Turbulent Flows Generated by Multi-scale Structures - from a Fractal Tree to a Fractal Canopy

by

Kunlun Bai

A dissertation submitted to Johns Hopkins University in conformity with
the requirements for the degree of Doctor of Philosophy

Baltimore, Maryland
January, 2014

Abstract

The vegetation canopy has a significant impact on various physical and biological processes. Most scaled laboratory experimental studies have used canopy element models that consist of rigid vertical strips or cylindrical rods that can be typically represented through only one or a few characteristic length scales while, most natural vegetation is highly multi-scale with branches and sub-branches, covering a wide range of length scales. Since fractals provide a convenient idealization of multi-scale objects. We study the flows generated by multi-scale, fractal structures. We first present results of the momentum transport and energy flux across scales in the near-wake flow of a single fractal tree-like object. Detailed mean velocity and turbulence stress profiles are documented, as well as their downstream development. The transverse momentum fluxes can be quantified well by the Boussinesq eddy-viscosity model and associated Prandtl mixing length-scale. We find that the measured mixing length increases with increasing streamwise locations. Conversely, the measured eddy viscosity and mixing length decrease with increasing elevation, which differs from eddy viscosity and mixing length behaviors of traditional boundary layers or canopies studied before. In order to find an appropriate length for the flow, several models are proposed, based on the notion of superposition of scales. These proposed models agree well with the measured mixing length. The subgrid-scale kinetic energy fluxes, of relevance to Large Eddy Simulations, are obtained by spatially filtering the velocity field at various scales. The subgrid-scale fluxes exhibit strong scale-dependence which is different from the behavior in canonical flows. Using the data, we measure the scale-dependent injection of kinetic energy and find that the length-scale associated with momentum transport identified before successfully collapses the measured trends of kinetic energy injection. The results confirm that information about multi-scale clustering of branches as it occurs in fractals has to be incorporated into subgrid-scale models of flows through canopies with multiple scales.

Beyond studies of flows behind a single fractal tree, we also report the turbulence inside and above an entire canopy consisting of an array of fractal tree models. An index-matching technique is utilized based on matching the refractive indices of the tree elements and the working fluid. Such index matching provides optical paths for both light illuminations and camera recordings. As a result, the flow fields between each individual branch can be well resolved, which in prior work was very challenging or impossible due to optical interference. We observe distinct spatial partitioning of flows into wake and non-wake regions. The local velocities deviate significantly from spatially averaged values and the streamwise normal dispersive flux inside the canopy has larger magnitude (up to four times) than the corresponding Reynolds normal stress. The eddy viscosity and mixing length are deduced from the data and the mixing length can be described by models proposed for flows behind a single tree. Above the fractal canopy, the flow structures are quite different from that in typical boundary layer flows. From the instantaneous velocity field, we observe jet-like motions which are directly ejected from the region inside the canopy. Based on the linear stochastic estimation and the lead-lag correlation from two-point correlation, we identify the structure inclination angle of about 36° which is much steeper than the angle in typical boundary layer flows. We find that close to the canopy, in addition to large scale structures, the flows contain small-scale coherent structures which could contribute, at small scale, to momentum transport. A physical space filtering technique is then applied to the velocity field to study such structures.

Advisors: Dr. Charles Meneveau and Dr. Joseph Katz

Reader: Dr. Dennice Gayme

Acknowledgements

I would never be able to finish my dissertation without the guidance of my advisors, support from committee and other faculty members, help from friends, and love from my family. Upon the completion of my exciting journey in Johns Hopkins University, I would like to express my sincerest appreciation to everyone who have supported and helped me during my Ph.D. study.

I would like to thank my advisors, Dr. Charles Meneveau and Dr. Joseph Katz, for providing me such an excellent opportunity to work on this challenging project, for giving me the freedom to explore different aspects of the subject, for their encouragements at different stages of the study, and for their timely and insightful guidance in my voyage through turbulence. Whenever I was stuck with any kind of difficulties, they always had brilliant solutions waiting there to help me out. Without their consistent supports, none of the studies in this thesis could be finished. Besides helping me to become a better researcher, they also help me to grow and to become a better person. It is my great privilege to work with them and learn from them.

I would like to thank Dr. Dennice Gayme for reading my thesis and providing detailed suggestions which greatly improve the quality of the thesis. I also would like to thank other faculty members for their help in past few years. Among many of them, Dr. Andrea Prosperetti, Dr. Omar Knio, Dr. Takeru Igusa, Dr. Greg Eyink, and Dr. Markus Hilpert provided excellent courses on various topics which prepared me well for my own research. I also would like to thank Dr. Lester Su and Dr. German Drazer for serving in my DQE and GBO committee respectively.

Special thanks are due to Dr. Yury Ronzhes for his very close involvement during the facility design and assembly, as well as technical supports during the experiments. My thanks also go to Stephen King who designed the electronic devices for the drag measurement. I would also like to thank Robert Blakely in undergraduate fluid mechanics lab for his help when I was a TA in the lab and for his kind supply for the temperature control bath during our index-matching measurement.

I would like to express my sincere thanks to my colleagues in the lab for their generous help both in the studies and in daily life. The name list is a long one: Dr. Huixuan Wu, Dr. Jiarong Hong, Dr. Pranav Joshi, Dr. Siddharth Talapatra, Cao Zhang, Yuan Lu, Aditya Nayak, David Tan, Cheng Li, Hangjian Ling, Kaushik Sampath, Courtney Engle, Dr. Xiaofeng Liu, Dr. Rinaldo Miorini, Dr. Mingming Zhang, Dr. Tiffany Camp, Dr. David Murphy, Dr. William Anderson, Dr. Marc Calaf, Jason Graham, Claire Verhulst, Adrien Thormann, Hector Morales, Xiang Yang, Tony Martinez, Joel Bretheim, Perry Johnson, Carl Shapiro, Dr. Hyung-Suk Kang, Dr. Marco Martins-Afonso, Dr. Huidan Yu, Dr. Adrian Sescu, Dr. Richard Stevens, Dr. Di Yang, Dr. Michael Wilczek, Greg Kheyfets, Kalen Parrott, and others. No one gets to select who their co-workers are going to be, but I don't think it would worked better that had I picked all of you myself. It is my pleasure to know all of you.

I also would like to thank the financial supports from sponsors: NSF ATM-0621396, AGS-1047550, the Sardella Chair and W.F. Ward at Johns Hopkins University.

Last but not least, I would like to dedicate this thesis to my parents, Baoxing Bai, Liemin Liu, and my wife Xiaomo Chen. I am forever in debt and gratitude to my beloved parents. I also thank Xiaomo, who is always there cheering me up and stand by me through the bad times and good.

Table of Contents

List of Figures

List of Tables

Chapter 1. Introduction

Turbulent flows within and above vegetation canopies play significant roles in many physical and biological processes (Finnigan 2000; de Langre 2008), such as forest microclimate (Shaw et al. 1988), rainfall distributions (Mahfouf and Jacquemin 1989), and climate change. The flow motions have significant impacts on hydrological, nitrogen, and carbon dioxide cycles among other important biological cycles. They are also responsible for various transport processes, for examples the dispersal of seed particles (Nathan et al. 2002), transport of scalars such as temperature and pollutants, and so on. Turbulent flow structures directly control the interactions between canopies and the atmosphere. To better understand and then control these various processes, one needs good understanding of the flow motions inside the canopy and the associated momentum, energy and scalar transport. For this purpose, extensive studies have been carried out over the past few decades by field and laboratory experiments, as well as by numerical simulations. These studies have provided important information about the flow motions in a variety of canopies. Detailed information about the relevant flow phenomena are summarized in Raupach and Thom (1981), Finnigan (2000) and Finnigan et al. (2009) among other studies.

1.1 Canopy with multi-scale elements and flow characteristic length scales

In laboratory environments, detailed flow information can be provided through studies of model canopies. Such studies often raise an important issue related to the geometry of canopy elements. Canopy models with more or less realistic tree shapes have been studied by various authors (Stacey et al. 1994; Marshall et al. 2002; Pietri et al. 2009). However, in general, most models used in laboratory experiments have consisted of rigid vertical strips (Raupach et al. 1986) and cylindrical rods (Seginer et al. 1976; Poggi et al. 2004b; Zhu et al. 2006), as well as nylon stalks with aero-elastic features (Finnigan and Mulhearn 1978; Brunet et al. 1994; Shaw et al. 1995). These simplified objects typically only have one or a few characteristic length scales (e.g. the diameter and height for cylindrical canopy elements). In natural systems, however, canopies consist of vegetation elements such as trees that contain multiple length scales (de Langre 2008). They are composed of big trunks, branches at small scales, sub-branches at smaller scales, and leaves at the smallest scales. The scale distributions vary at different elevations. Furthermore, different elements could be viewed as groups of clusters, which can impose additional length scales. The natural canopy is a multi-scale system which can be approximated conveniently as consisting of fractal objects (Mandelbrot 1982; Barnsley 1988). While fractal aspects of turbulence have been studied in several works in the past few decades (Mandelbrot 1975; Sreenivasan and Meneveau 1986; Meneveau and Sreenivasan 1991), research on interactions of turbulent flows with fractal objects began more recently. For example in turbulence behind a fractal grid with multiple length scales, studies reveal distinct flow physics such as unusually high turbulence intensities and a constant ratio of the integral scale to the Taylor microscale during the decay (Hurst and Vassilicos 2007; Seoud and Vassilicos 2007; Mazellier and Vassilicos 2010; Stresing et al. 2010; Valente and Vassilicos 2011; Gomes-Fernandes et al. 2012) at least close to the fractal grids (see Krogstad and Davidson 2012, Thormann and Meneveau, 2014). The turbulent flows generated by multi-scale fractal-like objects could display properties that are quite different from turbulence generated by objects characterized by a single length scale. For canopy turbulence, flow generated by multi-scale elements has not yet received much attention. It would be interesting and valuable to study how the elements affect the momentum and energy transport at various scales, as well as the difference from the canopy turbulence generated by elements with single length scales.

The elements inside a canopy change the flow properties and moreover modify the length scales in the flow fields. The study of length scales in canopy flows is essential, since the length scale is the key parameter in many models of turbulence energy, momentum and scalar transport (Seginer et al. 1976). The mean streamwise velocity profile can be predicted by using mixing-length models while invoking the Boussinesq eddy-viscosity concept (Cionco 1965; Macdonald 2000). Knowledge about characteristic length scales is also utilized in various canopy-flow models (Wilson and Shaw 1977; Katul et al. 2004; Poggi et al. 2004b). For a canopy with multi-scale elements, understanding of characteristic length scale and its effects on the momentum and energy transport is still lacking. It is even more difficult to provide possible linkages between complex multi-scale canopy morphology and scales in the turbulent canopy flow.

Exploring such linkages is now becoming possible in part because of rapid developments of geometry characterization techniques such as LIDARS (light detection and ranging). These allow detailed measurements of foliage distributions and of the general morphology of canopies. For canopies with simple-geometry elements, the linkage between the flow and canopy length scales has been studied before. For example in experiments in a cylindrical-rod model canopy, Poggi et al. (2004b) proposed that the mixing length inside the canopy is a constant value proportional to the diameter of the rods, and closely related to von Karman vortices generated by the rods. Above the canopy, boundary layer scaling of the mixing length, i.e. proportional to κz (where κ is the von Karman constant) is observed. The transition between a constant mixing length to the boundary layer behavior occurs near the top of the canopy. Conversely, for canopies with multi-scale elements the relationship between the canopy morphology and the flow scales raises important questions such as: what are the important scales in the flow? Can these flow scales be expressed as function of the geometry of the canopy elements?

1.2 Energy cascading process

Another important issue is how the multi-scale elements affect the energy cascade. In classic turbulence, one of the most important phenomena associated with turbulent flows is the Richardson energy cascade（Richardson 1922; Frisch 1995), and the Kolmogorov 1941 theory and its phenomenology of fully developed turbulence are considered major milestones in our understanding of turbulent flow physics. Energy is injected into the flow from eddies with large scales in the energy-containing range and is then successively transferred to smaller-scale motions. This process continues until the eddies are so small that molecular viscosity plays a dominate role and facilitates dissipation of kinetic energy into heat. Between the energy-containing and the dissipation range, no addition nor loss of energy occurs, i.e. the flux is independent of scale. The rate at which kinetic energy is transferred among scales also plays a vital role in numerical simulations, in particular in Large Eddy Simulations (LES) (Piomelli et al. 1991).

In the spectral domain, the energy balance (Tennekes and Lumley 1972; Hinze 1975; Pope 2000) reads

$$\frac{\partial E(k,t)}{\partial t} = P(k,t) - \frac{\partial \Pi(k,t)}{\partial k} - 2\nu k^2 E(k,t), \tag{1.1}$$

where $E(k,t)$ is the (radial) energy spectral density. On the right hand side of this equation, the first term $P(k,t)$ represents the spectrum of net injection of kinetic energy. It consists of production due to mean shear as well as possible contributions to the spectral balance arising from other large-scale effects, such as spatial transport of kinetic energy in inhomogeneous flows. The third term is viscous energy dissipation which is effective at small scales. The spectral energy flux $\Pi(k,t)$, whose divergence in wavenumber space describes its effects at each wavenumber, connects the energy-containing and viscous ranges and will be the main quantity of interest of the present study. It represents the spectral transport of energy from wavenumbers smaller than k to wavenumbers larger than k (or from large to small scales). It serves a crucial role in the energy balance, and is a key ingredient in many turbulence models (Monin and Yaglom 1975), such as the spectral models from Obukhov (1941), Heisenberg (1948) and Pao (1965). One can see from Eq. 1.1 that for a steady-state case, in the inertial range where the net production and viscous dissipation may be thought to be negligible, the energy flux is independent of wavenumber. This scale-independence corresponds to the constant (average) energy transfer rate in the inertial range during the Richardson-Kolmogorov cascade.

The spectral energy flux as a tool to study the energy cascade has been considered mainly in the context of turbulence theories (Kraichnan 1971) and numerical simulations (Ishihara et al. 2009). From an experimental perspective, the spectral energy flux has been studied less often, due to challenges in measuring the full three-dimensional fields required for Fourier analysis. However, a physical-space interpretation becomes more accessible using experimental data, and then higher Reynolds numbers can be reached. In particular, the spectral energy flux can be evaluated based on the physical-space filtering methods of direct relevance to Large Eddy Simulations (Piomelli et al. 1988; Moin 2002). For example, Liu et al. (1994) apply this framework to experimental data of turbulent jet. Chen et al. (2006) utilize the same technique to study the scale interactions of turbulence during straining. Carper and Porté-Agel (2008) focus on the energy flux in boundary layer flow over a surface roughness transition. More recently, Kelley and Ouellette (2011) apply the filtering approach to study the spatiotemporal persistence of spectral fluxes in two-dimensional turbulence.

In these past studies that mostly involved canonical turbulent flows, kinetic energy was typically introduced at one, or at a few well-defined length-scales. For example, the characteristic scale would be the jet diameter for a turbulent jet, and the boundary layer thickness for boundary layer flows. Often, however, turbulent flows interact with objects that have a multiplicity of length-scales, such as vegetation elements that contain tree trunks, branches of many generations, and leaves (Finnigan 2000; de Langre 2008). In particular, the scale-to-scale energy transfer associated with such flows in which kinetic energy is injected over many length-scales has not been examined systematically, but it is of considerable interest. Taking vegetation canopies as an example, previous research has identified non-standard energy transfer processes due to the interactions between the flow and canopy elements, leading to concepts such as energy cascade bypass (Finnigan 2000; de Langre 2008; King et al. 2012). The elements in the canopy could interact with the turbulent flows. Such interactions produce structures at scales comparable with the size of the canopy elements. As a result, the turbulent kinetic energy at large scales could be directly converted into energy at smaller scales, bypassing the typical energy cascading process. In our study, we want to explore following questions: how do the multiple scales modify the energy cascading process? Can characteristic length-scales be defined to collapse physical quantities that are directly relevant to the cascade process?

1.3 Flows generated by canopy with non-uniform foliage distribution

Our knowledge on canopy turbulent structures mostly comes from studies of canopies with a relatively uniform vertical and horizontal foliage distribution. Only a few studies have focused on the flow fields in forests with vertically varying or even discontinuous foliage distribution such as in Baldocchi and Meyers (1988). In a recent study, Dupont et al. (2012) carried out both field meansurements and Large Eddy Simulations (LES) to study turbulent structures in a maritime pine forest characterized by a high, dense foliated layer associated with a deep and sparse trunk space. Wake structures developing behind the tree stems were observed and the mean velocity profile displayed a secondary maximum within the trunk layer. These features are different from typical flow behaviors in canopies with uniform foliage distribution. In another recent wind tunnel experiment carried out by Bohm et al. (2013), distinct spatial partitioning of flows into wake and non-wake regions was observed within the model canopy of bluff elements. These recent studies display heterogeneous flow fields associated with wake structures inside the canopy especially those with a discontinuous foliage distribution. The highly non-uniform flow fields could then contribute to significant horizontal momentum and energy transport, in addition to the vertical transport. Horizontal transport is important for a number of physical processes inside canopies such as mixing and expansion of pollutant plumes, transport of seeds and pollen, and so on.

Most previous experimental studies focus on measurements of vertical distributions of flow quantities while studies of flow distributions in horizontal planes are rather limited. For field measurements, there exist inherent difficulties in sampling sufficiently large flow fields covering a wide dynamic range with sufficient spatial resolution. Field measurements are mostly carried out by point measurements at single, or multiple, locations. In laboratory studies, although sampling regions are more easily accessible than in the field, it is still difficult to acquire data inside complex-geometry canopies especially in regions between canopy elements due to geometric or optical interference inside the canopy. Canopy velocity measurements are usually performed by point measurement techniques such as hot-wires (Raupach et al. 1986; Novak et al. 2000; Bohm et al. 2013), laser doppler velocimetry (LDV) (Pietri et al. 2009), laser doppler anemometry (LDA) (Righetti and Armanini 2002; Poggi et al. 2004a,b), and sonic anemometers (Launiainen et al. 2007). These studies, however, are carried out in a limited number of locations and thus cannot provide a complete picture of flow motions. Spatial distributions have been obtained using Particle Image Velocimetry (PIV) (Zhu et al. 2007; Reynolds and Castro 2008; Yue et al. 2008), but optical interference prevents full access. Also, past measurements have focused on vertical distributions of flow quantities while data to study horizontal transport is not yet available.

Canopy flow fields are highly non-uniform and local mean (time-averaged) velocities may deviate significantly from spatially averaged velocities. The effects of these deviations on mean momentum of the flow are quantified by so-called “dispersive fluxes” which arise from double averaging of the momentum equation. Small dispersive fluxes are indicative of small inhomogeneity of the mean velocity profiles. Relatively small dispersive fluxes have been reported in canopies with uniform foliage distributions (Raupach 1994; Kaimal and Finnigan 1994; Cheng and Castro 2002) in which case neglecting them (e.g. Lien et al. 2005; Tanino and Nepf 2008; Luhar et al. 2008) appears appropriate. Recently, however, studies have shown that dispersive fluxes may become significant in canopies with non-uniform foliage distributions. By using numerical simulations of turbulent boundary layer over an array of cubes, Coceal et al. (2006) showed that the dispersive fluxes can be about 20% of the total shear stresses. Martilli and Santiago (2007) found the dispersive fluxes are comparable with the Reynolds stresses within canopy consisting of an array of cubes. By using LDA measurements, Poggi et al. (2004a) showed that the dispersive fluxes can reach 35% of the Reynolds stresses in sparse canopies. In their experiments, the point measurements are performed at 11 locations with non-uniform distribution. The entire flow field is then represented by these measurements through a weighted scheme where the weighting is proportional to the fraction of ground represented by each point. Aberle et al. (2008) argued that dispersive fluxes obtained from point measurements could be inaccurate due to coarse spatial resolution. They suggested the use of PIV in future studies. Ferreira et al. (2009)

and Moltchanov et al. (2011) carried out PIV measurements of dispersive fluxes inside canopies, the latter in a canopy consisting of randomly distributed cylinders. They noticed that the normal component of dispersive fluxes within the canopy entry region can be significantly larger than the normal Reynolds stresses.

To capture the flow fields inside the canopy, one needs to overcome the inherent difficulties associated with optical access to the flow between complex-geometry structures. We utilize the index-matching technique, which matches the refractive indices of the tree models and the working fluid. The trees in the working fluid become invisible and transparent, which opens up optical paths for light illuminations and camera recordings. The detailed description of this technique is presented in the following chapter.

1.4 Coherent flow structures above canopies

In the past few decades, studies of turbulent coherent structures in flow above canopies have been carried out based on data from field and laboratory experiments (e.g., Baldocchiand and Meyers 1988; Paw et al. 1992; Collineauand and Irvine 1993a,b; Turner et al. 1994; Qiu et al. 1995; Shaw et al. 1995; Brunet and Irvine 2000; Finnigan and Shaw 2000; Ghisalberti and Nepf 2002; Zhu et al. 2007), as well as from numerical simulations (e.g., Kanda and Hino 1994; Su et al. 2000; Shaw et al. 2006; Yue et al. 2007; Dupont and Brunet 2008, 2009; Finnigan et al. 2009). The coherent structures were often revealed by two-point turbulence statistics, conditional averages, wavelet analysis, empirical orthogonal function (EOF) analysis, and so on. For example, based on streamwise velocity correlations, it was shown that a significantly large area with strong correlation could extend to about 10 times and 4 times of the tree height in streamwise and vertical directions respectively (Shaw et al.1995; Finnigan 2000). The correlation map tilted with an angle relative to the wall. The vertical velocity, on the other hand, was correlated over a much more restricted region. From quadrant analysis, it was shown by several studies that above the canopy, sweeping motions had larger contributions to total momentum transport in regions close to the canopy (Finnigan 1979; Raupach 1986; Zhu et al. 2007). Away from the canopy, ejections became dominant. The behavior was in contrast with that in smooth-wall boundary layers where ejections are dominant throughout the boundary layer. Among other studies, the flow motions were also studied by using other decomposition methods such as wavelets (Collineau and Brunet 1993a, b; Turner et al. 1994; Qiu et al.1995; Brunet and Irvine 2000) and EOF (Finnigan and Shaw 2000; Finnigan et al. 2009). A comprehensive review of various coherent structure detection methods was presented by Finnigan (2000). To further understand the mechanism of flows above canopies, several models of canopy eddy structures were proposed. Based on wind-tunnel experimental data, Finnigan and Shaw (2000) proposed a model consisting of a family of head-down hairpin vortices. This model was in accordance with the mixing-layer hypothesis proposed by Raupach et al. (1996). More recently, Finnigan et al. (2009) evaluated the data from a Large Eddy Simulation (LES). By using conditional averaging and EOF, they revealed coherent structures in the flow, and updated the previous model of a single head-down hairpin model by a newly proposed dual-hairpin model, which consists of both head-down and head-up hairpin vortices at low and high elevations, respectively. It was shown that the dual-hairpin model could explain a large set of observations from real and model canopies.

In typical turbulent wall-bounded flows, coherent structures have been determined by a substantial amount of experimental and numerical studies. Inclined hairpin vortices, firstly introduced by Theodorsen, have become a well accepted model for fundamental structures in turbulent boundary layers. The ejection generated between the legs of the primary hairpin generates a secondary head-up hairpin upstream, and this in turn generates another, and so on. These multiple hairpin structures could travel at the same convective velocity and form vortex packets, so-called large-scale motions (Kim and Adrian 1999; Zhou et al. 1999; Adrian et al. 2000; Guala et al. 2006; Adrian 2007; Balakumar and Adrian 2007). A characteristic feature of the large-scale motions (LSMs) is that the hairpin vortices within the packet align in the streamwise direction and induce regions of low-streamwise momentum between their legs (e.g., Brown and Thomas 1997; Ganapathisubramani et al. 2003; Tomkins and Adrian 2003). Compared to the dual-hairpin model in canopy turbulence proposed by Finnigan et al. (2009), the hairpin-vortex-packet theory in typical wall-bounded flows only consists of multiple head-up vortices. The difference may indicate different mechanisms in these two types of flows. It is of interest to compare some features of the coherent structures in canopy flows and typical wall-bounded flows. Such comparisons, especially from geometrical perspectives, are still limited.

The coherent structures incline with certain angle with respect to the wall in both types of flows. In turbulent boundary layers, the structure inclination angles are found to be from 12° to 20°, through flow visualization techniques (Head and Bandyopadhyay 1981; Adrian et al. 2000; Christensen and Adrian 2001), linear stochastic estimation (Christensen and Adrian 2001; Volino et al. 2009), and lead-lag correlation from two-point correlation (Brown and Thomas 1977; Carper and Porte-Agel 2004; Marusic and Heuer 2007; Chamorro and Porte-Agel 2010; Guala et al. 2011; Chauhan et al. 2013). By using the last method, Marusic and Heuer (2007) measured the correlation between directly measured wall shear stress and the velocity from a sensor above the wall. By identifying the spatial delays of the correlation peak when the velocity sensor locates at different elevation, the inclination angle was inferred. They found that the inclined angle was about 14° and was independent of Reynolds number. Chauhan et al. (2013) applied the lead-lag correlation method based on streamwise fluctuation velocities to quantify the inclination angles in atmospheric boundary layers. They noticed that the angles vary with atmospheric conditions. For example during unstable conditions, the angle could be high and reach to about 50°. However, the inclination angle during neutral conditions was found to be consistent with that in typical turbulent boundary layers, about 14°. Compared to the intensive studies of inclination angle in wall flows, studies of the angle in canopy turbulence are less prevalent. Moreover, the analysis framework which is often used in canopy flows is not consistent with that in typical wall flows as shown in the following sections. The angle is mostly estimated from the major axes of the two dimensional map corresponding to the correlation function. However, as indicated by Shaw et al. (1995), the tilted major axis may not represent the inclined coherent structures well, and it could be smaller than the angle of actual coherent structures. As a result, a direct comparison of the inclination of coherent structures in canopy flows and turbulent boundary layers cannot be easily established. In our study, we analyze the coherent structure inclination in our canopy flows using methods proposed in studies of wall-bounded flows. A reanalysis of some existing data in the canopy flow literature is also undertaken.

The inclination angle not only describes the flow structures, but is also an important parameter in various wall-models in numerical simulations. For example in LES, the first grid point is usually far away from the wall. The instantaneous wall shear stress cannot be obtained directly. This term is usually parameterized through models which relate the instantaneous velocity at some distance above the wall, mean shear stress, and mean streamwise velocity. Examples include the shifted Schumann-Grotzbach model (Piomelli et al.1989), and a model proposed by Marusic et al. (2001). In these models, a streamwise shift is involved which arises from the fact that inclined structures in the near-wall region play important roles in the energy and momentum transfer in wall-bounded flows. The shift has been shown to play a vital role in accurately estimating the surface shear stress by a priori evaluations (e.g., Carper and Porte-Agel 2004; Chamorro and Porte-Agel 2010; Li and Bou-Zeid 2011) and by a posteriori studies of the wall models (e.g., Stoll and Porte-Agel 2006, 2008). For canopy flows, if one wants to simulate the flow fields above the canopies without detailed descriptions of structures underneath, a proper correction in the wall models should also be used. As a result, it would be valuable to first have a good understanding of the structure inclination angles in canopy flows.

1.5 Thesis outline

To address the abovementioned issues and to achieve a better understanding of canopy turbulence, we perform systematic studies of flows generated by a canopy model with multi-scale, tree-like elements. The tree models, experimental facility, instrumentation, and the index-matching technique are presented in Chapter 2. The characteristic length scale produced by a single tree and its effect on the momentum transport are discussed in Chapter 3. Several models are proposed to quantify the scale distributions based on the notion of superposition of scales. As a result, the linkage between tree morphology and the scales in the flow is established. The energy cascading process in the wake of a single tree is further quantified in Chapter 4. The measured energy flux and net energy injection rates are discussed in detail, along with tests to verify whether the mixing length model developed to describe momentum transport could also succeed in collapsing quantities of relevance to the energy cascade. In Chapter 5, studies of turbulence inside the canopy with multiple tree elements are presented. We discuss the variation of the flow fields and importance of the associated dispersive fluxes. Horizontal momentum transport is furthermore studied through the eddy-viscosity formalism, where the eddy viscosity and mixing length can be deduced from the experimental results. We then compare the measured mixing length with the model proposed in Chapter 3. In Chapter 6, the studies of coherent flow structures above the canopy are discussed. We focus on the inclination angle of the structures and the coherent structures at various scales. Finally, we summarize and conclude our studies in Chapter 7.

Chapter 2. Experimental Set-up

This chapter describes the multi-scale model utilized in our studies, the experiment facility, experimental instrumentation, and the refractive index matching technique.

2.1 Fractal tree model and fractal canopy

The fractal tree model, which is shown in Fig. 2.1, has been manufactured using rapid prototyping (i.e. stereolithography with an ultraviolet curable material) based on a 3D Computer Aided Design drawing. The tree has five generations, with three ($N = 3$) branches at the each generation and a scale-reduction factor $r = 1/2$ between consecutive generations. This type of fractal can be characterized by its similarity fractal dimension (Mandelbrot 1982), defined in terms of the number of daughter elements (N) for each mother element, and their scale ratio (r), according to

$$D_f = \log(N) / \log(1/r). \tag{2.1}$$

For the present tree, we obtain $D_f = \log 3 / \log 2 \approx 1.585$. This fractal similarity dimension is consistent with known fractal dimensions of real vegetation, which have generally been found to be mostly between 1.45 and 1.74 (Burk 2005), or between 1 and 2 (Mandelbrot 1982). The tree geometry is a compromise between realism and simplicity, and preserves multi-scale and scale-invariance features. The first generation has three branches of diameter 28.8 mm ($= d_1$) and the fifth generation has 243 branches of diameter 1.8 mm ($= d_5$), with the total height of the tree (H) equal to 97.65 mm. In this thesis, the height is used as a reference length scale. Also, note that strictly speaking the fractal tree considered is a “pre-fractal”, since it does not contain an infinite number of sub-branches and has a small-scale “cut-off”. We could not include branches smaller that d_5 due to manufacturing difficulties and the need to maintain structural strength. If the fractal had included an infinite number of branches, its height would be $H_\infty = 2H_1 = 100.8$ mm, where H_1 is the height of the first generation of the tree. Also note that this type of fractal tree involves a direct relationship between height and scale (or between height and fractal generation number): smaller-scale branches are placed at increasing elevations away from the surface. And at any given height, only a single branch scale or generation number is present in the fractal object.

Figure 2.2 shows characteristic horizontal cross-sections for the five generations. By utilizing a set of many such fractal trees in planned future experiments, a fractal tree canopy can be constructed. Here, as a first step, measurements are reported for the near wake of a single tree, which is also of relevance to sparse canopies when interactions between trees may be neglected. During the experiments, the fractal tree faces the flow with the orientation indicated in Fig. 2.1b and Fig. 2.2. The leaf area density (a), as well as the accumulated frontal area (A_t) based on all branches and projected branches (Finnigan 2000; van Hout et al. 2007), are shown in Fig. 2.3. The leaf area density is defined as the single-side surface area per unit volume. Here, the frontal area is used as the surface area. Then the accumulated frontal area is the integration of frontal area from the ground. The lot area used in the definitions of the leaf area density is the area of a circle (with radius 100 mm) that encloses the horizontal cross-section of the tree at its maximum height. The leaf area increases significantly with increasing elevation, although the dimensions for single branches are small at high elevations. The leaf area index (*LAI*) of the entire fractal tree, defined here as the frontal area of all the branches divided by the lot area, is about 0.0128, and the projected frontal area index (*PFAI*), defined as the projected frontal area divided by the lot area, is about 0.0063. These two quantities closely follow the relation: $PFAI \approx LAI/2$ (van Hout et al. 2007).

In order to apply the reference index matching technique which allows an unobstructed view of the flow field between tree branches, two transparent trees, as in Fig. 2.4a, are made of material UOPTIC 2 with refractive index about 1.499. The branches of these two trees are manufactured by casting and molding technique. The tree models are then carefully assembled. Other tree models are made of non-transparent material as shown in Fig. 2.4b.

For our later experiments of flow within and above a canopy, a canopy model which consists of 12 identical fractal trees is utilized, as in Fig. 2.5. The trees are placed into four rows with three trees in each row. The row distance is 166 mm and the center-to-center distance of two trees in the spanwise direction is 190 mm. The target tree is located at the center of the third row where the flow measurements are carried out within a representative flow volume. The origin of the x, y, and z (or x_1, x_2, and x_3) coordinate system is placed at the center of the target tree in the x-y plane and at the bottom surface for $z = 0$. In studies of wake structures behind a single tree, we keep the target tree and remove other tree models. The definition of the coordinate system is same. The corresponding instantaneous velocities u, v, and w (or u_1, u_2, and u_3) indicate streamwise, spanwise and vertical velocities, respectively. The instantaneous velocity u_i can be decomposed to

$$u_i = U_i + u_i' , \tag{2.2}$$

where U_i is the mean velocity and u_i' is the velocity fluctuation. Throughout the study, the overbar indicates the ensemble average, and based on this decomposition, the (kinematic) Reynolds stress elements are defined as usual as $\overline{u'u'}$, $\overline{v'v'}$, $\overline{u'v'}$, etc.

2.2 Experimental facilities

Experiments were carried out in the bypass channel of the turbomachine facility in the Laboratory of Experimental Fluid Dynamics at the Johns Hopkins University, U.S.A. The working fluid is water at ambient temperature. Photos of the facility are shown in Fig. 2.6. The test section is 1040 mm long, 560 mm wide and 230 mm deep. Honeycombs and a shear generator are installed in the honeycomb chamber, 270 mm upstream of the test section to modify the incoming flow. The shear generator consists of a background mesh and nine strips of mesh wire, similar to that described in Zhu et al. (2006). We choose the design by aids of computational simulations using Fluent software and by testing the generator in the facility, in order to achieve desired incoming velocity profiles.

2.3 Instrumentations

During the experiments, detailed Particle Image Velocimetry (PIV) measurements are performed. The laser sheet is generated by a 120 mJ/pulse Nd:YAG laser, and has an estimated thickness of 1 mm. The illuminated particle images are captured by a 4864×3248 pixel CCD camera. Images are enhanced by the methods described in Roth et al. (1999), and velocity vector maps are calculated using multi-path cross-correlations in LaVision DaVis software. The final interrogation window size varies for different experiments and specific descriptions will be presented in following chapters accordingly.

During the measurements, the drag of the tree, which is located at the center of the third row of the canopy model, is recorded as well by using a load cell. The design of the load cell setting is shown in Fig. 2.7. Since the NaI solution is conductive which could short circuit the load cell, we installed the cell in a casing outside of the channel and filled with oil. The load cell and the oil in the casing are separated from the main loop by a customer-made rubber membrane. As an example, the measured drag signals of a single tree are shown as a function of time in Fig. 2.8. These measurements are performed at flow speed of 1.3 m/s. As branch generation number increases, i.e. more branches are added to the tree, the drag of the tree gradually increases due to the increasing blockage area. In Fig. 2.9, the measured drag of a single tree is plotted as a function of flow velocity. Different symbols represent tree with different branch generation numbers. For a tree with fixed generation, the drag increases with increasing velocity. For a fixed velocity, the drag increases with increasing generation numbers as well. At low velocity, the drag difference between trees with different generation numbers is much smaller than that at high velocity. It indicates the small branches at high elevation have larger impact on the drag at conditions of higher flow velocity. In addition, the drag coefficient of the single tree, $C_d=F/(0.5\rho V^2A_p)$, is shown as a function of the total generation number of the tree, at different flow speed in Fig. 2.10. A_p is the projected frontal area of the tree. The measurements agree well with simulation studies (Graham et al. 2011). In the present thesis, however, the detailed analysis of the drag signals will not be discussed, thus will be left for future studies.

2.4 Refractive index matching technique

Spatially resolved, non-intrusive optical velocity measurement techniques, such as PIV, have undergone a tremendous development over the last two decades. With recently introduced high-speed cameras and lasers, the temporal evolution of the flows can be acquired as well (Adrian and Westerweel 2011). Inherently, these methods require optical access both for illumination and image acquisition. For some applications, such as systems with complex geometry, this requirement cannot be easily satisfied. Some examples include studies of flows in porous media, near the blades of turbomachines, close to walls, and within canopies. In these studies, parts or the entire flow fields are blocked by the solid boundaries. Also, when the surfaces of objects are curved, e.g. in vascular models and Taylor-Couette flows, one has to overcome image distortion. In cases involving rough surfaces, reflection from boundaries becomes a challenge. To overcome these problems, one possible approach is to match the refractive index of the solid objects with that of the liquid. This approach provides essentially an unobstructed optical access and image distortion can be minimized.

Refractive index matching has been applied in several fields, such as the fluidized beds, particle suspensions, flows in porous media, and flows through complex geometries. Budwig (1994) and Wiederseiner et al. (2011) provided comprehensive reviews about this technique. To achieve index matching, a common approach was to use mixtures of different fluids by adjusting their relative concentrations. There were even cases involving combination of four different fluids (Averbakh et al. 1997). Mixtures of organic fluids have been used for example by Northrup et al. (1991), and a large scale mineral oil facility was described by Stoots et al. (2001). One of the popular approaches, which has been implemented in facilities of varying sizes, is to use solutions of sodium iodide in water. To mimic blood flow in vascular research, Shida et al. (2011) and Yousif et al. (2011) used a mixture of aqueous solution of glycerol and sodium iodide. The same approach was utilized to study flows in porous media (Zerai et al. 2005). Pure NaI solutions were used to match the refractive index of liquid and solid structures in porous media (Okumra et al. 2005; Yuki et al 2008), and to eliminate the image distortion caused by curved boundaries in Taylor-Couette flows (Parker and Merati 1996). This method was also used to match the refractive index of the liquid and acrylic particles in slurry flows (Chen 1991; Wildman et al. 1992; Chen et al. 1994). Large-scale studies of flow structures and turbulence statistics within acrylic turbomachines inserted in an NaI test loop were reported in e.g. Uzol et al. (2002) and Wu et al. (2012). The same facility has been used for measuring turbulence in the inner part of rough wall boundary layers (Hong et al. 2011; Talapatra and Katz 2012), and in present studies. Although the NaI solution is expensive for applications involving large facilities, the same liquid could be used for many years, and in multiple studies.

In planning for utilizing transparent plastics in index-matched experiments with NaI solutions, it is essential to know how the refractive index of the solution varies with concentration. Answers covering part of the relevant range are provided in prior publications (Chen 1991; Narrow et al. 2000; Shida et al. 2011). In this thesis, we extend the data range up to the temperature-dependent solubility limit of NaI solutions. This range covers the refractive index of hard transparent plastics, which can be machined, molded and manufactured in complex shapes using rapid prototyping.

During the tests, we vary the mass concentration of the NaI solutions in distilled water and measure their refractive index at different temperatures (*T*). The concentration (*c*) is defined as the ratio of sodium iodide mass to the total mass. The accuracy of weight measurements is ±0.05 g, resulting in a concentration uncertainty of 2%. The refractive index of the solution is measured at a wavelength of 589 nm using a digital refractometer (Sper Scientific, Model 300034) that has a stated accuracy of ±0.001. The temperature is controlled using an immersion circulator bath (Cole-Parmer Polystat Series 12003) at ±0.02˚C. The tests are performed at 23˚C, 30˚C, 35˚C, and 40˚C. For each temperature, we also estimate the solubility of NaI based on the maximum mass of salt that can be dissolved. During each test, we gradually add NaI salt into the solution while stirring it. Close to the solubility limits, measured amounts (0.5 g) of salt are added, and stirred for 5 minutes. Then, stirring is stopped for another 5 minutes, while the temperature is kept constant. If no reformation of salt crystal is observed, an additional amount of salt is added, and the process is repeated. We stop when visible solid crystals remain in the stirred sample. Once the salt dissolves, it does not reform as long as the temperature does not decrease. During the measurements, the solution remains colorless and transparent for several hours. However, left exposed to oxygen and light for longer periods, aqueous solutions of NaI become yellow, presumably due to formation of minute amounts of I_3^-, which absorb part of the visible spectrum. This process can be reversed in closed system, by e.g. keeping the solution in an oxygen-free environment (Uzol et al. 2002). For a solution at the temperature-dependent solubility, decreasing the temperature causes reformation of crystals. This process is also reversible by increasing temperature again. In our large facility, a viable approach has been used to keep the room at a temperature that exceeds the solubility limit. Otherwise, as we have found out, the salt crystals reform on the windows/walls and in the free stream.

Refractive indices of typical transparent solid materials are summarized in Fig. 2.11, including fluorinated ethylene propylene (FEP), silicone elastomers, silica gel, polyvinyl acetate (PVA), glass, acrylic and polycarbonate. For these materials, we use information available in published literature and technical information provided by vendors. In addition, we include three recently introduced materials and measure their indices by inserting them into the NaI solutions (see Fig. 2.12). The first is UOPTIC 2 (manufactured by Forecast3D), which can be molded into desired shapes, e.g. Figs 2.12a-c. We are presently performing experiments of canopy turbulence using index-matched UOPTIC 2 tree models. The second is RenShape®SL7870 (manufactured by 3D system corporation), which can be formed into desired shapes using rapid prototyping (Fig. 2.12d-f). The third, Crystal Clear®, can be manufactured using 3D printing. Consequently, these materials could be produced in essentially any desired shape. In some of these cases, achieving matched refractive indices requires NaI concentrations that can only be achieved above certain threshold temperatures. The presently measured solubility of sodium iodide in water for several temperatures is summarized in Table 1.

Figure 2.13a summarizes previously measured refractive indices of NaI solutions by Chen (1991), Narrow et al. (2000), and Shida et al. (2011). Narrow et al. (2000) showed that at a constant temperature of 20˚C, the refractive index decreased by about 0.003 when the wavelength increased from 589 to 632 nm. On the other hand, at wavelength of 589 nm, the refractive index decreased by about 0.004 when the temperature increased from 20˚C to 40˚C, i.e. the temperature effects were quite small at typical conditions. A similar trend was shown by Chen (1991). Narrow et al. (2000), based on their measurements, introduced an empirical model, in which the refractive index (ranging from 1.43 to 1.48) was linearly dependent on concentration and temperature, and had quadratic dependence on wavelength. Overall, these available data cover a broad range of concentrations and indices, but do not extend to those of acrylics or the abovementioned, recently introduced plastics. In the present measurements, we extend the range up to conditions that could only be achieved above a certain temperature because of solubility limits. Our results are added to the previous measurements in Figure 2.13b. At 23˚C, our measured refractive indices range between 1.333 and 1.499. At the overlapped range, our data are generally indistinguishable from the previous results, keeping in mind the abovementioned fourth digit effects of temperature, wavelength and accuracy of the refractometer. At higher temperatures, namely 30˚C, 35˚C, and 40˚C, we generally restrict our range of concentrations to those that could not be achieved at lower temperatures with some overlap. The results seem to follow the trend observed at 23˚C. A quadratic, least-square fit to our all data gives

$$n = 0.2425c^2 + 0.09511c + 1.335, \tag{2.3}$$

where n is the refractive index. The R^2 value is 0.9997, i.e. the data fit very well with the empirical fit. Fig. 2.13c is a magnified part of the data, including the empirical fit, which focuses on the results for high concentrations. It is aimed at demonstrating the variations of refractive index with temperature for several concentrations. For example, for c=64%, the indices are 1.4952, 1.4941, 1.4935, 1.4929 and 1.4921 at temperature of 23˚C, 30˚C, 35˚C, 40˚C, and 45˚C, respectively. At c=65.5%, the indices decrease from 1.5021 to 1.4996 as the temperature increases from 30˚C to 45˚C. A decrease of about 0.0008 for a

5˚C increase in temperature is consistent with the low concentration results of Chen (1991) and Narrow et al. (2000). These variations are less pronounced than those associated with changes in e.g. concentration, and are hardly visible in the scales of Fig. 2.13b. However, they will affect the data in studies involving large temperature gradients.

The present results indicate that to use the easily moldable UOPTIC 2, the facility has to be maintained at temperatures exceeding at least 23˚C. To use RenShape®SL7870, which can be formed into complex shapes using rapid prototyping, a temperature of at least 40˚C is required. Such temperatures control can be easily achieved for the small-scale experiments, but require careful attention in large facilities.

The viscosity of the solution increases with concentration, and decreases with increasing temperature. Zaytsev and Aseyev (1992) present the properties of various aqueous solutions of electrolytes, covering a wide range of concentrations and temperatures. For NaI solutions, for example, the dynamic viscosity (μ) and density (ρ) are provided at concentrations of 10%-63% and temperatures of 10-90˚C. Within these ranges,

$$\log_{10}\mu = \log_{10}\mu_0 + \left(d_0 + d_1 T\right)c, \tag{2.4}$$

$$\log_{10}\rho = \log_{10}\rho_0 + \left(b_0 + b_1 T + b_2 T^2\right)c, \tag{2.5}$$

where T is expressed in ˚C, d_0=64×10^{-2}, d_1=-55.8×10^{-4}, b_0=4036.7×10^{-4}, b_1=-294.9×10^{-6}, and b_2=183.2×10^{-8}. The dynamic viscosity of pure water, μ_0, can be determined from Slott formula as

$$\mu_0 = 0.59849\left(43.252 + T\right)^{-1.5423}, \tag{2.6}$$

while the density of pure water, ρ_0, can be estimated from

$$\rho_0 = 1000 - 0.062T - 0.00355T^2. \tag{2.7}$$

These empirical expressions agree with measurements and other models quite well (e.g., Lengyel et al. 1964; Goldsack and Franchetto 1977, 1978; Kacperska et al. 1989; Jiang and Sandler 2003; Abdulagatov et al. 2006). For 63% concentration, the kinematic viscosity (ν) estimated from Eqs. 2.4 and 2.5 is 1.21×10^{-6}, 1.04×10^{-6} and 0.9×10^{-6} m^2/s at 20˚C, 25˚C, and 30˚C, respectively. These results are consistent with the 1.1×10^{-6} m^2/s value reported in Uzol et al. (2002). Extrapolating the kinematic viscosity to a higher concentration of 67.5% and temperature of 40˚C, which is required for maintaining such a concentration, gives a kinematic viscosity of 0.7×10^{-6} m^2/s.

As can be seen from our measurements above, a broad range of refractive indices, from 1.33 to 1.51, can be achieved by varying the concentration of sodium iodide in water. This range covers most of the commonly used transparent materials, except for polycarbonate. It also covers the indices of a couple of recently introduced and particularly attractive materials that could be formed into complex shapes using molds or rapid prototyping, although in some cases the required concentration can only be achieved above threshold temperatures. A quadratic empirical expression relating the concentration to the refractive index and the temperature-dependent solubility is presented. It extends the range that previous models covered. As concentration increases, viscosity of solution increases. The absolute value of viscosity could be tuned by adjusting the temperature, and could be close to that of water. As a result, the NaI solution could be a good replacement for water in studies of high Reynolds number flows when index-matching is needed.

During our studies of wake structures behind a single fractal tree (Chapter 3 and 4), it is not necessary to apply the index-matching technique. The experiments are performed in water. However in the studies of flow in a canopy, index-matching is required in order to overcome the inherent optical interference of tree branches. To achieve it, the target tree and the tree next to it are made of a material called UOPTIC 2 whose refractive index of about 1.499. This falls in the range that can be achieved with a sodium-iodide (NaI) solution. A perspective view of the canopy inside the test section is shown in Fig. 2.14a, where two transparent trees made of UOPTIC 2 are visible. The effect of using a NaI solution as index matched working fluid is shown in Fig. 2.14b, where the partially-filled facility is shown. The dashed line in Fig. 2.14b indicates the solution level when the photograph was taken (for the measurements, the test section is filled). Below the solution level, branches of the two transparent trees become essentially invisible and one can actually see the branches of the tree behind them. As a result optical paths for both illuminations and image recordings to access any portion of the flow exist.

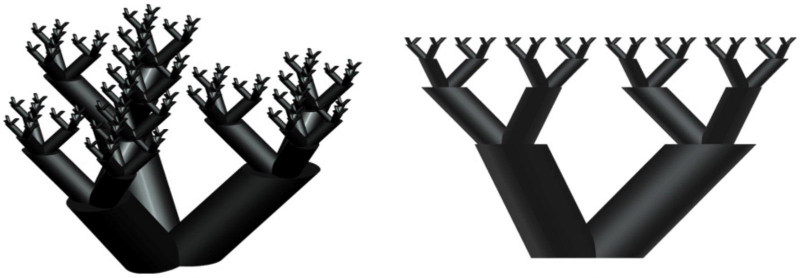

(a) (b)

Figure 2.1 Fractal tree model used in the present experiments: (a) perspective view; (b) frontal view.

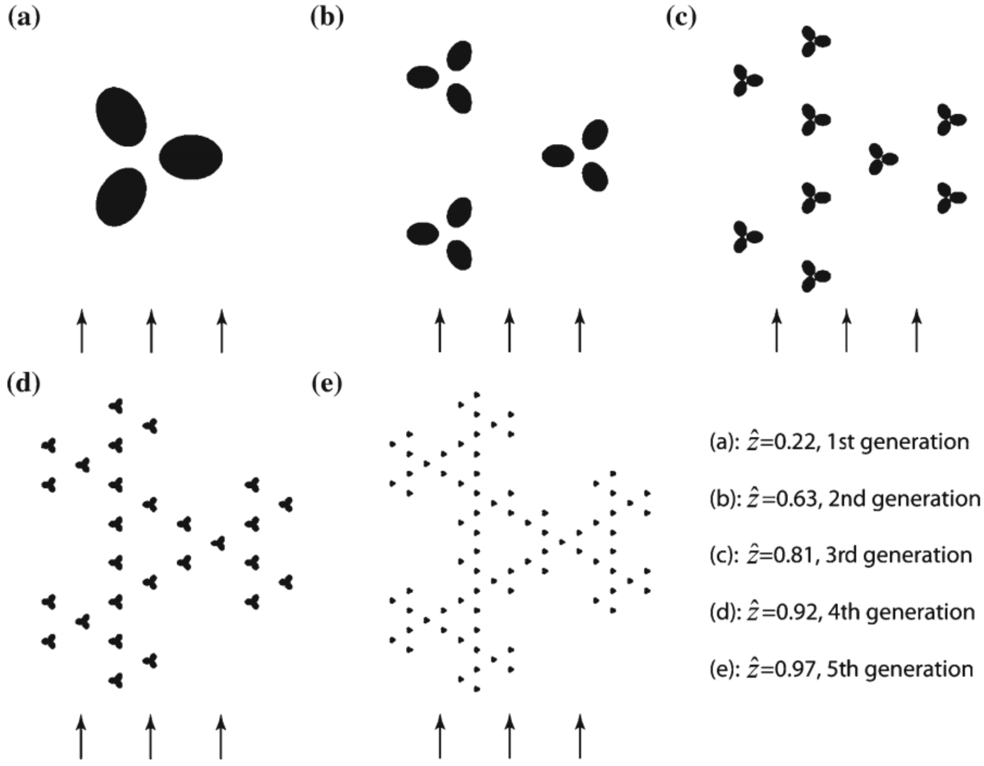

Figure 2.2 Typical horizontal cross-sections of the five generations with corresponding heights indicated by $\hat{z} = z/H$. The flow direction is indicated by the arrows.

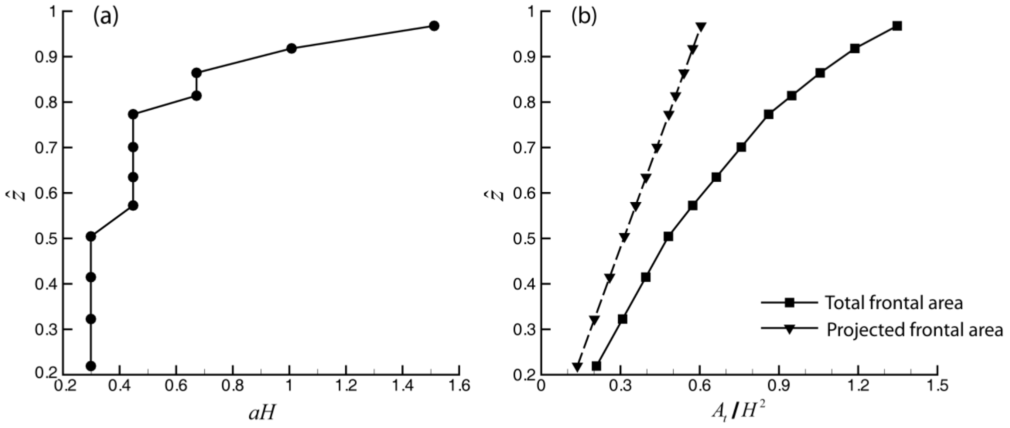

Figure 2.3 Leaf area density (a) and accumulated frontal area of the fractal tree (b) as a function of the normalized height $\hat{z} = z/H$.

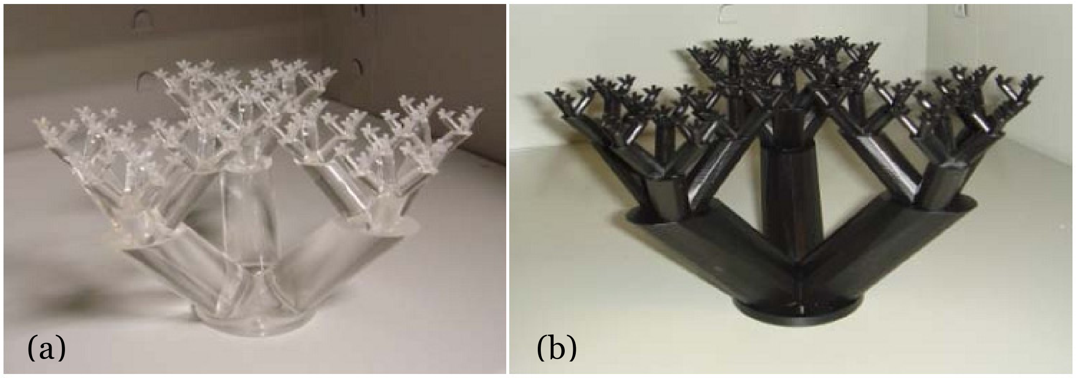

Figure 2.4 Photos of fractal tree model: (a) model made of material UOPTIC 2; (b) model made of non-transparent material.

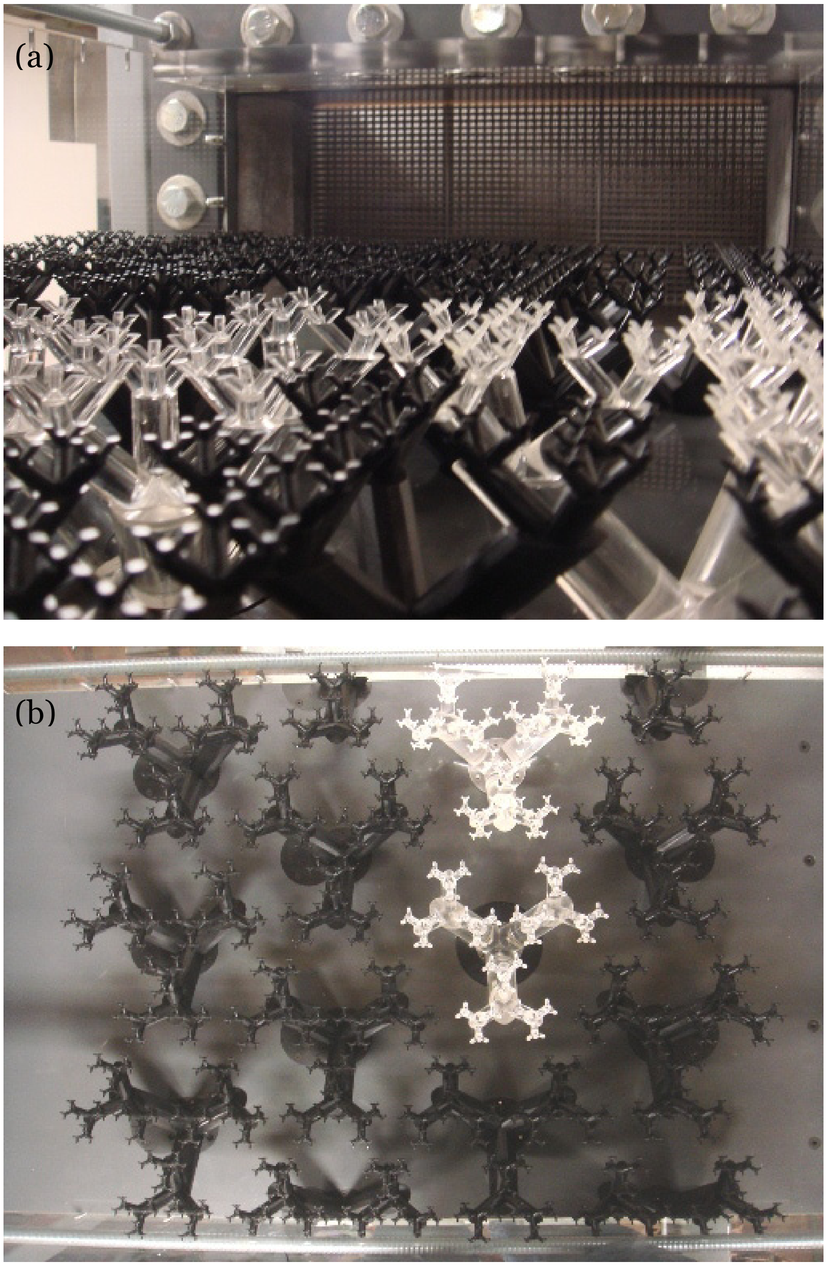

Figure 2.5 Canopy model with multiple fractal trees inside the test section. Perspective view (a) and top view (b) of the canopy. In (b), flow direction is from left to right.

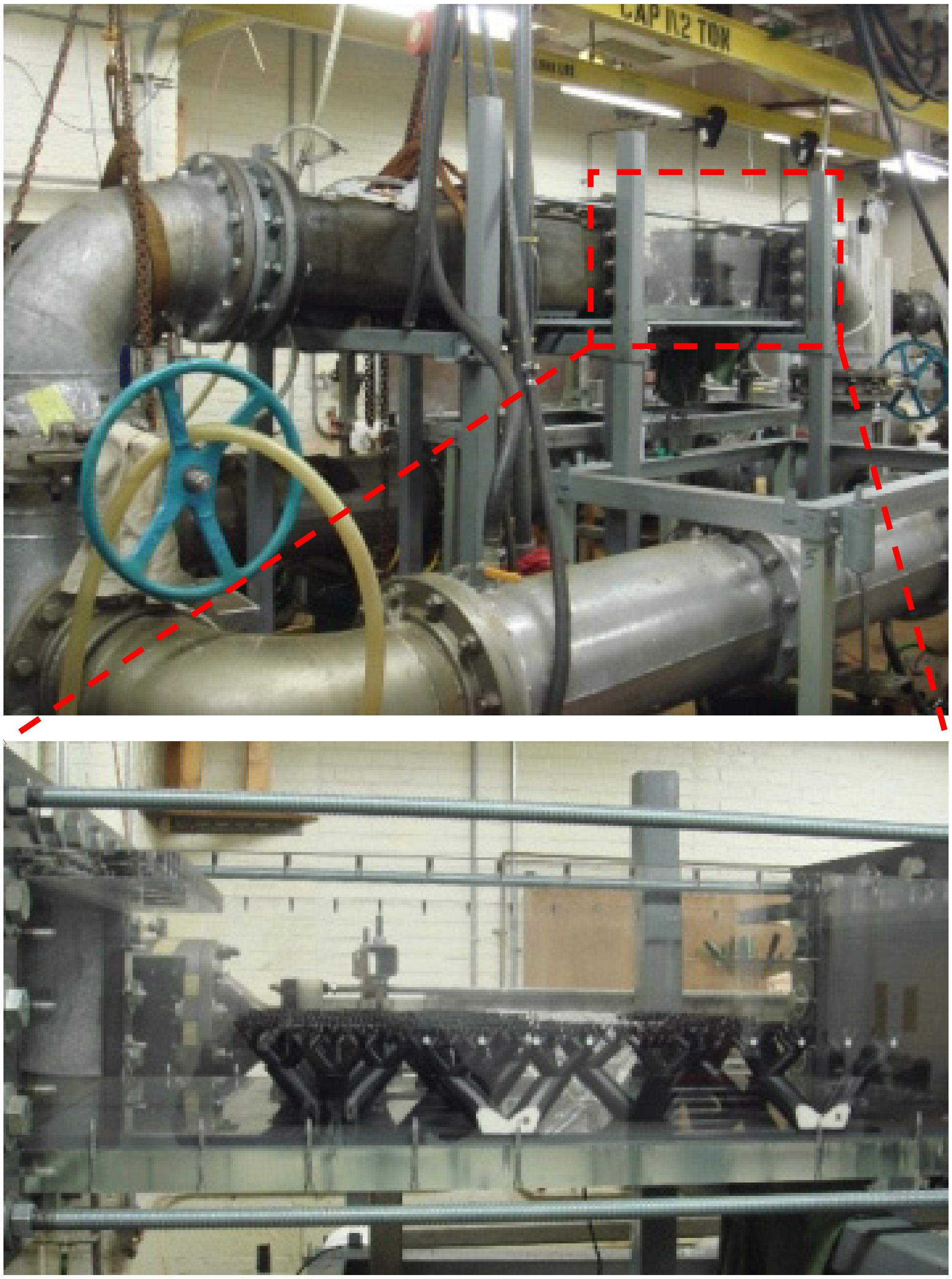

Figure 2.6 Photos of test facility in the Laboratory of Experimental Fluid Dynamics. Flow direction is from left to right.

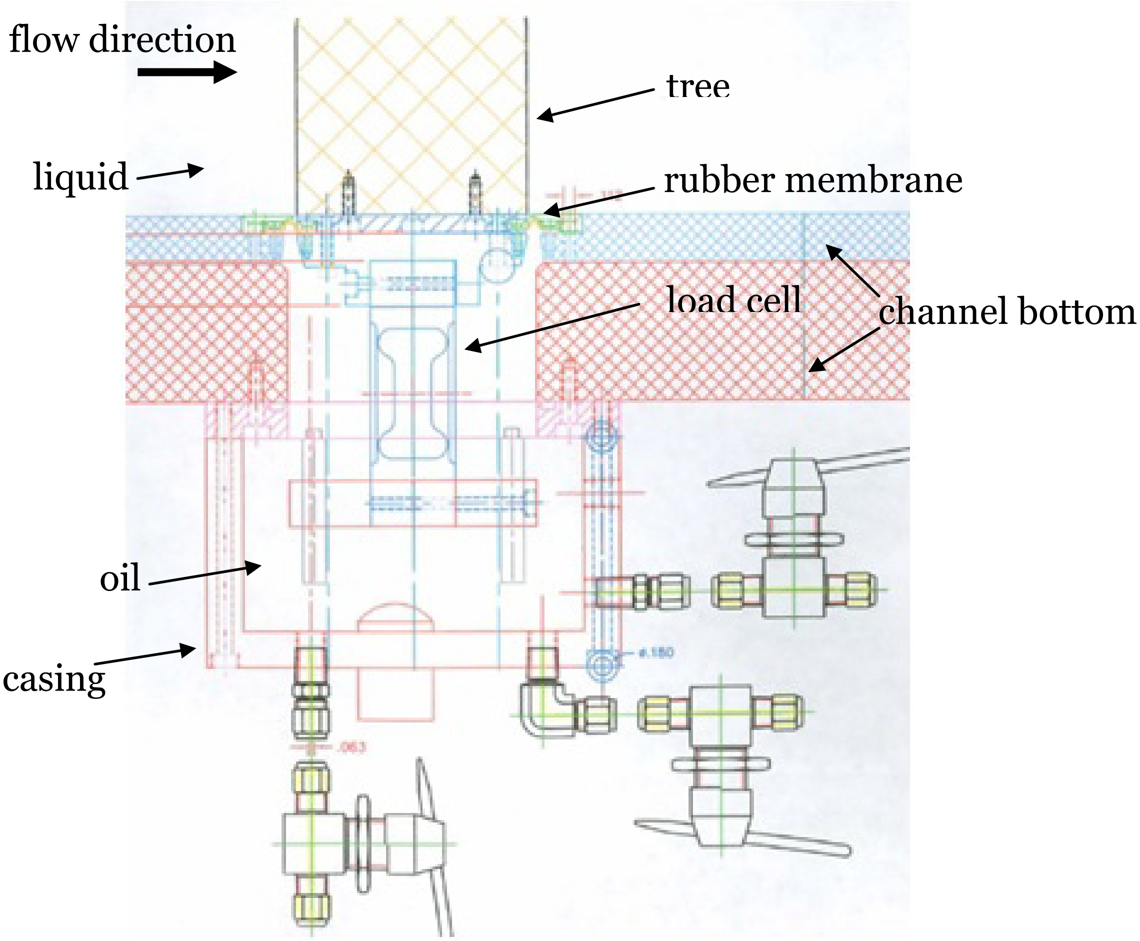

Figure 2.7 Design of the load cell setting.

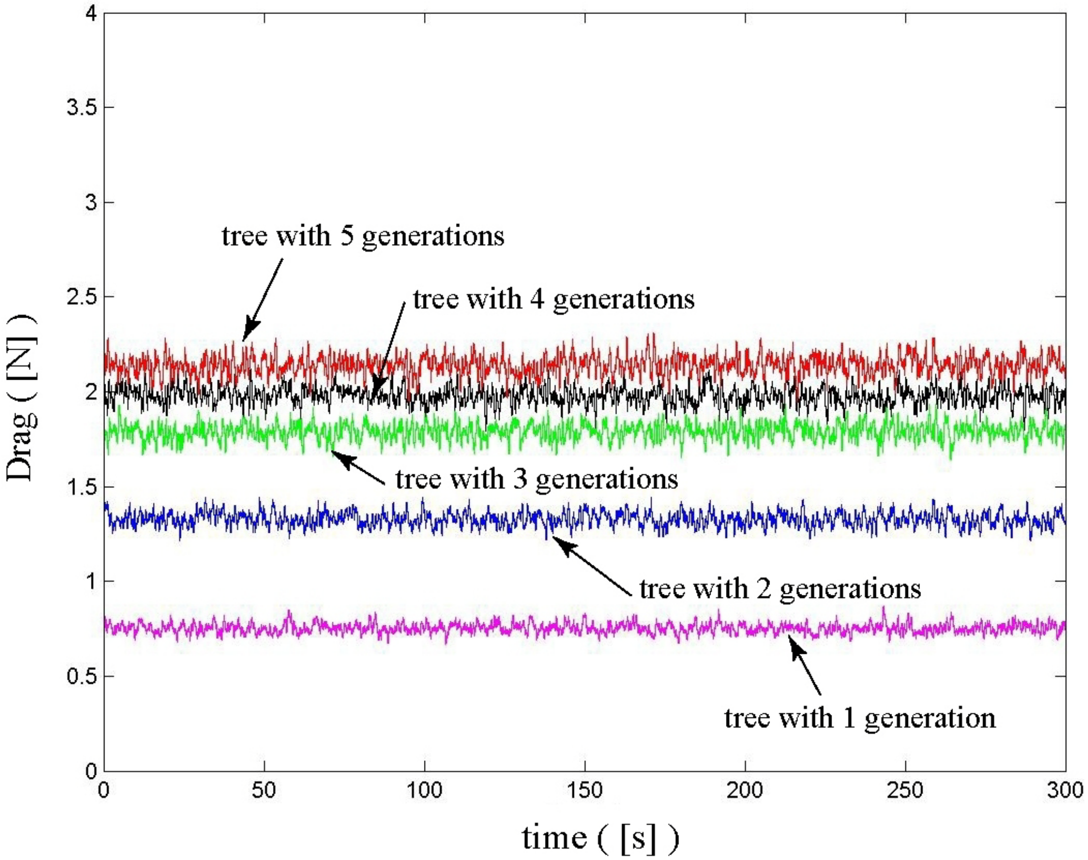

Figure 2.8 Typical force signals as a function of time. The data shown here are obtained from a single tree at flow speed of 1.3 m/s. Different lines indicate drag of trees with different branch generation numbers.

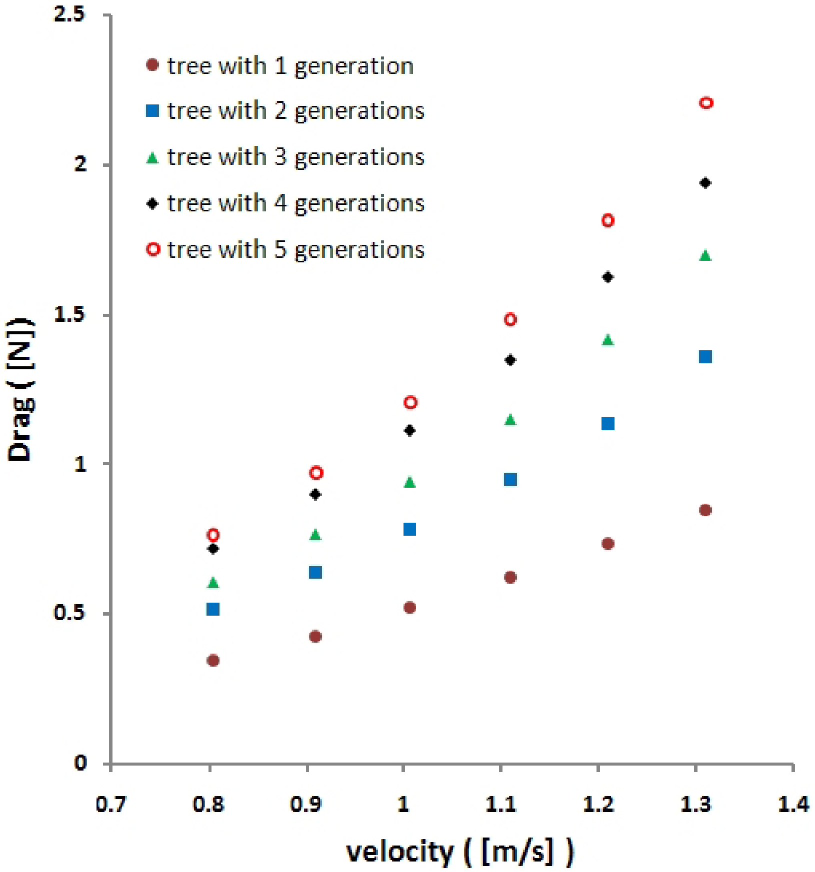

Figure 2.9 The measured drag of a single tree as a function of flow velocity. Different symbols represent tree with different generation numbers.

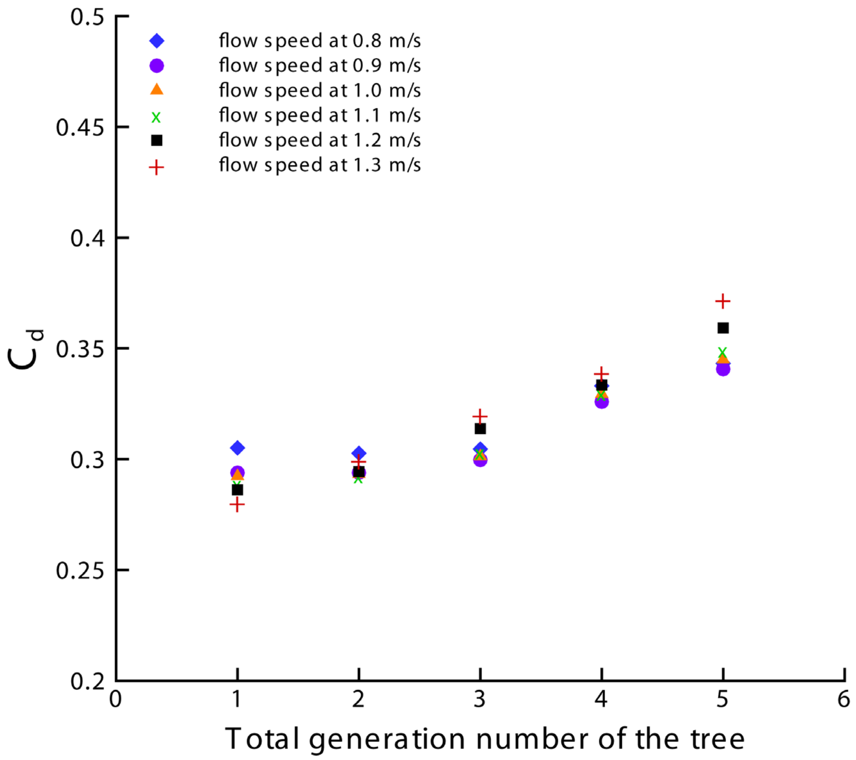

Figure 2.10 The measured drag coefficient for a single tree with different branch generations.

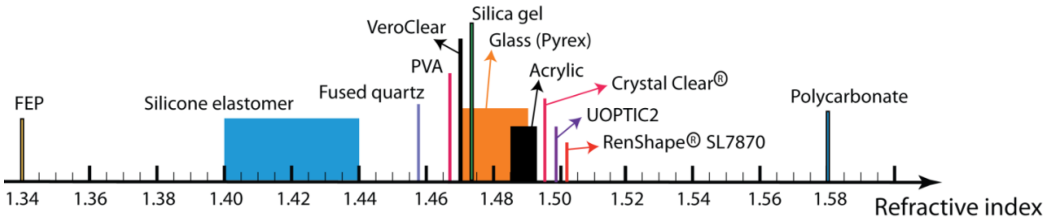

Figure 2.11 Refractive indices of typical transparent solid materials.

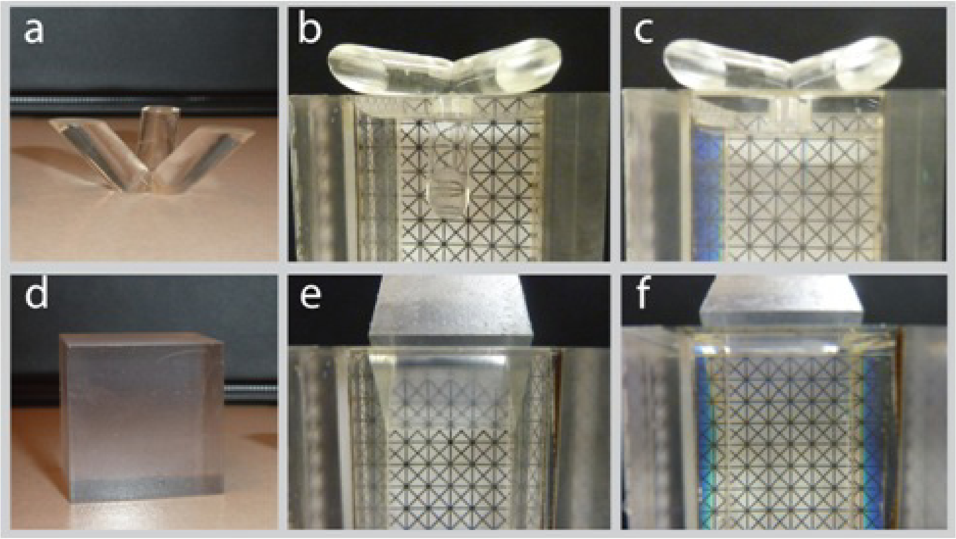

Figure 2.12 Test samples demonstrating index matching of hard materials that could be manufactured in complex shapes:(a)-(c) UOPTIC 2, and (d)-(f) RenShape®SL7870. In (b) and (e) the sample is inserted in water. Index matching is demonstrated in (c) and (f) using NaI solutions with refractive indices of (c) 1.499, and (f) 1.508.

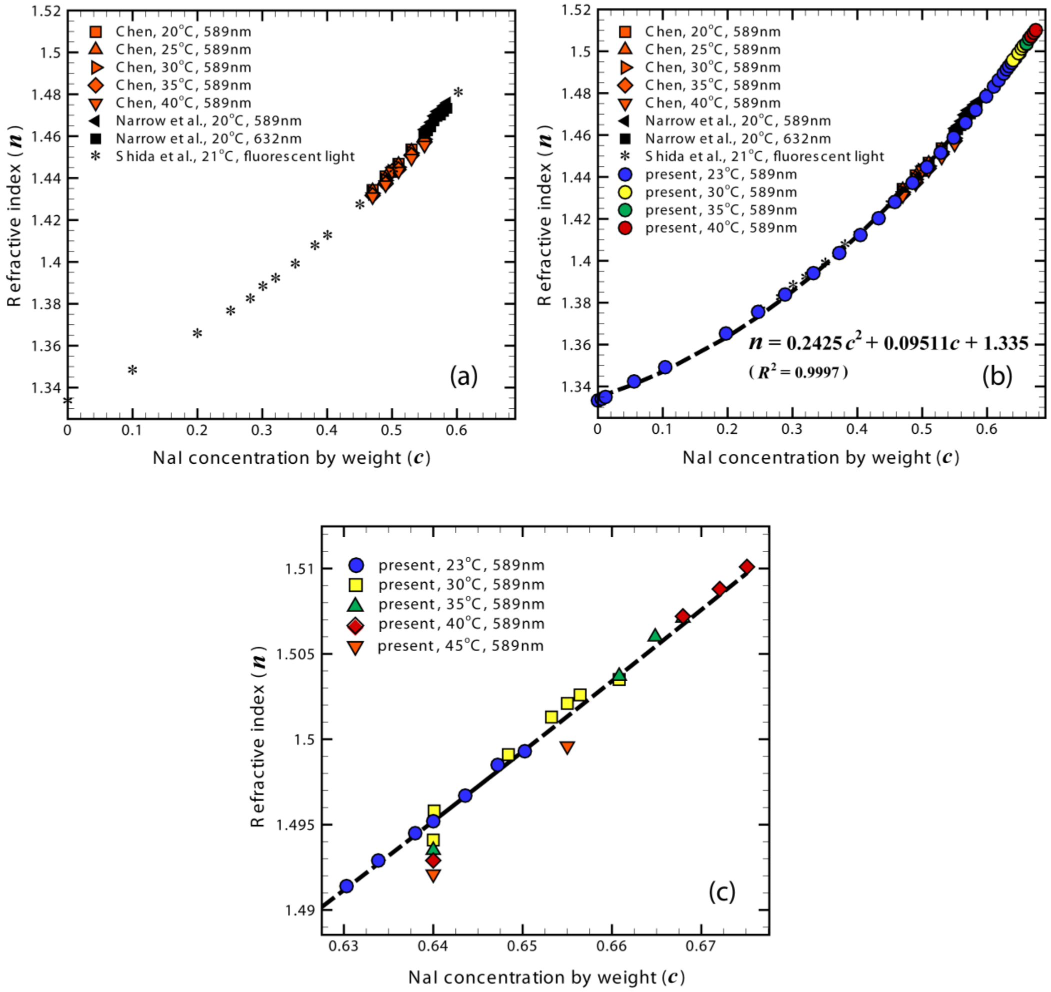

Figure 2.13 Refractive indices of sodium iodide solutions: (a) Previously published values; (b) the present results included; and (c) a magnified part at the present high concentration range aimed at showing temperature effects.

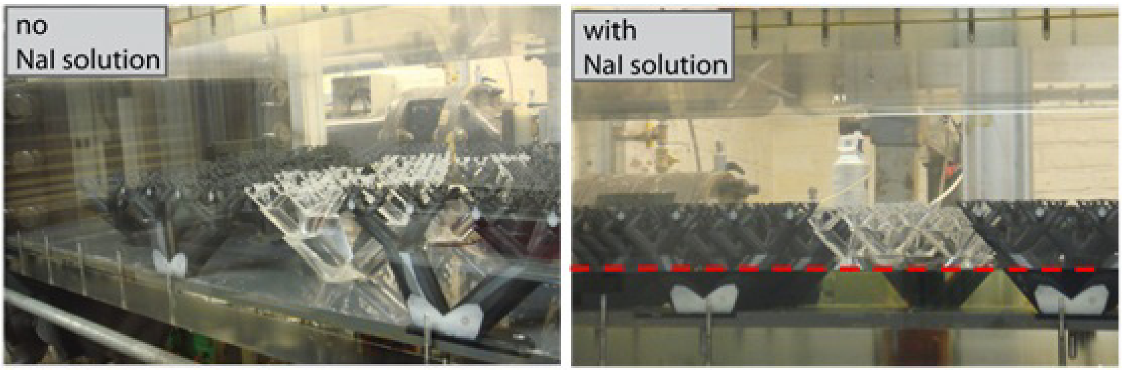

Figure 2.14 Index matching using sodium iodide (NaI) solution in the facility. (a) Two transparent trees made of UOPTIC 2 are visible. (b) With index matching in partially filled conditions, when the two trees become invisible below the solution level, indicated by red dashed line.

Table 2.1 Measured solubility at different temperatures and the refractive index of solutions at corresponding solubility.

Temperature	23˚C	30˚C	35˚C	40˚C
Solubility	65.0%	66.1%	66.8%	67.5%
Refractive index	1.499	1.503	1.507	1.510

Chapter 3. Near-Wake Structures behind a Single Fractal Tree

In this chapter, the near-wake structures behind a single fractal tree are discussed. The goal of this study is to answer the following questions: what is the overall structure of the turbulence in the wake behind a fractal tree? Is there a characteristic length scale describing the momentum transport across the wake? If so, how does the length scale change across different regions of the wake? And, can it be related to some geometric feature of the tree. We begin with a brief description of the experimental set-up in section 3.1. In section 3.2, results about velocity, turbulent Reynolds stresses and dispersive stresses are presented, while the Boussinesq eddy viscosity and Prandtl mixing length are discussed in section 3.3. Models for the mixing length are introduced in section 3.4.

3.1 Experimental set-up

A schematic layout of the experimental set-up is shown in Fig. 3.1. The fractal tree is installed at the centre of the channel, 870 mm behind the shear generator. The incoming velocity profile ($U(z)$) and the Reynolds stresses ($\overline{u'u'}_{in}$, $\overline{w'w'}_{in}$ and $\overline{u'w'}_{in}$), as measured by PIV on an *x*-*z* plane at the centre of the channel, are shown in Fig. 3.2. Quantities are normalized by U_H, the velocity at H ($U_H = 0.73$ ms^{-1}), and the Reynolds number based on U_H and H is $\mathrm{Re}_H = 71{,}300$. Based on the peak of the Reynolds shear-stress profile, the friction velocity is estimated as $u_* \approx \sqrt{-\overline{u'w'}_{in,\,peak}} \approx 0.08U_H$. As can be seen, the profiles of Reynolds stresses are similar to turbulent boundary-layer flow up to a height of about $z/H = 0.7$, but then they decrease and approach distributions more typical of isotropic turbulence in the core of the channel, with $\overline{u'u'}_{in} \approx \overline{w'w'}_{in}$ and $\overline{u'w'}_{in} \approx 0$.

The PIV measurements in the wake are conducted at 14 different *x-y* planes, parallel to the channel bottom, with these sampling planes located at $\hat{z} = z/H$=0.22, 0.32, 0.41, 0.50, 0.57, 0.63, 0.70, 0.77, 0.81, 0.86, 0.92, 0.97, 1.01 and 1.05, starting from 125 mm behind the tree centre. For PIV vector calculation, the final interrogation window size is 32×32 pixels, with 50% overlap. The resolved field of view of about 195×130 mm^2 contains 304×203 vectors, with a vector resolution of about 0.64 mm, which is smaller than the smallest branch diameter. As with z, we normalize the x and y coordinates by H: $\hat{x} = x/H$, and $\hat{y} = y/H$. For each plane, 2,500 image pairs are recorded to achieve good convergence of turbulence statistics, and with a recording frequency 1Hz, the total recording time per plane is about 42 min. A sample of the instantaneous velocity map is shown in Fig. 3.3, in which the mean velocity is subtracted to visualize the eddy structures. The associated tree cross-section at the same elevation is also shown, as a reference. In this map, the signature of the wakes and shear layers can be clearly identified and small eddies can be observed in the zoomed-in region. Detailed discussions of velocity fields and statistics are presented in the next section

3.2 Basic flow properties

Mean velocities and turbulence second-order moments are evaluated using ensemble averaging over the 2,500 vector maps, at each elevation. The 14 different PIV sampling planes are also sufficiently close to each other (typical distance is about 6 mm) to allow smooth interpolation of the statistical fields, for plotting purposes. The inverse-distance interpolation is applied in the *z*-direction to create a three-dimensional volumetric dataset. Mean streamwise velocity contours in the $\hat{y}$ - $\hat{z}$ plane at three different streamwise locations: $x/H \approx 1.33$, 1.96, and 2.59 are shown in Fig. 3.4a, which shows the changing shape of the wake and the vertical distribution of the streamwise velocity component in different regions. The wake shape follows the broad outlines of the fractal tree and displays general features of branching at different heights and generations. In the $x/H \approx 1.33$ plane, there is a clear low velocity region at $y/H \approx -0.5$ and $0.5 < z/H < 0.8$. This wake decays gradually downstream and becomes almost invisible at $x/H \approx 2.59$. On the other hand, at $x/H \approx 1.33$, $0 < y/H < 0.7$, and $z/H \approx 0.8$, two distinct low velocity regions are observed. As $\hat{x}$ increases, these regions tend to merge, and then continue to decay. Since the one-branch side of the tree ($y/H < 0$) is further away in the $\hat{x}$-direction from the PIV sampling planes than the two-branch side (Fig. 3.1b), there is a significantly greater velocity recovery in the one-branch side than that in the two-branch side.

From the 2D data, we can obtain three components of the full Reynolds-stress tensor, and their distributions are plotted in Fig. 3.4b-d. As with the mean velocity contour plots, coarse features of the tree shape can be recognized especially close to the tree (e.g., $x/H=1.33$). As x increases, the stresses decay; the high stress regions interact with the surrounding flow and then merge. The very non-homogeneous distribution of $\overline{u'u'}$ at $x/H=1.33$ becomes a nearly uniform field at $x/H=2.59$. Furthermore, the significant differences in magnitude between $\overline{u'u'}$ and $\overline{v'v'}$ that can be seen at $x/H=1.33$, diminish greatly by $x/H=2.59$, i.e. the turbulence becomes more isotropic. Besides merging and decay, one can observe clear correlations between the distributions of

Reynolds stresses and the gradients of the mean streamwise velocity. In the Reynolds shear-stress distribution, zero-crossings of $\overline{u'v'}$ occur at the wake centers, where the velocity has the strongest deficit (Townsend 1947; Tennekes and Lumley 1972), and the associated sign changes follow sign changes of the velocity gradient. The relations between the Reynolds stresses and velocity gradients are central to the classic eddy-viscosity models in general (Tennekes and Lumley 1972; Pope 2000), and to canopy flow applications in particular (Raupach and Thom 1981; Finnigan 2000; Poggi et al. 2004b). These relations are explored in more detail below.

To extract relevant information using a more compact representation than the entire 3D distributions, averaging in the spanwise direction, denoted as $\langle\ \rangle_y$, is applied at different downstream locations to the mean velocity and Reynolds stresses (Fig. 3.5). Spatial averaging is often used in canopy flows, for example, the plane averaging developed by Wilson and Shaw (1977) and Raupach and Shaw (1982), and the more general volume averaging introduced by Finnigan (1985) and Raupach et al. (1986). Although only one tree is utilized in the current study, we can imagine that the flow field is, at least qualitatively, the representative of very sparse canopies, where the interactions between trees are negligible. Figure 3.5a shows the spanwise-averaged velocity as a function of height for various downstream locations. The shape of this profile is similar to those reported by Seginer (1976) and Baldocchi and Meyers (1988). In the portion of the profile near the tree top ($0.5<z/H<1$), where the tree introduces large blockage, one can observe a significant velocity recovery, starting from a large deficit at x/H=1.33. On the other hand, the velocity at low elevations and above the tree does not change much with streamwise distance. At low elevations, since the branches are located relatively far from the measurement planes, the wakes already recover before they enter the sample area. At the top of the tree, the dominant free-stream flow imposes a fixed mean velocity.

The spanwise-averaged Reynolds stress profiles (Fig. 3.5b and d) show that, at very high elevation (0.9<*z/H*<1), $\left\langle \overline{u'u'} \right\rangle_y$ increases significantly as elevation increases. A distinct peak at the tree height can be identified for the normal components, i.e. $\left\langle \overline{u'u'} \right\rangle_y$ and $\left\langle \overline{v'v'} \right\rangle_y$, while at lower elevations (*z/H*<0.9), both normal components have very similar shapes, but $\left\langle \overline{u'u'} \right\rangle_y$ decays faster than $\left\langle \overline{v'v'} \right\rangle_y$. Their magnitudes become comparable already at *x/H*=2.28. The mean spanwise-averaged Reynolds shear stress, $\left\langle \overline{u'v'} \right\rangle_y$, is nearly zero due to cancellations of positive and negative contributions in the wakes.

Furthermore, one can calculate the dispersive fluxes, which arise when the time-averaged (here ensemble-averaged) mean momentum equation is additionally averaged in space (Finnigan 2000; Poggi 2004a). Following the notations used in Poggi et al. (2004a), in which a spatial deviation of any variable *a* is denoted as $\overline{a}'' = \overline{a} - \left\langle \overline{a} \right\rangle_y$, the dispersive fluxes for horizontal momentum transport, $\left\langle \overline{u}''\overline{u}'' \right\rangle_y$, $\left\langle \overline{v}''\overline{v}'' \right\rangle_y$ and $\left\langle \overline{u}''\overline{v}'' \right\rangle_y$, are shown in Fig. 3.6a-c. The $\left\langle \overline{u}''\overline{u}'' \right\rangle_y$ component increases with increasing elevation, reaches its maximum value below the tree top and then decreases. It also decreases along the streamwise direction due to the wake decay. The mean spanwise velocity component V in the wake is very small compared with the mean streamwise velocity component U .

As a result, the spatial deviation of spanwise velocity, $\bar{v}" = V - \langle V \rangle_y$, is also negligible, and thus the nearly-zero values of $\langle \bar{v}"\bar{v}" \rangle_y$ and $\langle \bar{u}"\bar{v}" \rangle_y$ can be expected. To illustrate the relative contribution from dispersive stresses compared with those of the Reynolds stresses in the streamwise direction, we plot their ratio $\xi = \langle \bar{u}"\bar{u}" \rangle_y \big/ \langle \overline{u'u'} \rangle_y$ in Fig. 3.6d. Although the values of both $\langle \overline{u'u'} \rangle_y$ and $\langle \bar{u}"\bar{u}" \rangle_y$ decrease along the streamwise direction (Fig. 3.5b and 3.6a), their ratios remain reasonably constant. Clearly, the contribution from the dispersive fluxes cannot be ignored. One should note that the dispersive fluxes are evaluated based on horizontal averaging over lines in the data plane, which covers only the near-wake of a single tree. As such the results are relevant to what is expected to occur in very sparse canopies. Poggi et al. (2004a) demonstrate that the dispersive fluxes are important for sparse canopies, where they quantify the importance of $\langle \bar{u}"\bar{w}" \rangle$, the contribution of dispersive flux to the mean momentum transport in the vertical direction. In subsequent sections, we focus on modeling of Reynolds shear stresses associated with the turbulence and transport in the transverse direction.

3.3 Boussinesq eddy viscosity and Prandtl mixing length

To model Reynolds shear stresses, the Boussinesq eddy-viscosity concept is widely utilized in turbulent shear flows (Pope 2000) as

$$\overline{u'_i u'_j} = -\nu_t \left(\frac{\partial U_i}{\partial x_j} + \frac{\partial U_j}{\partial x_i} \right),\ i \neq j, \qquad (3.1)$$

where ν_t is the (kinematic) eddy viscosity. For the present discussion where we focus on the transverse transport in the wake region, the relation is

$$\overline{u'v'} = -\nu_t \left(\frac{\partial V}{\partial x} + \frac{\partial U}{\partial y} \right). \tag{3.2}$$

Inside the wake, the streamwise gradient of the mean spanwise velocity, i.e. $\partial V / \partial x$, is much smaller (typically less than 5%) than the spanwise gradient of the mean streamwise velocity, $\partial U / \partial y$. As a result, we focus on the relation between $\overline{u'v'}$ and $\partial U / \partial y$, i.e., transport and gradients in the transverse direction. In most of the canopy turbulence literature, the Boussinesq eddy viscosity is obtained directly by assuming a linear relation between Reynolds shear stress and velocity gradients. There has been little discussion as to whether this linear relation holds, probably due to the lack of detailed experimental data over domains covering a large dynamic range of variations in Reynolds shear stresses and mean velocity gradients. The current PIV data can be used to answer part of this basic question for transport in the transverse direction, by analyzing scatter plots of $\overline{u'v'}$ versus $\partial U / \partial y$. In these plots, shear stress, velocity gradient and eddy viscosity are functions of x and z, and, for the Boussinesq eddy viscosity to hold, they should be related by

$$\overline{u'v'}(x, z) = -\nu_{t,xy}(x, z) \frac{\partial U}{\partial y}(x, z), \tag{3.3}$$

where the subscript xy in the eddy viscosity is used to emphasize that this definition relates to transport in the x-y plane. Such scatter plots can be obtained from the current data for different streamwise locations and elevations. Figure 3.7 presents four representative examples (out of 14×203 scatter plots) corresponding to two streamwise locations and two elevations. All these scatter plots display clear linear relationships between the Reynolds shear stresses and velocity gradients. The data obtained at *z/H*=0.41, which falls within the first generation height, are shown in Figs. 3.7a and b for *x/H*=1.79 and *x/H*=2.30, respectively. Similarly, scatter plots for the same streamwise locations, but at *z/H*=0.97, which falls in the fifth generation, are shown in Figs. 3.7c and d. The slopes of the nearly linear relationships change with elevations and with streamwise locations. For example, for a fixed $\hat{x}$, Figs. 3.7a and c (or Figs. 3.7b and d) indicate that the slope increases with increasing elevations. On the other hand, for a fixed elevation, Figs. 3.7a and b (as well as Figs3.7c and d), show that the slope decreases as *x* increases. Since eddy viscosity is the negative value of the slope, the changing slopes indicate variations in the eddy viscosity. The numerical value of each slope can be obtained by linear least-square regression, providing us with the values of eddy viscosity ($v_{t,\,xy}$) at 203 streamwise locations and 14 elevations.

The measured values of $v_{t,\,xy}\left(x,\, z\right)$ are shown in Fig. 3.8a, as vertical profiles at different streamwise locations. Generally, it can be seen that the eddy viscosity decreases with increasing elevation, with its value at the tree top being only about half of that at low elevations. This trend is in contrast with the increase in eddy viscosity inside canopies that has been reported for stripe canopy models (Raupach et al. 1986) and nylon-stalk canopy models (Brunet et al. 1994). Some studies involving other artificial canopies have reported constant eddy viscosities (Thom 1971; Novak et al. 2000). These previous results have been derived for vertical momentum transport and for canopy models in which only one single length scale is involved. However, for our model, in which multiple scales are imposed at different elevations, and in which we focus on momentum transport in the transverse direction, the trends might be different. A lack of isotropic eddy-viscosity behavior, as well as the multi-scale nature of the canopy elements, may account for the different trends. Based on the dataset obtained, we may explore the behavior of characteristic length scales, in particular, the mixing length. It is a key factor in canopy turbulence modeling and its behavior in the present wake flow behind a multi-scale object is of significant interest.

For a flow with dominant shear in the y-direction, the Prandtl mixing length for transport in the x-y plane, L_{xy}, is defined based on the eddy viscosity as

$$\nu_{t,\,xy} = L_{xy}^2 \left| \frac{\partial U}{\partial y} \right| . \tag{3.4}$$

Generally the absolute value of the velocity gradient $\left|\partial U / \partial y\right|$ is used to determine a relevant timescale and is a function of the three coordinate axes. Since the eddy viscosity deduced from our data is a function of x and z, and is obtained by averaging (fitting) in the y direction, it is appropriate to average also the velocity gradient magnitude in the y direction, at each x and z. Then, the length scale using the transverse mean velocity gradient can be obtained as follows

$$L_{m,xy}\left(x,z\right) = \left(\frac{\nu_{t,xy}\left(x,z\right)}{\left\langle \left| \partial U / \partial y \right| \right\rangle_y} \right)^{1/2} . \tag{3.5}$$

To emphasize that this mixing length is only relevant to eddy viscosity and transport relating stresses and velocity gradients in the *x*-*y* planes, we denote it with the xy subscript. The normalized mixing length, $\hat{L}_{m,\,xy} = L_{m,\,xy} \big/ H$, is plotted in Fig. 3.8b. For comparison, the eddy viscosity and mixing length in front of the tree are about $v_{t,\,xz} \big/ U_H H \approx 0.005$ and $\hat{L}_{m,\,xz} \approx 0.07$. These values are estimated from the peak of the shear stress profiles and the mean velocity gradients shown in Fig. 3.2. These two quantities describe the momentum transport in the vertical direction, instead of the horizontal transport upon which we focus in this paper. Comparing these values with those in Fig. 3.8, we can conclude that the horizontal momentum transport behind the tree is of comparable importance as the vertical transport in the boundary layer without the tree.

In Fig. 3.8b, some interesting trends can be observed as well. First of all, similar to the eddy-viscosity trends, the mixing length decreases as the elevation increases. This tendency is opposite to the trends observed in classical boundary layers, in which the length scale increases linearly with height, in accordance with the increasing eddy sizes away from the surface (i.e., $L_{xz} = \kappa z$, where $\kappa \approx 0.4$ is the von Kármán constant). Previous studies of vertical transport inside canopies have found or used either a constant mixing length (Cionco 1965; Seginer et al. 1976) or an increasing mixing length (Uchijima 1962; Cowan 1968). Although the presently measured mixing length is associated with transverse and not vertical transport, its decreasing behavior is still noteworthy in contrast to these prior results. As will be shown in the next section, the mixing length does not simply depend on the *LAI* or leaf area density, or on the scale of the individual branches at any given height, and is determined instead by a multiplicity of scales composing the tree. This observation is important, especially if one wants to use mixing length to model turbulence in tree wakes or in very sparse canopies with multi-scale elements.

Furthermore, for a fixed elevation, the mixing length increases with x. For the most part, this trend appears to be similar for all elevations. This behavior is reminiscent of the classical 2D plane wake, for which the evolution of the characteristic length scale with streamwise direction follows the 1/2 power law. One can seek an expression for the mixing length as a function of position (x, z) in the wake, as well as a function of detailed information about tree geometry (denoted below as "…"). Furthermore, based on the concept of plane wake expansion for which length scales grow as$x^{1/2}$, one may propose to separate the spatial dependence into two terms according to

$$\frac{L_{m,\,xy}}{H} = g\left(\frac{x}{H},\ \frac{z}{H},\ \ldots\right) \approx \left(\frac{x}{H}\right)^{1/2} L^{*}_{m,\,xy}\left(\frac{z}{H},\ \ldots\right) = \hat{x}^{1/2} L^{*}_{m,\,xy}\left(\hat{z},\ \ldots\right), \qquad (3.6)$$

where the factor $\hat{x}^{1/2}$ describes the dependence in the x-direction, and $L^{*}_{m,\,xy}\left(\hat{z},\ \ldots\right)$, which we will refer to as "compensated" mixing length, describes the dependence in the z-direction and tree geometry. The distribution of $L^{*}_{m,\,xy}$ is plotted against $\hat{z}$ in Fig. 3.8c. The profiles at different streamwise locations collapse into a single curve, showing that the growth of mixing length in the x-direction can be quantified quite well using the classical plane-wake growth rate. The trend of $L^{*}_{m,\,xy}\left(\hat{z}\right)$ in the z-direction, however, is quite non-trivial, and will be quantified in the following sections.

3.4 Scaling of mixing length

In this section, we address the question of what is an appropriate length scale derived from the tree geometry, which can be used to scale the measured mixing length at various heights in the wake. First, some possible scalings based on traditional length scales, such as the tree height, branch diameter, and leaf area density, are examined. Then, two models are proposed that are based on explicit knowledge about the multi-scale geometry of the tree. One model is derived in the spectral domain, and is based on the spectrum of the tree structure at different elevations. The second model is derived in the physical domain, and is based on the fractal length-scale distribution.

3.4.1 Scaling based on traditional length scales

The simplest approach to scale the mixing length is to use the known length scales of the tree geometry. Some examples are shown in Fig. 3.9, where the measured mixing length $L_{m,xy}$ at *x/H*=2 is presented as a reference. As already mentioned, the traditional boundary layer scale (κz) increases with the elevation, in contrast to the decreasing trend of the mixing length. The other possible scales show a decreasing trend with height, but the overall decrease differs greatly from that of the measured mixing length. For example, the normalized branch diameters (d/H) decrease from 0.3 to 0.035, by a factor of about 8. The normalized inverse of leaf area density ($\sim a^{-1}H$) also decreases by a factor of 8. In contrast, the measured mixing length ($L_{m,xy}/H$) decreases only by a factor of approximately 2, from 0.18 to 0.09. Many other possibilities have also been considered, but none give reasonable results. The difficulty is likely due to the fact that these traditional length scales simplify the problem too much and are based on a dominant single length scale, instead of using the multi-scale information about the fractal tree. In the tree geometry, different scales coexist. The single branches have their own dimensions (i.e., the diameter), but several single branches group into small clusters, which introduces a larger dimension. Then, several small clusters group into bigger clusters and so on. Because of this fact, a single length scale alone cannot fully represent the multi-scale information, and a more sophisticated way appears to be needed to determine an effective scale.

3.4.2 Model based on spectral distribution

In order to quantify the hierarchical features of the fractal tree, some type of superposition of all scales may be needed. To explore this possibility, we consider using the spectrum of the object, which describes the various scales present.

In Fig. 2.2, five representative cross sections are shown. Based on these distributions, the cross-section indicator function $I(x,\ y)$ is defined as $I=1$ when a point $(x,\ y)$ is located inside the object and $I=0$ outside. Then the indicator function is Fourier transformed in 2D, defining $\hat{I}(k_x,\ k_y)$ where k_x and k_y are the wavenumbers in the x-y plane. To convert the 2D results into 1D, which is easier to analyze, the radial spectrum of the indicator function, $E_I(k)$, is introduced by

$$E_I(k)\Delta k = \sum_{k<\sqrt{k_x^2+k_y^2}<k+\Delta k} \hat{I}(k_x,k_y)\hat{I}^*(k_x,k_y) \tag{3.7}$$

in which “ * ” indicates the complex conjugate of the function. The radial spectrum depends only on wavenumber magnitude. Four representative radial spectra, corresponding to tree cross-sections at selected elevations, are shown in Fig. 3.10. To highlight the interesting regions with various peaks, the spectra are shown only up to $k = 1000$ (rad·m^{-1}). Generally, at low elevations, most of the energy is concentrated at low wavenumbers (large scales). At higher elevations, the energy shifts towards higher wavenumbers and is distributed over a broader range with more peaks, due to the clustering and presence of smaller-diameter branches.

Based on the radial spectrum, a characteristic length scale that averages over all scales can be defined as the ratio $\int \frac{1}{k} E_I(k)\,dk \Big/ \int E_I(k)\,dk$. Such a length scale can be understood as a properly weighted superposition of length scales as represented by the spectrum. Furthermore, in order to consider the evolution of scales in the streamwise direction, we incorporate our finding from section 3.3, which indicated that the growth of scale follows a $\hat{x}^{1/2}$ power law. Based on the above information, the modeled mixing length derived from the radial spectrum is written as

$$\hat{L}_{s,xy}(\hat{x},\hat{z}) = L^*_{s,xy}(\hat{z})\,\hat{x}^{1/2} \tag{3.8}$$

where

$$L^*_{s,\,xy} = \alpha \frac{1}{H} \frac{\int \frac{1}{k} E_I(k)\,dk}{\int E_I(k)\,dk} \tag{3.9}$$

and α is a pre-factor of order unity.

In Fig. 3.11, we compare the modeled compensated mixing length $L^*_{s,\,xy}$ with the measured one $L^*_{m,\,xy}$ defined in Eq. 8. A pre-factor of $\alpha \approx 0.33$ appears to work well. Although there are some deviations at high elevations, the results shown in Fig. 3.11

confirm that the modeled length scale follows the decreasing trend of the measured mixing length quite well. It works well not only as a function of the vertical direction ($\hat{z}$) through Eq. 3.9, but also as a function of the various streamwise directions ($\hat{x}$) through Eq. 3.8. Since the model is based on the length scales of the tree itself and not on the flow, we do not know how to apply the model above the tree. Therefore, Fig. 3.11 shows the model applied only up to the tree height. One would like to develop a model that merges realistically the trends between the wake and the outside flow above the tree. However, we have insufficient data points for the outside flow above the tree to develop such a model at this stage.

The modeled length scale based on the spectrum Eq. 3.9 could, alternatively, be derived from the radial-averaged correlation function $C(r) = \frac{1}{2\pi r} \int_{|\underline{r}|=r} \langle I(\underline{x}+\underline{r}) I(\underline{x}) \rangle \, d\underline{r}$. As shown in Appendix A, the relationship is given by

$$\frac{\int \frac{1}{k} E_I(k) dk}{\int E_I(k) dk} = \frac{\int C(r) dr}{C(0)}, \tag{3.10}$$

where $C(r)/C(0)$ is the normalized correlation function. This relation is a 2D generalization of the more familiar relation often used in 3D (Monin and Yaglom 1975). Thus in principle these two methods are identical. However, the expression using the radial spectrum may be more insightful since the spectrum can be used to display the distribution of peaks as function of wavenumber (as in Fig. 3.10) and, as will be shown in the next section, the spectral approach is more convenient when cut-off length scales need to be applied.

3.4.3 Introducing cut-off scales due to wake interactions

Since many branches coexist at the same elevation, interactions among wakes generated by these branches should be considered. Especially for high elevations, where the diameters of individual branches are small, the wakes may not leave independent signatures, especially after the wakes have grown in size and began to interact. Instead, one should expect bigger wakes from the merging of small ones after a certain downstream distance. In other words, the appropriate cut-off scale in the flow might not correspond to the smallest branches, but instead correspond to the scale of clusters of branches whose wakes have merged.

In order to estimate the distance at which the wakes merge, $x_{m,\,i}$, we consider classic decaying 2D wakes generated by two objects with the same diameter d_i and with spacing S_i. Here S_i is the spacing between two branches at the height of the i-th generation. As detailed in Appendix B, using a linear superposition of two classical wake profiles shifted by S_i, one can show that,

$$\frac{x_{m,\,i}}{d_i} \approx 8\left(\frac{S_i}{d_i}\right)^2 . \tag{3.11}$$

In our geometry, we have $S_i \approx 3.5 d_i$ for any generation**,** which leads to a generation-independent dimensionless merging distance of $x_{m,\,i}/d_i \approx 100$. In the current experiment, the distance between the start of the data planes and the tree centre is 125 mm, while the end of the planes is at 255 mm. At such a distance, wakes generated by individual branches of the fifth generation have already merged over much of the measurement domain, and the flow does not contain individual wake signatures from this generation. Based on this reasoning, we apply a cut-off wavenumber, k_c, to Eq. 3.9 to avoid including branches that are so small that their wakes have already merged. Relating the wavenumber to the scale corresponding to the fourth-generation branches ($d_4 = 3.6$ mm), according to $k_c = \pi / d_4$, yields $k_c = 872\,\mathrm{rad\cdot m^{-1}}$. Based on this wake interaction argument, the integration of the spectrum should proceed only up to k_c:

$$L^*_{sc,\,xy} = \alpha \frac{1}{H} \frac{\int_0^{k_c} \frac{1}{k} E_I(k)\,dk}{\int_0^{k_c} E_I(k)\,dk}. \tag{3.12}$$

This expression defines another modeled length scale $L^*_{sc,\,xy}$ that includes a cut-off. Comparing with the results shown in Fig. 3.11, we find only minor changes at the top planes (not shown). For example at $z/H = 0.97$, the value of $L^*_{sc,\,xy}$ is about 0.034 while the value of $L^*_{s,\,xy}$ was about 0.025 without applying the cut-off. At lower elevations, the two model predictions are indistinguishable and therefore the plots are not shown. While in this case the results are not very different, a wake interaction argument should be applied especially if the length scales are to be obtained at larger downstream distances, where more wakes will have merged.

Furthermore, we remark that even for the fifth generation, the estimated merging distance of about 180 mm falls within the data plane, about midway through in the *x*-direction. So one would expect that near the tree (*x*<180 mm) no cut-off should be applied, while for *x*-locations further downstream (*x*>180 mm), the cut-off mentioned above should be applied. In fact, from the measured compensated mixing length $L^*_{m,\,xy}$ shown in Fig. 3.8c and Fig. 3.11, one can observe that the values at small *x* are slightly lower than at larger *x*. This trend is consistent with the above arguments, since $L^*_{s,\,xy}$ without a cut-off is smaller (because it includes contributions from smaller scales) than $L^*_{sc,\,xy}$ evaluated with a cut-off.

3.4.4 Model based on fractal size distribution

The approach described in the previous sections is based on a relatively complicated computation that involves the numerical evaluation of the radial spectrum of the object's cross sections. A simpler, but conceptually similar way is to account for the multiple scales by evaluating a weighted average over all the branch diameters. This approach enables us to invoke the fractal features of the object in determining an appropriate weight function. We propose to use the weighted average of scales as the characteristic scale, namely

$$r_f = \int rP(r)dr\,, \tag{3.13}$$

where $P(r)$ is the probability density function of scale r. For the fractal tree, the scales are discrete and thus the integration becomes a summation over generations "*i*". The individual scales are given by the diameters at generation "i". At height z_n, one obtains

$$l(z_n) = \sum_{i=1}^{n} d_i P_n(d_i), \tag{3.14}$$

where $l(z_n)$ is the characteristic length scale at height z_n corresponding to the n-th generation, d_i is the diameter of branches in the i-th generation and $P_n(d_i)$ is the normalized probability (weight function) for the diameter d_i at height z_n. For example the characteristic length scale for the second generation can be written as $l(z_2)=\sum_{i=1}^{2} d_i P_2(d_i)$. Since the tree has five generations, n ranges from 1 to 5.

To derive $P_n(d_i)$, we first imagine a 2D domain with size L. The number of square boxes with size r required to cover the whole 2D domain scales as $N_{tot} = (r/L)^{-2}$. Within this domain, there is an object with a fractal cross section. Based on the definition of fractal dimension, the number of boxes needed to cover this fractal object is $N(r) \sim (r/L)^{-D_f}$, where D_f is the fractal dimension. The fraction of the domain occupied by the fractal thus scales as $N(r)/N_{tot} \sim (r/L)^{2-D_f}$.

Now let us consider the fact that a cross section located at z_n not only contains branches with size d_n, but also groups of these branches organized into clusters of scales that are proportional to the parent branches of larger sizes, d_{n-1}, d_{n-2}, etc. Applying this feature to our problem, at the n-th generation, we have length scales $r_i = d_1,\ d_2 \ldots d_n$, where $d_i = d_1 (1/2)^{i-1}$. Then, the weight function (normalized to add up to unity at any given elevation) can be evaluated according to

$$P_n\left(d_i\right)=\frac{d_i^{2-D_f}}{\sum_{j=1}^{n} d_j^{2-D_f}}=\frac{2^{\left(D_f-2\right)\left(i-1\right)}\left(1-2^{D_f-2}\right)}{1-2^{\left(D_f-2\right)n}}, \tag{3.15}$$

where for the present tree, the fractal (similarity) dimension is $D_f = 1.585$. When this probability distribution is substituted in Eq. 3.14, we obtain the characteristic (average) length scale for the fractal tree at height z_n

$$l\left(z_n\right)=\sum_{i=1}^{n} d_i P_n\left(d_i\right)=\frac{\sum_{i=1}^{n} d_i^{3-D_f}}{\sum_{i=1}^{n} d_i^{2-D_f}}=\frac{1-2^{D_f-2}}{1-2^{D_f-3}}\frac{1-\left(2d_1/d_n\right)^{D_f-3}}{1-\left(2d_1/d_n\right)^{D_f-2}}d_1, \tag{3.16}$$

in which d_i is the diameter at the i-th generation. This procedure is a simple way to include multi-scale information in evaluating a characteristic length scale of the fractal tree, at any given height z_n. To relate it to the scales in the flow, again a pre-factor α of order unity is included. After considering the streamwise growth as in Eq. 3.6 and Eq. 3.8, the resulting mixing-length model based on the fractal size distribution is given by

$$\hat{L}_{f,xy}\left(\hat{x},\hat{z}\right)=L^{*}_{f,xy}\left(\hat{z}\right)\hat{x}^{1/2} \tag{3.17}$$

where

$$L^{*}_{f,\,xy}=\alpha\frac{d_1}{H}\frac{1-2^{D_f-2}}{1-2^{D_f-3}}\frac{1-\left(2d_1/d_n\right)^{D_f-3}}{1-\left(2d_1/d_n\right)^{D_f-2}}. \tag{3.18}$$

Similar to Fig. 3.11, $L^{*}_{f,\,xy}$ is compared to the measured compensated mixing length $L^{*}_{m,\,xy}$ in Fig. 3.12, where the same pre-factor $\alpha \approx 0.33$ is chosen. The agreement between these two quantities is in fact slightly better than the model based on the radial spectra. The model not only captures the decreasing trend of the mixing length in the vertical direction through Eq. 3.18, but also represents the growth of the mixing length in the streamwise direction through Eq. 3.17. Since the value of n is a discrete integer for each generation, elevations at the same generation with a fixed n give rise to a piecewise constant mixing length.

Next, we introduce a continuous model by allowing ℓ_m to change gradually in the vertical direction. The relationship between the scale and generation number is $2d_1/d_n = 2^n$. Also, the vertical location at the top of the n th generation is $z_n = H_1 \sum_{i=0}^{n-1} (1/2)^i = 2H_1[1-(1/2)^n]$ where H_1 is the height of first generation. Therefore $2^n = (1 - z_n/2H_1)^{-1}$, a term that can be also written as function of the continuous height z. By using this relation instead of $2d_1/d_n$ in Eq. 3.18, a continuous version of Eq. 3.18 can be written as

$$\ell_c(z) = d_1 \frac{1-2^{D_f-2}}{1-2^{D_f-3}} \frac{1-(1-z/2H_1)^{3-D_f}}{1-(1-z/2H_1)^{2-D_f}}. \tag{3.19}$$

The scaled mixing length then can be approximated by $\ell_{m,c}(z) = \alpha_c \ell_c(z)$. The result of this continuous model ($\alpha_c = 0.33$) is compared with measured mixing length in Fig. 3.13. It captures the measured distributions quite well, without the discrete steps. As argued in Bai et al. (2012), the good agreement between such a scale superposition-based model and the data confirms that the mixing properties in the wake of this kind of fractal tree must take into account the various hierarchical clusters of branches present at each height.

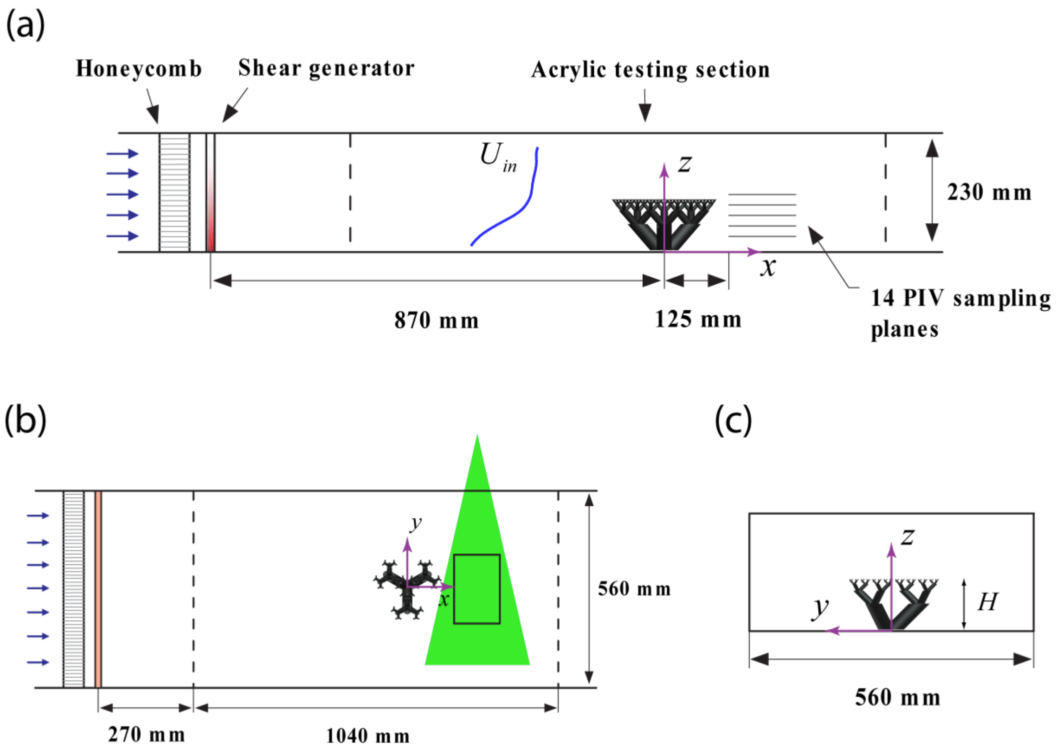

Figure 3.1 Three views of the flow facility: (a) side view; (b) top view and (c) front view.

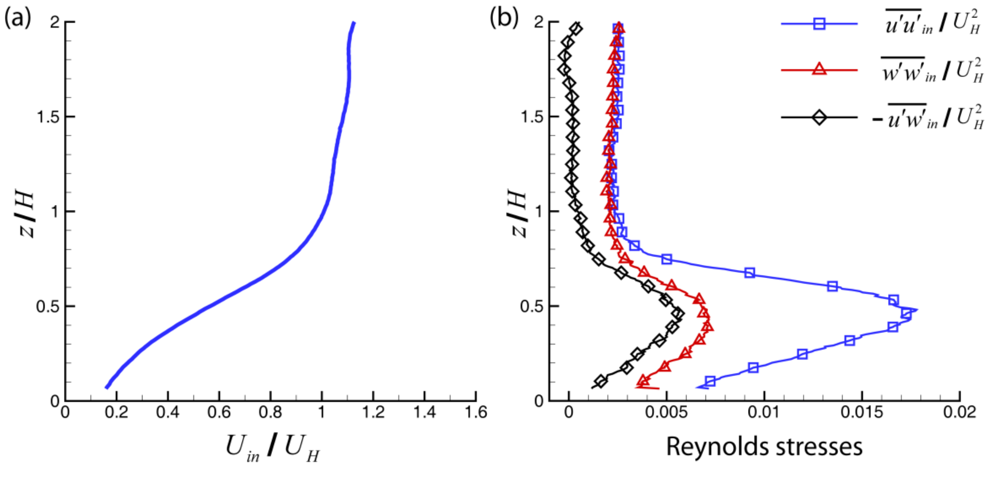

Figure 3.2 Incoming profiles of mean streamwise velocity (a) and Reynolds stresses (b).

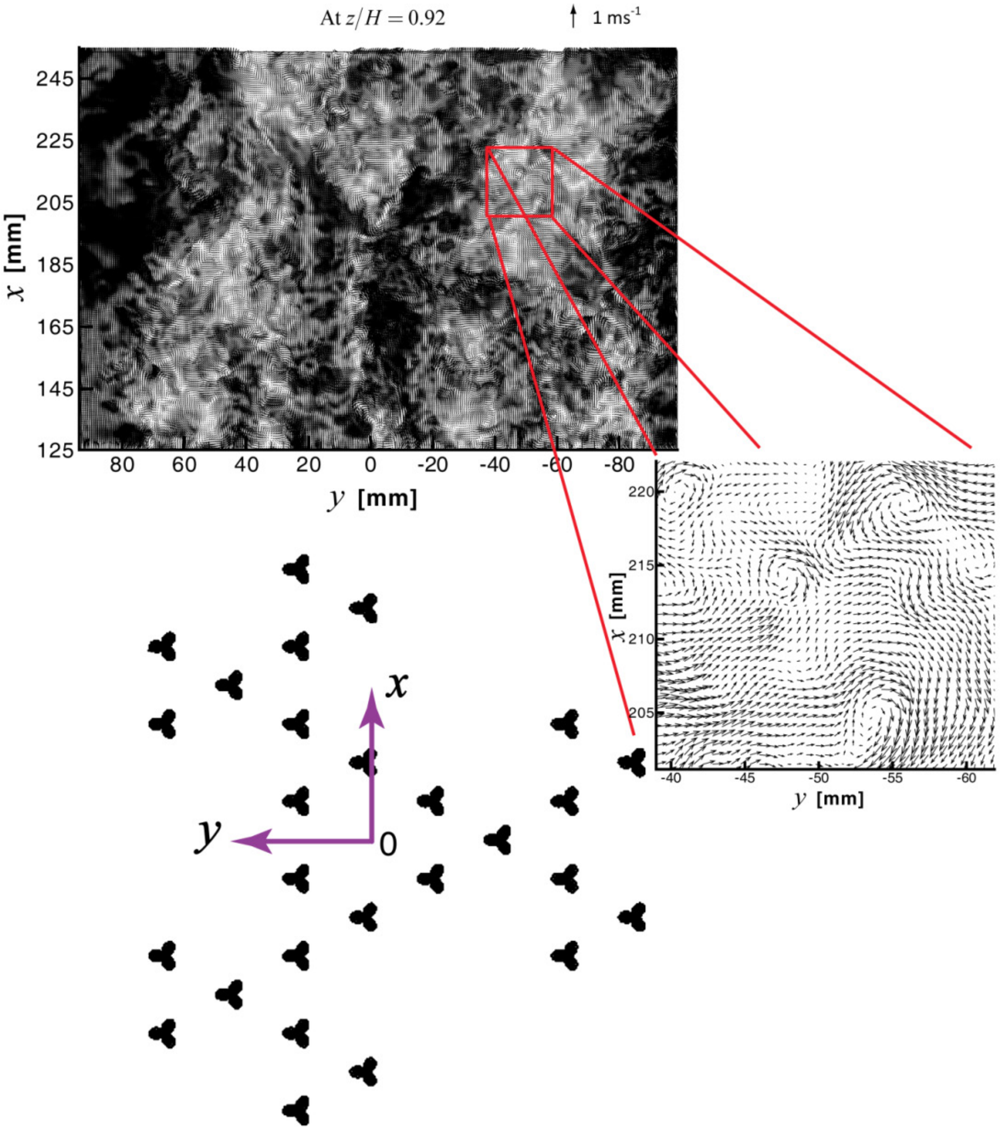

Figure 3.3 Sample map of instantaneous velocity vectors as obtained from PIV on 304×203 vectors at $z/H = 0.92$. The mean velocity has been subtracted. The zoom-in to the right shows small-scale eddies, while the tree cross-section upstream of the vector map is shown below the vector map.

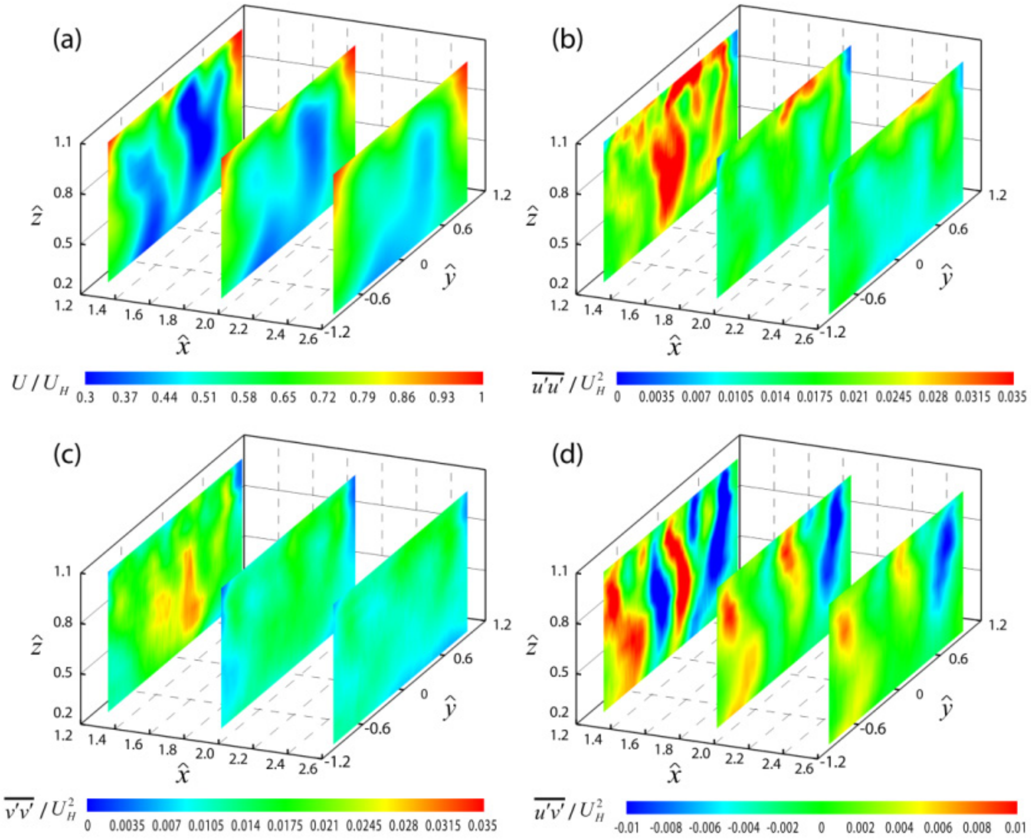

Figure 3.4 Contour plots of mean streamwise velocity (a) and Reynolds stresses at different streamwise locations (b)-(d).

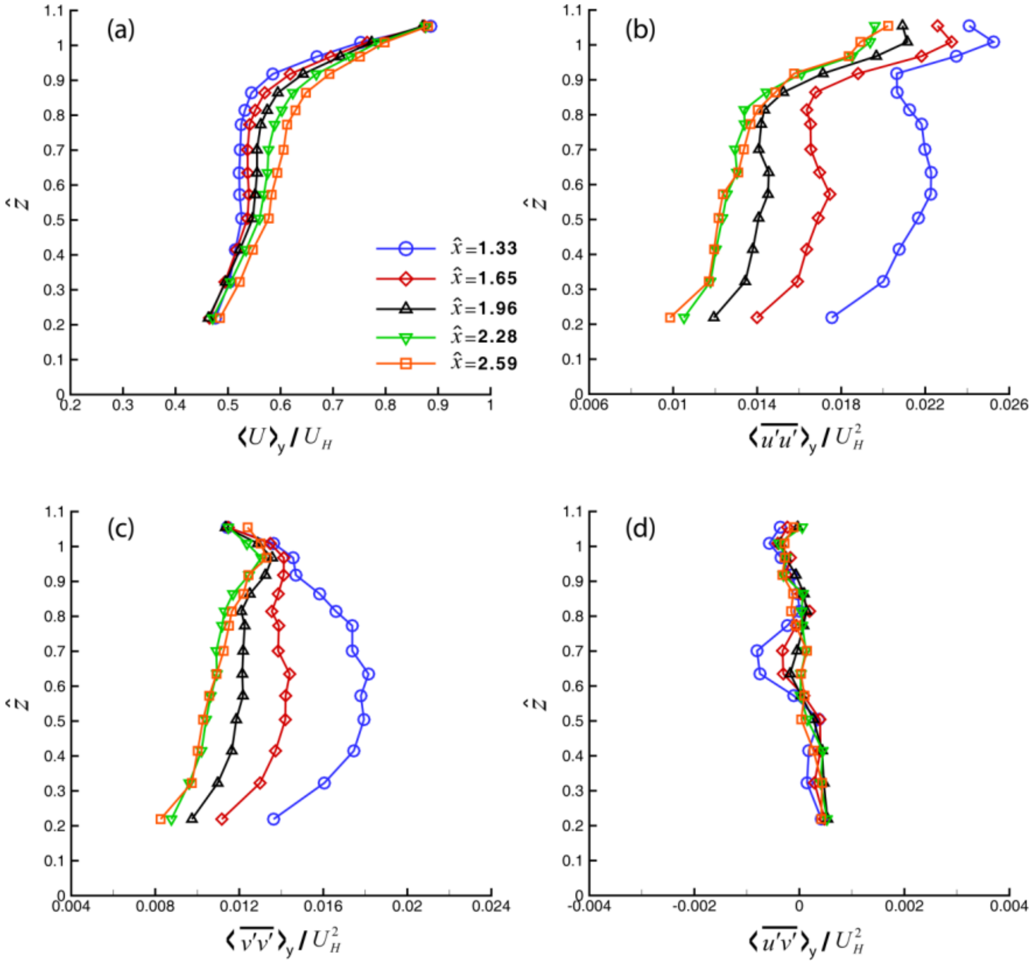

Figure 3.5 Profiles of mean velocity (a) and Reynolds stresses (b)-(d) after spanwise averaging in the *y*-direction.

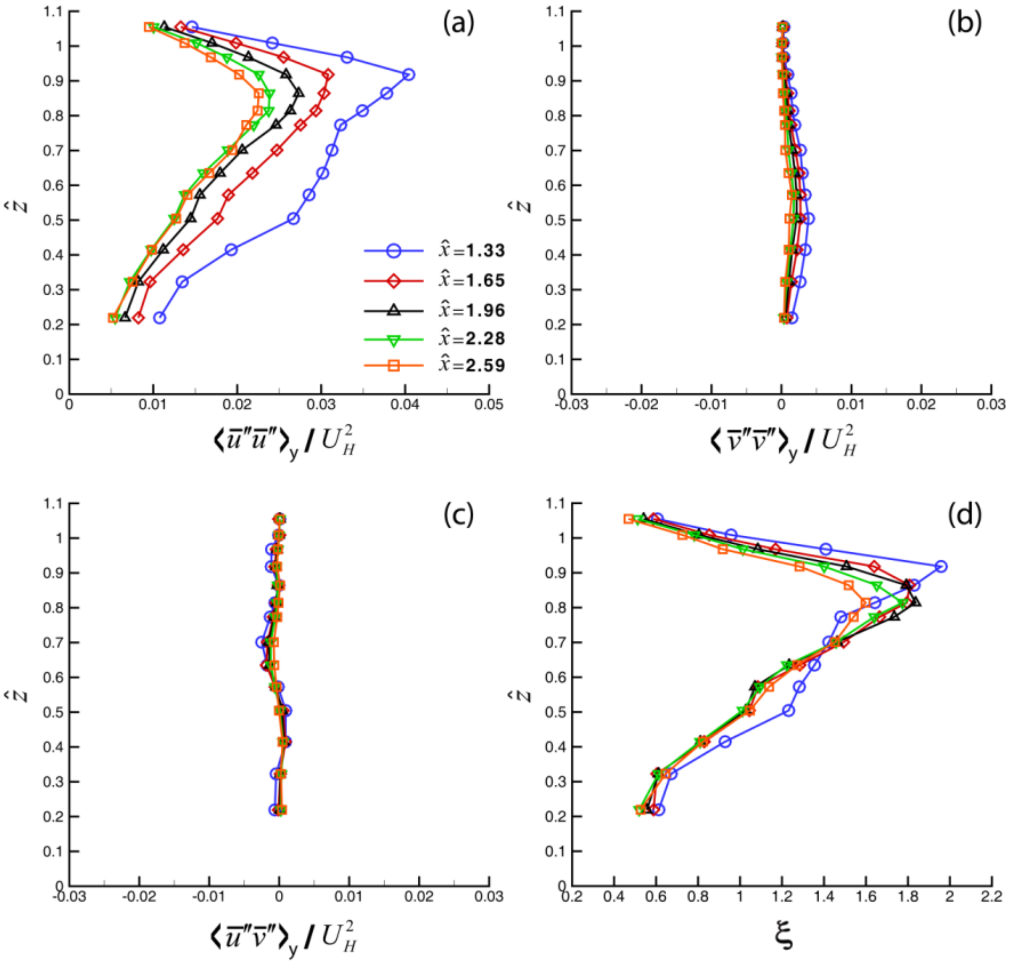

Figure 3.6 Profiles of dispersive fluxes (a)-(c) and ratio of streamwise dispersive flux to Reynolds stress in the streamwise direction (d).

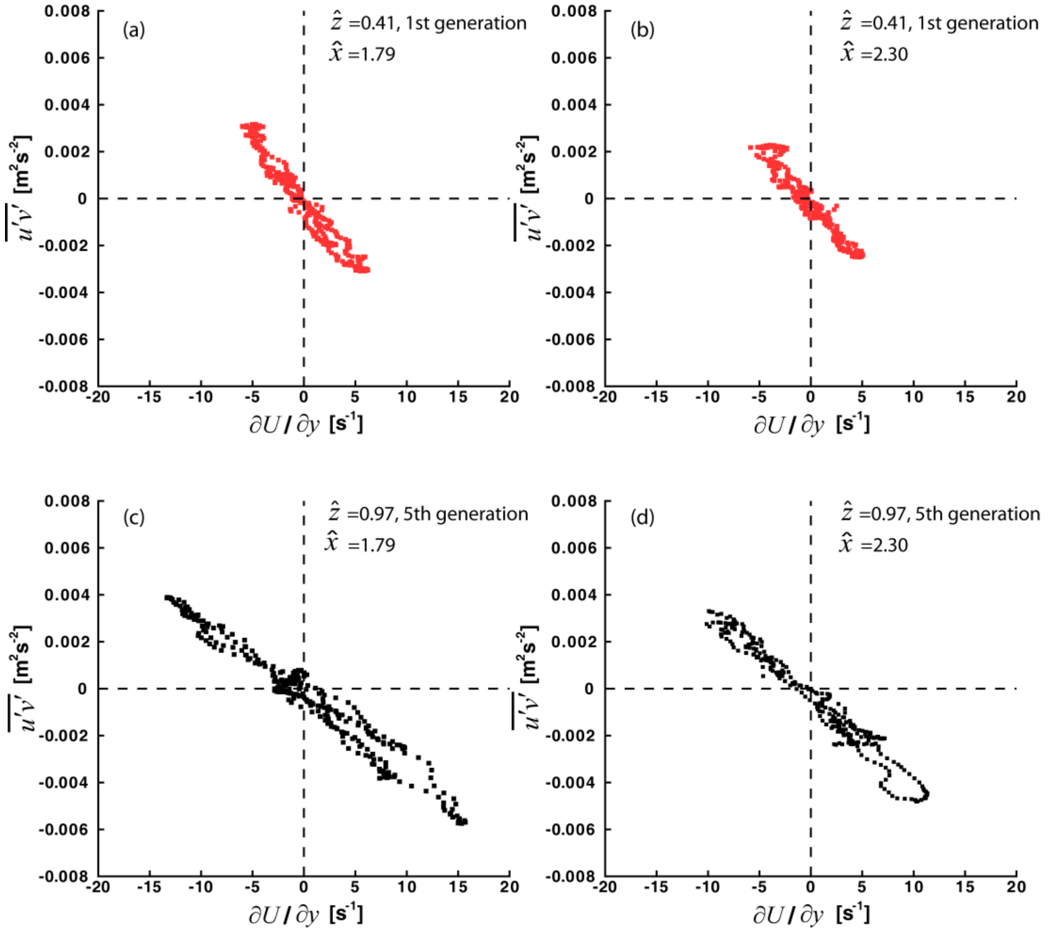

Figure 3.7 Scatter plots for mean velocity gradient and Reynolds shear stresses. Each point represents result at different spanwise locations (*y*).

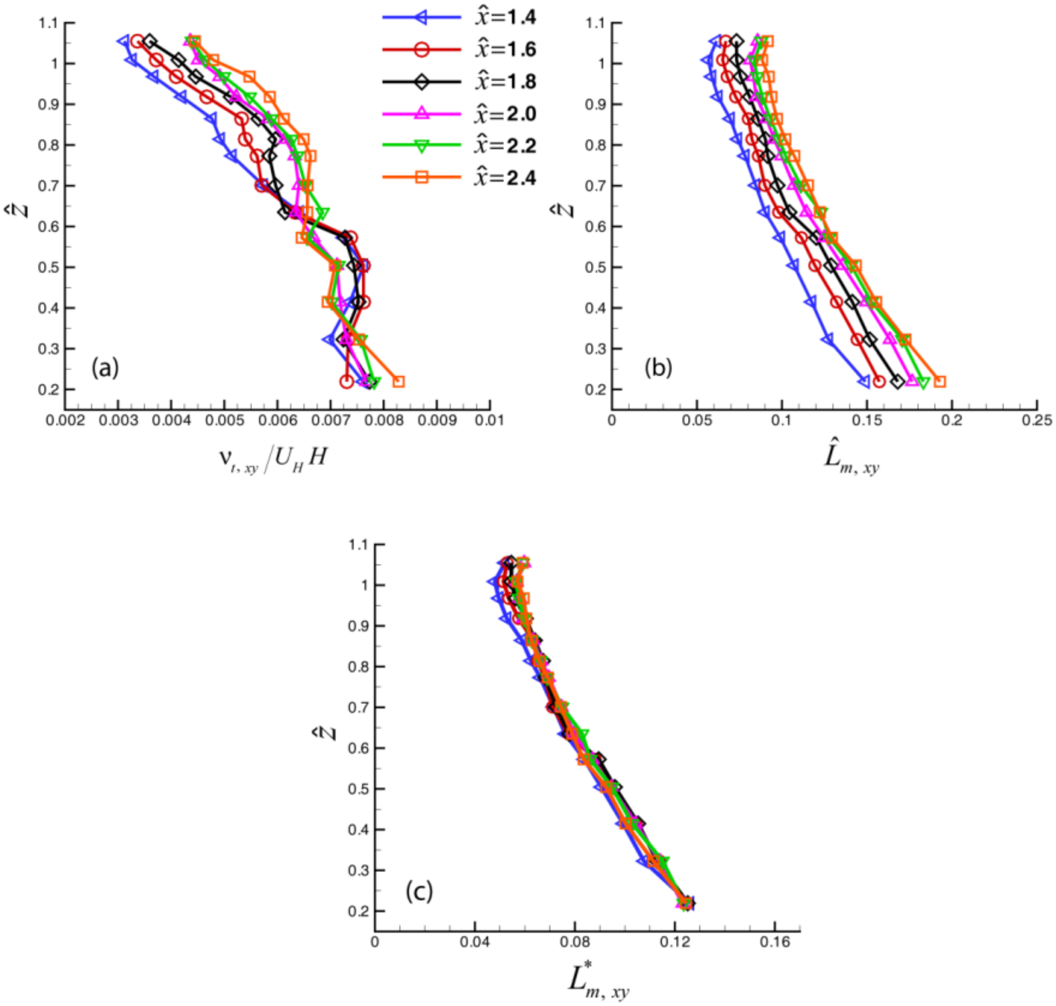

Figure 3.8 Measured eddy viscosity (a); mixing length (b); and compensated mixing length based on the plane wake theory (Eq. 3.6).

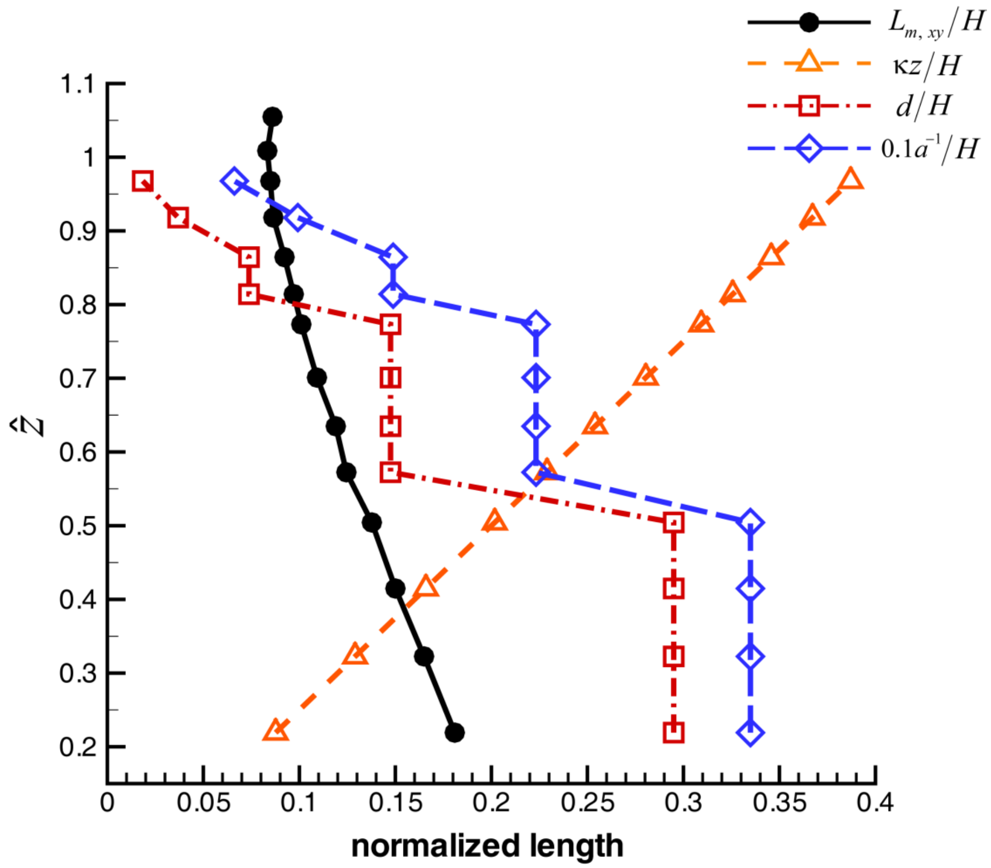

Figure 3.9 Length based on traditional scales, as functions of height. The lines show the measured mixing length at $\hat{x} = 2$, κz, branch diameter (*d*) and a scale proportional to the inverse of the leaf area density. The length scales are normalized by the tree height.

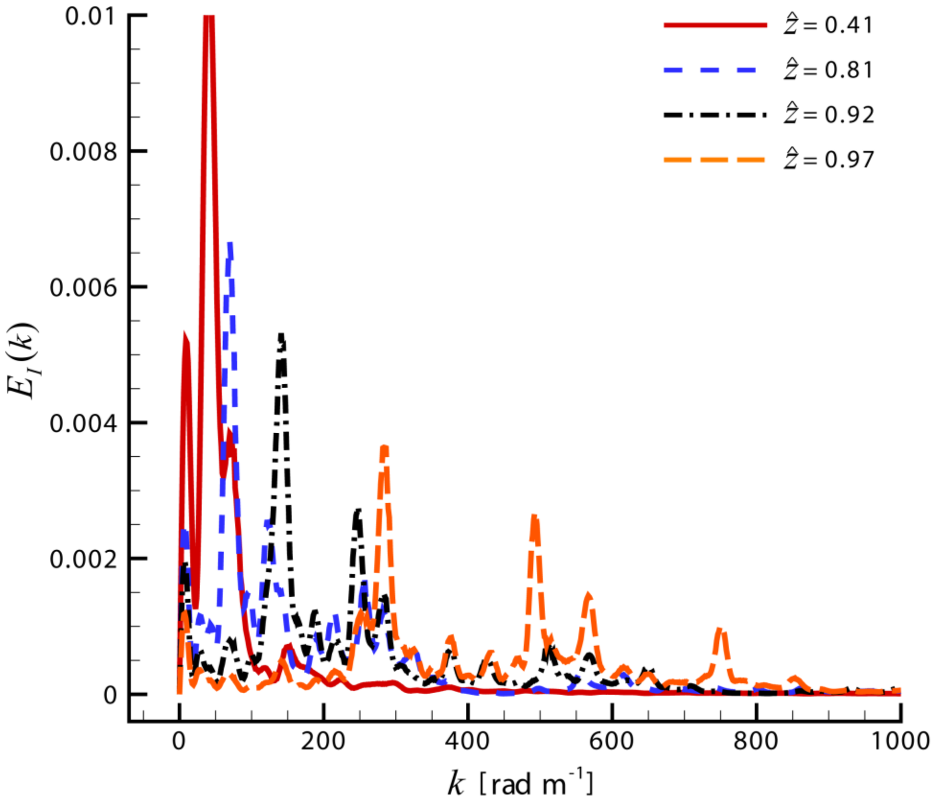

Figure 3.10 Radial spectra of the cross-section indicator function at four elevations.

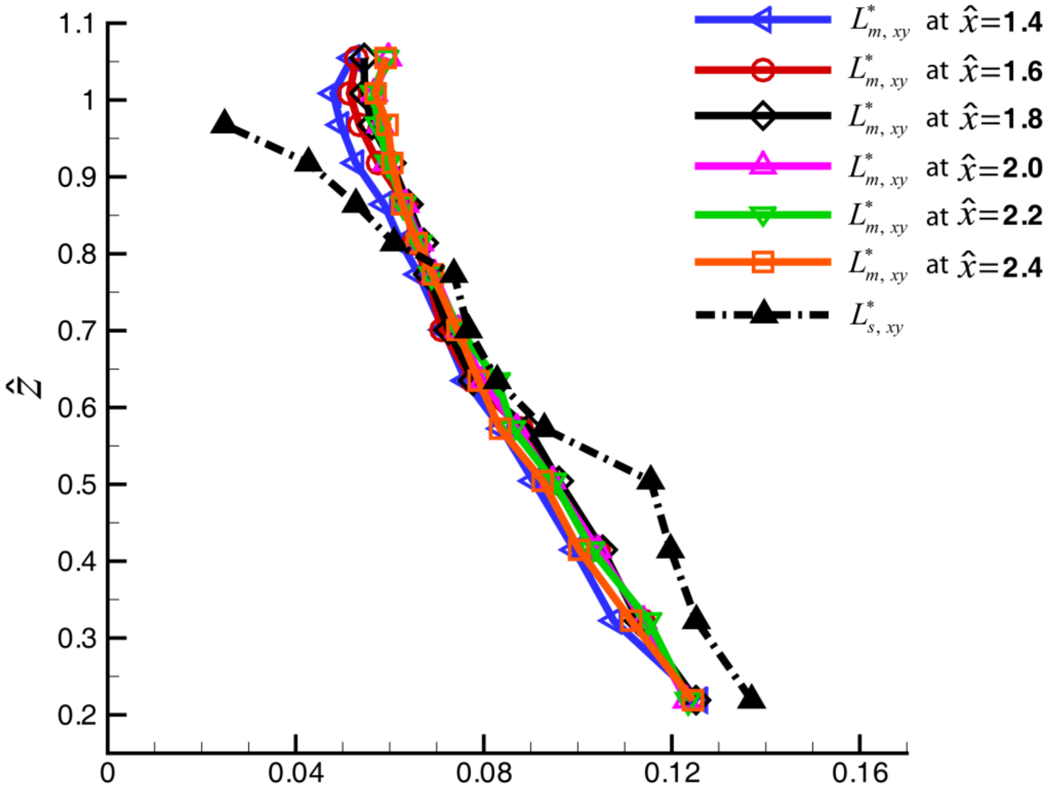

Figure 3.11 Comparison of the compensated mixing length to the model based on radial spectra, $L^*_{s,\,xy}$, as defined in Eq. 3.9.

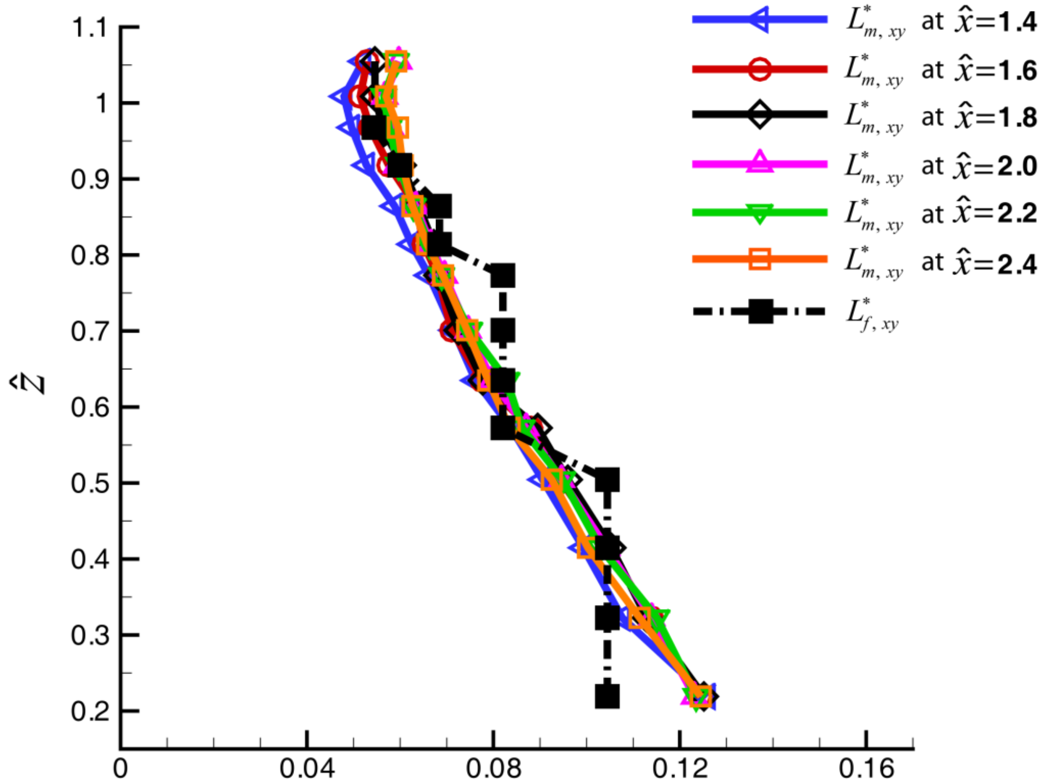

Figure 3.12 Comparison of the compensated mixing length with the fractal model based on the size distribution, $L^*_{f,xy}$, as defined in Eq. 3.18.

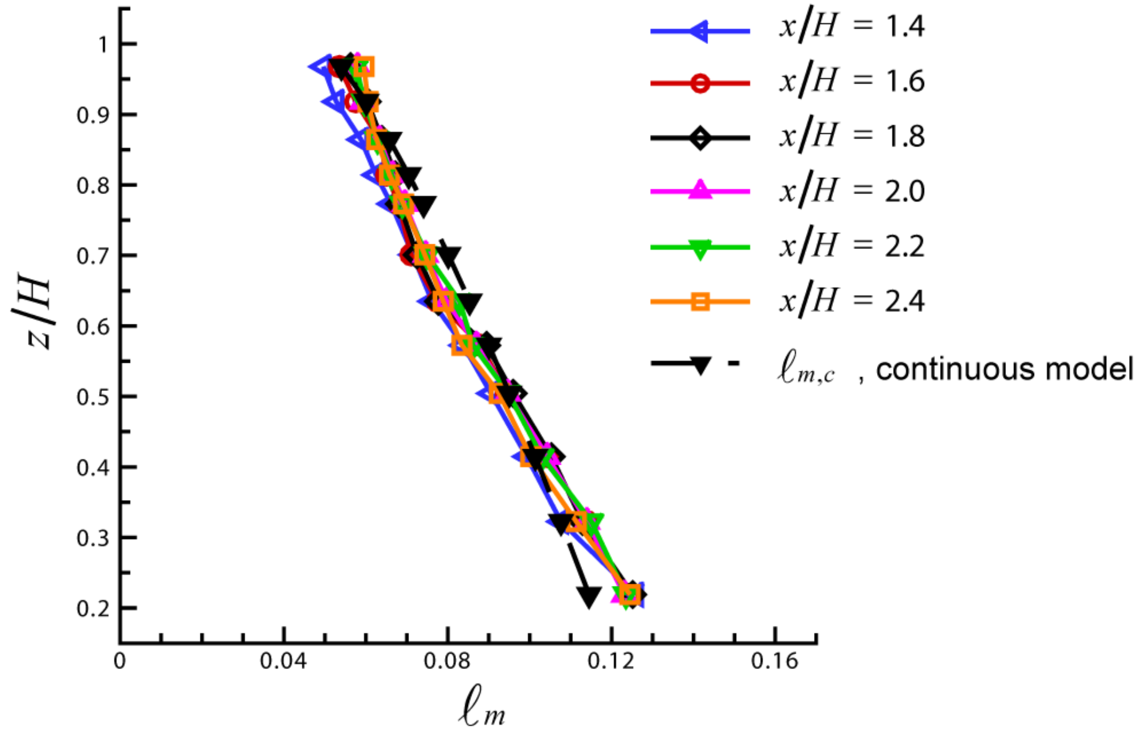

Figure 3.13 Improved mixing length model proposed in Eq. 3.19, in which the vertical dependence is made continuous rather than discrete.

Chapter 4. Spectral Energy Fluxes in Turbulence Generated by a Single Fractal Tree

In Chapter 3, we show that eddy-viscosity and mixing length concepts could be applied successfully to describe transverse transport of streamwise momentum, and that the measured mixing length could be predicted using a model based on superposing relevant branch length-scales at various heights. The focus of that study is on momentum transfer in the near-wake behind the fractal tree. It does not address the issue of the energy cascade process and the intrinsic structure of turbulence. Some new questions of interest are the following: how do the multiple scales modify the energy cascade process? Can a characteristic length-scale still be defined to collapse physical quantities that are directly relevant to the energy cascade?

In this chapter, we analyze the data obtained from Chapter 3, and specifically focus on the energy cascade in this flow and its associated characteristic scales. The measured energy flux and net energy injection rates are discussed in detail, along with tests to verify whether the mixing length model developed to describe momentum transport could also succeed in collapsing quantities of relevance to the energy cascade.

4.1 Spectral energy flux

To study the energy transfer corresponding to various branch-generations, we focus on the data at five elevations, which correspond to each of the five generations of the tree, namely at $z/H = 0.50$, 0.70, 0.86, 0.92, and 0.97, for generations $n = 1$, 2, 3, 4 and 5, respectively. The locations of these planes are indicated by lines in Fig. 4.1c. As one can see it from their cross-sections in Fig. 4.1d to h, each plane contains three large patterns, which correspond to the three big branches of the first generation, and three clusters with many small branches at higher elevations. We choose to study these planes since the centers of the $x-y$ plane projections of the three large patterns coincide with each other. The vector fields are then analyzed based on the filtering framework of relevance to Large Eddy Simulations. In this approach one decomposes the flow field into resolved and unresolved parts. As an example, figure 4.2a shows an instantaneous PIV vector map where the ensemble averaged velocity in that plane has been subtracted to visualize the eddying structures. When the filter with $\Delta = 6\delta = 3.84$ mm (where Δ is the filter size and δ is the vector spacing) is applied in Fig. 4.2b, only motions with relatively large scales can be observed while contributions from small scales have been eliminated. In the analysis, the data are spatially filtered using a box-filter, but the choice of the filter shape does not significantly affect the energy flux, as discussed by Liu et al. (1994) and Domaradzki and Carati (2007). We use box-filters at nine different scales, i.e. $\Delta/\delta =$ 6, 8, 10, 12, 16, 20, 24, 32 and 40. In order to determine whether these filters are located in the inertial range of turbulence, we evaluate the energy spectra as a reference.

In Fig. 4.3, two transverse spectra along the spanwise direction at $x/H = 1.4$ are shown, for two representative elevations $z/H =$ 0.50 and 0.92, respectively. The vertical lines indicate the wavenumbers corresponding to the above-mentioned filters scales. After obtaining the filtered velocity, $\tilde{u}_i$, for each filter size, the mean subgrid-stress (SGS) flux of kinetic energy can be evaluated according to (Piomelli et al. 1988)

$$\Pi_\Delta\left(x,y,z\right) = -\overline{\tau_{ij}\tilde{S}_{ij}} \;, \tag{4.1}$$

where τ_{ij} is the subgrid stresses and $\tilde{S}_{ij} = \frac{1}{2}\left(\frac{\partial \tilde{u}_i}{\partial x_j} + \frac{\partial \tilde{u}_j}{\partial x_i} \right)$ is the filtered/resolved strain-rate tensor. The SGS flux appears as a sink term and a source term in the resolved and unresolved kinetic energy equations, respectively (Meneveau and Katz 2000). It thus quantifies the net energy transfer between resolved and subgrid scales, i.e. the energy transferred across the filter scale Δ.

The calculation of the full SGS flux requires full 3D velocity measurements to include all of the terms involving the vertical velocity, and requires 3D instead of 2D box filtering. For the present 2D measurements, we can only use a 2D surrogate of the SGS flux of kinetic energy (Chen et al. 2006; Carper and Porte-Agel 2008).

In the present study, results will be presented as function of downstream distance, height, and length-scale or wavenumber, k. Significant variations also occur across the wake, in the y-direction. For ease of presentation and interpretation, in this paper we provide results that have been averaged over the y direction. That is to say, we focus on $\langle \Pi_\Delta \rangle_y$. Note that the y-direction averaging is performed on Π_Δ after evaluating it, rather than averaging the velocity gradient and the SGS stress terms separately before computing Π_Δ. Therefore, the results represent spatial averages of an accurately determined quantity over the wake instead of a quantity whose inherent accuracy would be degraded due to spanwise smoothing of its individual factors.

In the spectral domain, Π_Δ can be considered as the net energy transferred across filter wavenumber k_Δ (=2π/Δ), from all smaller wavenumbers to all larger wavenumbers.

Hence, the spectral energy flux $\Pi(k_\Delta)$ can be identified with the mean SGS flux, i.e. $\Pi(k_\Delta) = \Pi_\Delta$. As an example, the measured SGS fluxes at elevation $z/H = 0.50$ are shown as a function of the filter wavenumber in Fig. 4.4a. The different symbols represent fluxes at different streamwise locations, from $x/H = 1.75$ to 2.06. In this figure, Π_Δ is evaluated in the physical space at some particular filter scale Δ, and the result is then plotted as function of k_Δ and interpreted as the spectral energy flux $\Pi(k)$. As shown in Fig. 4.4a, the flux gradually decreases as x increases. This trend is a direct result of the overall decay of the turbulent kinetic energy in the wake.

To cast these trends in dimensionless fashion, we need a characteristic velocity and length scale, since Π has units of V^3/L. We use the spanwise-averaged streamwise velocity fluctuation r.m.s. $\langle \overline{u'^2} \rangle^{1/2}$ as a velocity scale. As a length-scale, the measured mixing length L_m discussed in the previous section provides a possible option to test. Both measured velocity and length-scales are functions of x and z. The normalized energy flux, $\Pi^* = \Pi / (\langle \overline{u'^2} \rangle^{3/2} / L_m)$, plotted against the normalized wavenumber k/k_{L_m}, is shown in Fig. 4.4b. Different lines collapse into a single curve quite well. As the wavenumber increases or the scale decreases, the flux displays a flat region. This plateau starts approximately when the scale becomes smaller than the measured mixing length. In the classic Richardson-Kolmogorov cascade, in the inertial range, the energy flux across different scales displays a characteristic constant value. Accordingly, the mixing length studied here can be considered as a representative of the energy injection range of scales. At scales larger than the mixing length, energy is injected gradually and the flux increases with wavenumber. And at scales smaller than the mixing length, the energy injection becomes small and the flux approaches a constant value, denoted as $\Pi_f^*\left(\frac{z}{H}\right)$. To visualize the deviations from the ideal inertial range behavior, we plot the difference between the normalized flux, Π^*, and the plateau value Π_f^*. Figure 4.4c shows $\Pi^* - \Pi_f^*$ as a function of normalized wavenumber. Later on we will focus on the gradient of $\Pi(k)$ and therefore we do not loose relevant information by subtracting a k-independent constant from the measurements. Data at all five elevations are included, and each elevation includes data at seven streamwise locations. In total, this plot contains energy fluxes at thirty five different locations in the flow. All profiles tend to show very similar trends with a constant value when the normalized wavenumber is larger than one. The collapse indicates that the energy flux in the whole field of the near-wake of the tree can be quantified by the mixing length, which itself encodes the multi-scale geometry of the fractal object.

4.2 Spectral gradient of kinetic energy flux

Next, we consider the wavenumber space gradient of the energy flux, which at large scales can be considered as an indication of the net injection rate of kinetic energy into the cascade. For steady state turbulence at sufficiently low wavenumbers (where viscous terms can be neglected), Eq. 1.1 reduces to

$$P(k) = \frac{d\Pi(k)}{dk}. \qquad (4.2)$$

As discussed when introducing Eq.1.1, for inhomogeneous flows, such as in our experiment, $P(k)$ contains shear production as well as spatial (mainly vertical) transport of kinetic energy. By measuring $d\Pi(k)/dk$ from the data, we are evaluating the combined net injection rate, without separating the production and spatial transport. Numerically, we obtain $d\Pi(k)/dk$ using finite differencing of the measured SGS flux. We use centered finite difference derivatives evaluated both at $(k^{j+1}+k^{j})/2$ and at $(k^{j+1}+k^{j-1})/2$, where k^{j} are the wavenumbers at which flux measurements are performed. Results from both methods of evaluation are plotted together, providing an increased number of points, since the wavenumbers are not equidistant.

The flux gradient or net injection rate evaluated in this fashion is shown in Fig. 4.5a, where colors and symbols indicate different elevations and streamwise locations, as before. Generally, as the wavenumber increases or the scale decreases, the net injection rate decreases, as energy is mostly injected at large scales. However, it can be discerned that the net injection rate approaches zero more abruptly at the lower elevations than at higher elevations. For example at z/H = 0.97, the flux is close to zero only for $k > 1450\, rad\, m^{-1}$, whereas for z/H = 0.50, it reaches zero at much lower wavenumbers, close to $k > 400\, rad\, m^{-1}$. Also, for scales in the inertial range, the effects of dissipation are negligible as assumed when stating Eq. 4.2. To test this notion based on the data, in Fig. 4.5a we plot the transverse viscous dissipation spectrum $2\nu k^{2} E_{11}(k)$ using data at $z/H = 0.92$, as in Fig. 4.3. As can be seen, over almost the entire relevant range of wavenumbers where net injection takes place, viscous contributions are negligible.

Figure 4.5b shows the injection rate with the horizontal-axis normalized using the measured mixing length at each location and with vertical-axis normalized using $\langle \overline{u'^{2}} \rangle^{3/2}$. The collapse of the curves corresponding to the lowest four elevations is quite good but the data at the fifth generation deviates from the collapsed curve. Interestingly, data at all elevations show a power law behavior with slope $-7/3$ which is evident in Fig. 4.5c.

As demonstrated in Fig. 4.5d, we have found that a better collapse can be achieved when we use a fixed velocity scale, such as U_H, instead of the position-dependent r.m.s. velocity. By using U_H, the points that are scattered in Fig. 4.5a collapse quite well in Fig. 4.5d and decay together as a function of normalized wavenumber. Figure 4.5e shows the results in a log-log plot, together with a suggested $k^{-7/3}$ power law behavior. A power-law decay of the production spectrum in the inertial range of turbulence in shear flows has been introduced before based on dimensional analysis and heuristic arguments as follows (Tennekes and Lumley 1972; Driscoll and Kennedy 1981). The shear production, $P_s(k)$, is the work per unit time done by the mean strain rate, S, on eddies at scale k. Dimensionally, it is energy-density per unit wavenumber, per unit time. Thus, using $E(k)$ for energy density, and $1/S$ as characteristic time-scale for the mean strain, $P_s(k)$ can be assumed to be proportional to $E(k)S$. However, shear production is mediated by the shear stresses and thus depends upon the degree of anisotropy at each scale. Inherently, $P_s(k)$ vanishes for isotropic turbulence (and equals the net injection $P(k)$ for homogeneous turbulence). A heuristic model for the degree of anisotropy, denoted as a factor $\gamma(k)$, is the ratio of mean to turbulent strain-rate, $S/s(k)$, where $s(k)$ is the characteristic strain rate of eddies of scale k^{-1}. Thus, it is assumed that $P_s(k) \sim \gamma(k) S E(k)$. When the size of eddies is much smaller than the mean flow scales or the motions of such eddies are much faster than that of the mean flow, the value of γ diminishes, indicating weaker energy production. On the other hand, at large scales or eddy motions are slow, one obtains large values of γ resulting in large energy production. In terms of the energy spectrum, one can write $S(k)\sim[k^3E(k)]^{1/2}$ and thus $\gamma(k)=S[k^3E(k)]^{-1/2}$. Finally, the production spectrum is $P_s(k)\sim S^2k^{-3/2}E(k)^{1/2}$. In the range where $E(k)\sim k^{-5/3}$, one obtains $P_s(k)\sim k^{-7/3}$. We recall that in our data, the net injection is likely to be affected by spatial transport. The wavenumber scaling of this effect is unknown and so is not possible to determine whether spatial transport causes deviations from the observed $P_s(k)\sim k^{-7/3}$ scaling or whether it reinforces it.

In the log-log plot of the net injection spectrum shown in Figure 4.5e it can be seen that at high elevations, for planes corresponding to the fourth and fifth branch generations, there is a small bump in the net injection rate at normalized wavenumber between 0.8 and 1.5. In vegetation canopy turbulence, researchers have proposed a mechanism of energy cascade bypass (Finnigan 2000; de Langre 2008; Cava and Katul 2008; King et al. 2012), leading to a spectrum that deviates from the Kolmogorov spectrum at small scales, specifically showing larger energies at high wavenumbers. From Fig. 4.3, it can indeed be seen that the spectrum for high elevation, $z/H = 0.92$, displays a flatter slope compared to $k^{-5/3}$, leading to somewhat higher $E(k)$ at high wavenumbers ($k_2=10^3$ $rad\ m^{-1}$). Since in the proposed scaling analysis the production spectrum is proportional to $E(k)^{1/2}$, it would also imply larger $P(k)$ in that range, consistent with the trends displayed in Fig. 4.5e. However, the considerable scatter in the data should be kept in mind when interpreting the results.

So far, we have used the measured mixing length to scale the results in Figs 4.5b-e. But often, one would like to be able to use a predictive model rather than measured length scales. Next, we use the model, Eq. 3.19, to make the wavenumber dimensionless for plotting the injection rate. In Fig. 4.5f, the horizontal axis is the wavenumber normalized by the modeled mixing length. As can be seen, the modeled mixing length can also collapse data at various locations in the flows successfully.

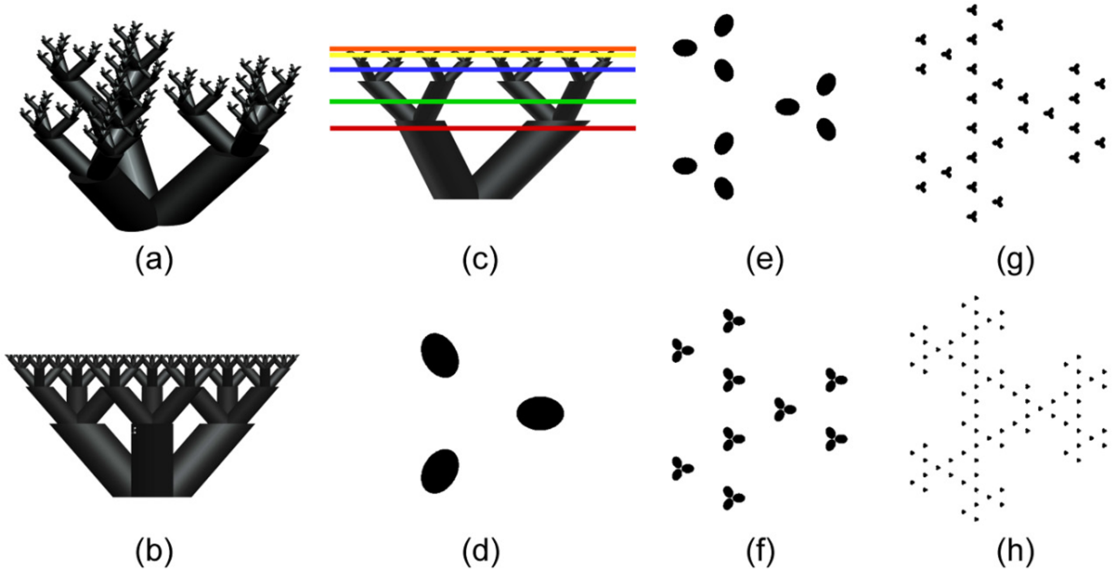

Figure 4.1 The fractal tree model and its typical cross-sections: (a) perspective view; (b) side view; and (c) frontal view. Cross-sections of layers, as indicated in (c), at: (d) $z/H = 0.50$; (e) $z/H = 0.70$; (f) $z/H = 0.86$; (g) $z/H = 0.92$; and (h) $z/H = 0.97$.

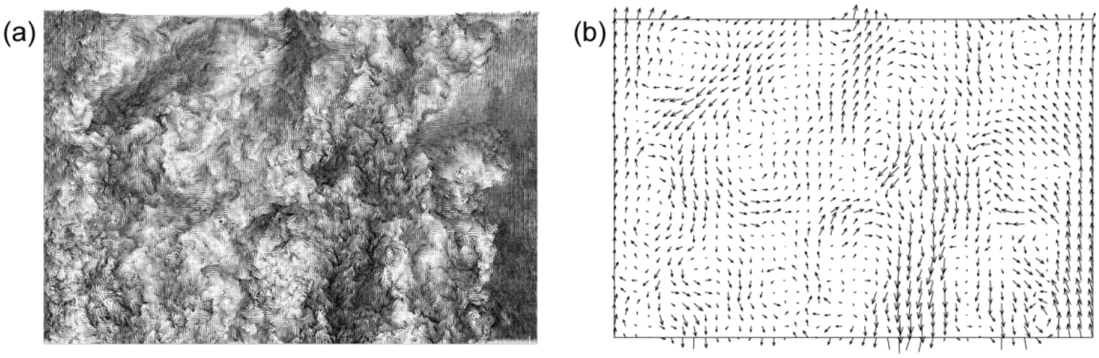

Figure 4.2 (a) An instantaneous velocity vector map, and (b) the filtered vector map of the same velocity field using a filter size of $\Delta = 6\delta$.

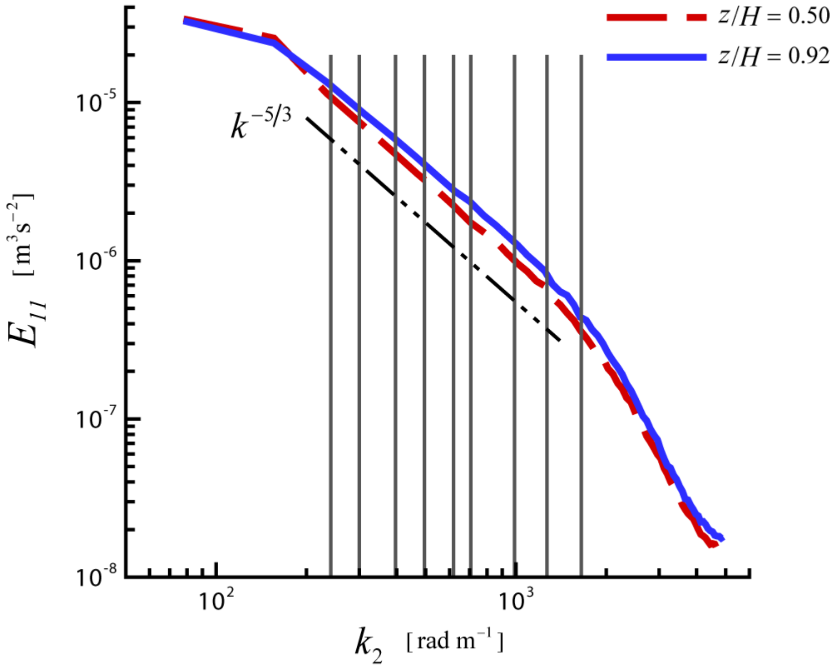

Figure 4.3 Examples of transverse energy spectrum and wavenumbers of filters utilized. Vertical lines from left to right indicate filter wavenumber $k_\Delta = 2\pi/\Delta$, corresponding to $\Delta/\delta =$ 6, 8, 10, 12, 16, 20, 24, 32, and 40.

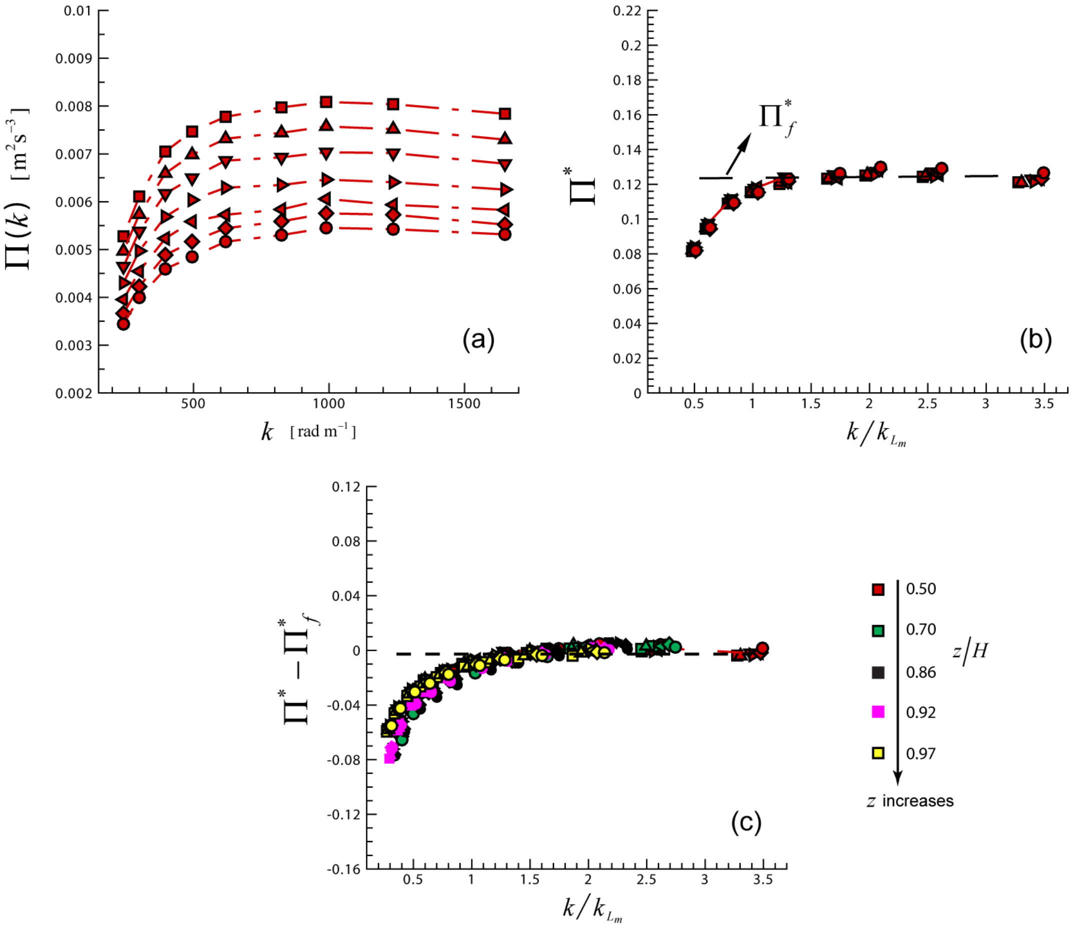

Figure 4.4 (a) Measured SGS fluxes at $z/H = 0.50$ as a function of wavenumber; (b) normalized SGS fluxes $\Pi^* = \Pi/(\langle \overline{u'^2} \rangle^{3/2}/L_m)$ as a function of normalized wavenumber for $z/H = 0.50$. The constant flux in the inertial range is denoted as Π^*_f. (c) Difference between normalized flux and Π^*_f at five elevations. Different symbols represent different streamwise locations: □, Δ, ∇, ▷, ◁, ◊ and ○ indicate $x/H = 1.75$, 1.80, 1.85, 1.90, 1.96, 2.01 and 2.06, respectively. Colors represent different elevations as indicated in the figure.

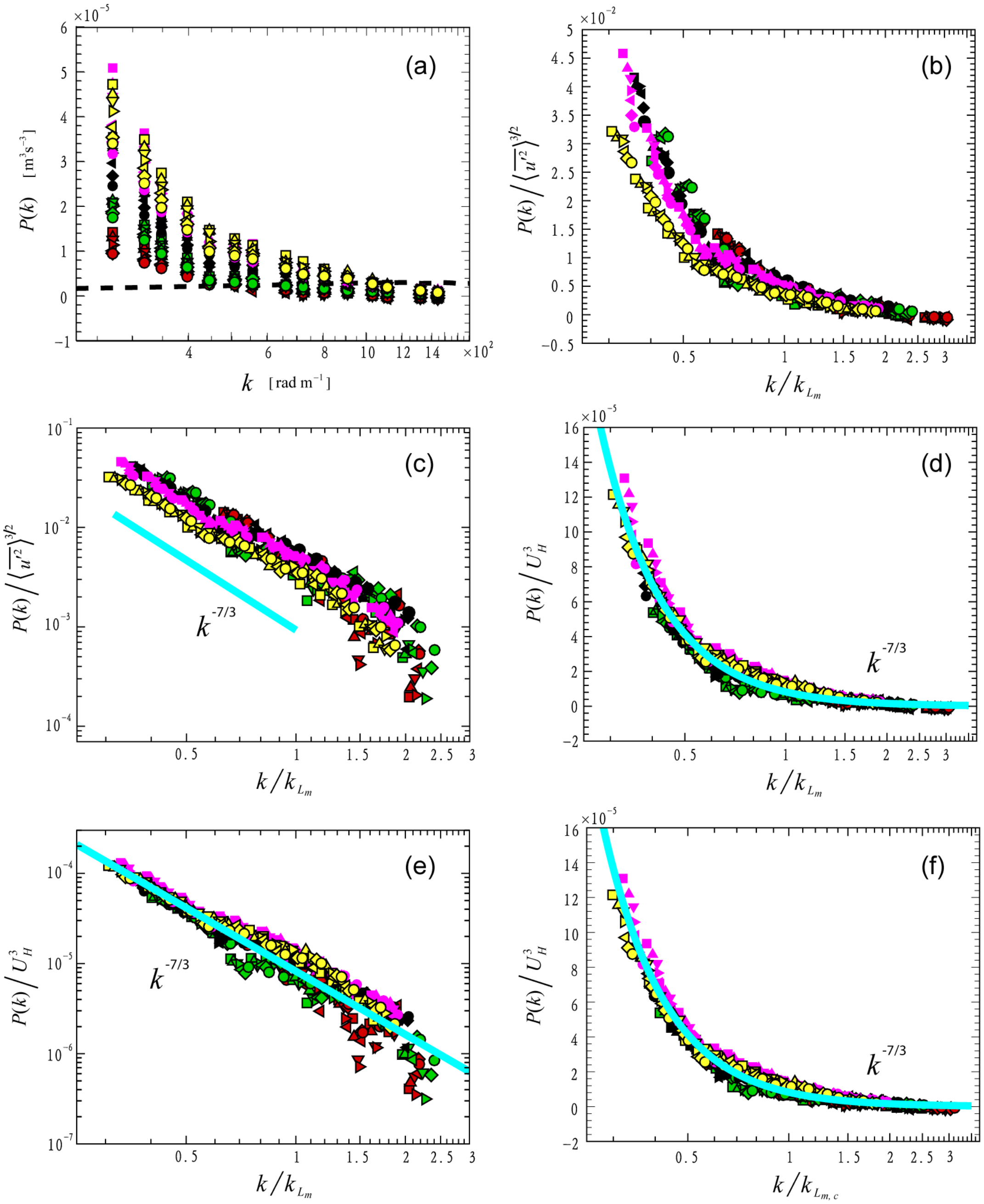

Figure 4.5 (a) Measured flux gradient or net injection rate as a function of k. Also shown (dashed line) is the dissipation spectrum $2\nu k^2 E_{11}(k)$ at $z/H = 0.92$. The data in (a) can be collapsed by the measured mixing length to scale wavenumber and $\langle \overline{u'^2} \rangle^{3/2}$ for velocity. Results are shown in (b) in semilog form, and in (c) as a log-log plot. The solid line shows a $\sim k^{-7/3}$ power-law (see text). A better collapse can be achieved by using a fixed velocity as a velocity scale as shown in (d) in semilog scale, and in (e) as a log-log plot. (f): Use of the modeled mixing length (see Eq. 3.19), instead of the measured one. Legend is the same as in figure 4.4.

Chapter 5. Turbulent Flows inside Entire Canopy with Multiple Tree-like Fractal Objects

In Chapter 3 and 4, we show that the multi-scale branch elements of a single tree appreciably modify the momentum transfer and energy cascade in the turbulence behind it. By using tools from fractal geometry, we could connect the distribution of scales in the tree to the turbulence flow length-scale that enabled them to collapse measurements of the momentum transfer (the mixing length) and the energy cascade rate quite well. The question remains whether such correlations can successfully represent mixing lengths and momentum transfer also inside an entire canopy of such fractal trees rather than only within a single wake. Most previous studies that use models with tree-like shapes focus on the flows above the canopy (e.g. Marshall et al. 2002) or behind the canopy such as wind break (e.g. Schwartz et al. 1995). An entire wake of fractal trees was recently considered in a Large Eddy Simulation study (Graham and Meneveau 2012). But the focus of that study was on how to parameterize the drag effects of small-scale, unresolved branch elements whereas the scaling of the flow response was not studied in detail. Overall, detailed measurements inside canopies of tree-like fractal elements are still lacking.

In this chapter, we perform index-matching PIV measurements to focus on the horizontal distributions of flow quantities such as mean velocities, Reynolds stresses, and dispersive fluxes within the fractal canopy. An important goal of the data analysis is to quantify the level of spatial variations of mean velocity distributions and quantify the relative importance of dispersive fluxes. Horizontal momentum transport is furthermore studied through the eddy-viscosity formalism, where the eddy viscosity and mixing length can be deduced from the experimental results. We then compare the measured mixing length with the model proposed in Chapter 3.

We first describe the experimental setup in section 5.1. In section 5.2, we briefly review the analysis framework used in present study. Results are presented in sections 5.3 to 5.6 where detailed profiles of mean velocity, Reynolds stresses and dispersive fluxes are provided. Also presented are a quantification of the relative importance of dispersive fluxes, and the distribution of mixing length in the context of the eddy-viscosity model.

5.1 Experimental set-up

The fractal canopy model consists of twelve trees arranged in a staggered pattern as presented in Fig. 2.5. A sketch of present study is shown in Fig. 5.1. The target tree is located at the center of the third row where the flow measurements are carried out within a representative flow volume.

The distribution of branches is very dense especially at high elevations. The leaf area density, *a*, is defined as the projected frontal area per unit volume in this present case. The leaf area density profile and the distribution of branch diameters are shown in Fig. 5.2. The diameter of individual branches decreases with elevation, while the leaf area density increases significantly from low to high elevation.

Flow fields are captured by planar PIV. To enhance particles from the background, we account for intensity variations at every single point from one image to another. A threshold is set to separate pixels with high and low image intensity. We keep those with high intensity as representative particles, and set others to zero as the background.

Repeating this procedure for every pixel, good particle images can be obtained efficiently. Velocity vectors are calculated from such thresholded images by the multi-path cross-correlation algorithm using LaVision DaVis software. PIV measurements are carried out both inside and above the canopy on horizontal *x-y* planes, at 22 separate elevations from *z/H* = 0.3 to 1.5. The vector interrogation window size is 64×64 pixels, with 75% overlap. The resolved field of view of about 194×130 mm^2 contains 304×203 vectors, with vector spacing 0.64 mm. The red box in Fig. 5.1 indicates the field of view in the horizontal measurement planes. Elements in this figure are correctly scaled and positioned to easily compare the field of view and the scale of the trees. For every PIV sampling plane, 2000 statistically independent vector maps are obtained to ensure good convergence of turbulence statistics.

5.2 Data analysis framework: ensemble and horizontal averaging

To document the spatial distribution of the flow inside and above the fractal canopy, quantities obtained from both ensemble and horizontal (or double) averaging are computed and presented. Based on ensemble averaging (or time averaging), one can decompose instantaneous velocities into ensemble mean and fluctuating parts as usual:

$$u_i = \overline{u}_i + u_i' = U_i + u_i' , \tag{5.1}$$

where the overbar indicates the ensemble averaging (capital letters will sometimes also be used for mean values). Associated with this conventional Reynolds-averaged decomposition, the stress tensor appearing in the mean momentum equation reads

$$\tau_{ij} = -\overline{u_i' u_j'} + \nu \left(\frac{\partial \overline{u}_i}{\partial x_j} + \frac{\partial \overline{u}_j}{\partial x_i} \right) = \left(\nu_t + \nu \right) \left(\frac{\partial \overline{u}_i}{\partial x_j} + \frac{\partial \overline{u}_j}{\partial x_i} \right) , \tag{5.2}$$

where $\overline{u_i'u_j'}$ are the Reynolds stresses which represent momentum fluxes due to turbulent motion. As a closure, the deviatoric part of the Reynolds stress tensor is usually modeled using an eddy viscosity as described in Eq. 3.1, leading to the second equality in Eq. 5.2.

In studies of urban and vegetation canopy flows with complex spatial structures, it is usually a difficult and daunting task to resolve every single element and formulate it as a boundary condition. Instead, additional spatial averaging over the volume containing canopy elements is often performed. This spatial averaging procedure was introduced for canopy flows by Wilson and Shaw (1977) and further developed by Raupach and Shaw (1982). The averaging is applied over a horizontal plane, while a more general volume averaging was then introduced by Finnigan (1985) and Raupach et al. (1986). In the present study, averaging in the horizontal planes, i.e. *x-y* planes, is applied in addition to ensemble averaging. The spatial averaging only applies to fluid regions, namely the intrinsic values are obtained. After the double averaging, the velocity u_i can be decomposed as

$$u_i = \langle \overline{u}_i \rangle + \overline{u}_i'' + u_i' , \tag{5.3}$$

where $\langle \overline{u}_i \rangle$ indicates the planar averaged velocity (planar space averaging is denoted by angular brackets) and $\overline{u}_i''$ is the deviation of the local mean velocity from the spatial mean. The spatial averaging only applies to fluid-phase regions, excluding trees. In this formulation, the stress tensor in the double-averaged momentum equation becomes as

$$\tau_{ij} = -\langle \overline{u_i'u_j'} \rangle - \langle \overline{u}_i''\overline{u}_j'' \rangle + \nu \left(\frac{\partial \langle \overline{u}_i \rangle}{\partial x_j} + \frac{\partial \langle \overline{u}_j \rangle}{\partial x_i} \right) . \tag{5.4}$$

Besides the conventional Reynolds and viscous stresses, the so-called dispersive fluxes $\left\langle \overline{u}_i''\overline{u}_j'' \right\rangle$, appear in the double-averaged momentum equation. In following sections, flow variables arising from these two averaging methods will be discussed in detail.

5.3 Flow variations inside the canopy: a view from contour plots

In Fig. 5.3, a sample instantaneous vector map is shown on a horizontal *x-y* plane at elevation *z/H* = 0.85. For clarity, only half of the vectors are shown and the ensemble mean streamwise velocity has been subtracted. The color contours indicate streamwise velocity magnitude. This cross-section is located at the third generation of the tree. Keeping in mind that there still are two generations of branches above this elevation, data acquisition has taken place through the canopy from the top this revealing the flow field inside the canopy. The wakes behind each individual branch can be identified, as well as their decay and interactions. The tree structures produce high and low velocity regions, which result in strong variations of the flow field thus justifying the need for PIV measurements. Relying on a small number of sampling points would have failed to capture such complicated flow structures.

For efficient presentation of the results recorded at 22 different elevations, we combine these data. The acquired horizontal PIV sampling planes are sufficiently close to each other (with typical distance of about 5 mm) to allow a smooth interpolation of the statistical fields. As a result, a three-dimensional volumetric dataset can be generated. The inverse-distance interpolation is applied but only for plotting and visualization purposes. All the quantitative analyses of results are based on actual acquired data. The ensemble mean streamwise velocity contours in *y-z* planes are shown at three streamwise locations in Fig. 5.4a where the contours indicate velocity magnitude and the black region indicates the tree branches. The velocity is normalized by the double-averaged mean streamwise velocity at $z/H = 1.5$, which is $U_c = 0.7$ m/s. In Fig. 5.4a we observe that trees generate wakes that reflect the general tree shape. For example at $y/H < 0$, the wake shown at $x/H = -0.5$ comes toward the branch located at $x/H = 0$. After passing through this branch, wake regions with low velocity follow the shape of the branch and a wider region of low velocity is seen to occur at low elevations, $z/H < 0.5$. Similar trends can be observed on the other side at $y/H > 0$, where the wake signatures can be clearly observed for example at $x/H = 0$. At increasing elevation, the wake region starts branching out similarly to the tree branches. The strong flow heterogeneity with branches providing sheltering while sparse regions without branch blockage show higher velocities (for example at center region where $y/H = 0$ and $z/H = 0.6$) has motivated other researchers (Bohm et al, 2013) to consider partitioning of the flow into wake and non-wake regions. At the same time, the recovery rates of the wakes varies at different locations due to differing distances to the branches, which also contributes to the variety of velocity distribution patterns. Above the canopy one can also observe low and high velocity regions extending to different elevations depending on the local topology of the tree underneath.

Based on above observations, dispersive fluxes are expected to be relatively important. As an example, the variable contributing to the streamwise component of the dispersive flux, $\overline{u}''\overline{u}''$, is shown in Fig. 5.4b. Note that what is shown is not the dispersive flux. The latter is $\overline{u}''\overline{u}''$ after horizontally averaging. Large magnitudes of $\overline{u}''\overline{u}''$ can be seen in the wake regions due to the significant velocity defects there. For similar reasons, regions with locally high flow velocity also have a large contribution to the dispersive flux, as seen for example at $y/H = 0$ and $z/H = 0.6$. At higher elevations above the canopy, flow variations gradually diminish, and so do the dispersive fluxes. For example at $z/h = 1.3$, $\overline{u''u''}$ nearly vanishes which indicates that the ensemble-averaged velocity becomes spatially uniform on horizontal planes.

From the horizontal measurement, we can evaluate three components of the full Reynolds-stress tensor, i.e. $\overline{u'u'}$, $\overline{v'v'}$, and $\overline{u'v'}$. The distributions of $\overline{u'u'}$ and $\overline{u'v'}$ are shown in Figs. 5.4c and d while component $\overline{v'v'}$ is not shown since it has a similar pattern as the $\overline{u'u'}$ term only with different (smaller) magnitude. Overall features of the tree shape again can be recognized in these distributions. Of particular interest is the distribution of Reynolds shear stress $\overline{u'v'}$, which quantifies the transverse momentum transport in horizontal planes. As expected from the eddy-viscosity concept, in Fig. 5.4 one can see that $\overline{u'v'}$ appears to be strongly correlated with the transverse gradients of mean streamwise velocity. For instance in Fig. 5.4 one can see that the zero-crossings of $\overline{u'v'}$ occur at positions where the mean velocity gradient vanishes, for example at the wake center at $x/H = 0.5$, $y/H = -0.4$ and $z/H = 0.4$. Around the edges of this wake, for example at $y/H = -0.6$ and 0.2, mean velocity gradients display large magnitude, with negative and positive signs respectively. At similar locations the Reynolds shear stress also displays strong magnitudes, and with opposite signs. Many prior studies have focused on the relation between $\overline{u'w'}$ and $\partial U/\partial z$, of relevance to vertical momentum flux. Of importance for horizontal transport, the relationship between $\overline{u'v'}$ and $\partial U/\partial y$ can be identified qualitatively in the contour plot shown in Fig. 5.4. More quantitative validation of the eddy-viscosity relationships will be presented in section 5.6.

5.4 Mean velocity and stress profiles throughout the canopy

A quantitatively more detailed view of the flow is provided using profiles. For example in Fig. 5.5, ensemble-averaged mean velocities are shown as a function of height at 25 locations. Different plots, from (a) to (e), show results at different streamwise locations, i.e. at *x/H* = -0.53, -0.27, 0, 0.24, and 0.50. In each plot, lines with different symbols indicate velocity at different spanwise locations, i.e. *y/H* = -1.01, -0.54, -0.09, 0.36 and 0.83. As references, the horizontal dashed lines indicate top locations of each generation. Some interesting trends can be observed in the distribution of mean velocity. First, stronger variations are observed in regions occupied by the lowest three generations when compared to relatively higher elevations. Velocities in the lower regions range from -0.1 to 0.7. Just in the lee region of the first generation branch, the mean velocity has negative value as seen in Fig. 5.5d, where sampling points are located in the recirculation zone generated by the big branch. Other locations, which are relatively sparse display large velocity magnitude. Secondly, the rate of streamwise evolution of the velocity strongly depends on location. When trees do not obstruct the flow, for instance at *y/H* = -1.01 and 0.83 (lines with square and diamond symbols), an “S” shape is observed in both profiles at different streamwise locations, where a second velocity maximum appears in the region of the second tree generation inside the canopy. These profiles do not vary much from upstream to downstream locations. They display similar shapes and magnitudes along the streamwise direction. In contrast, the velocity varies strongly at other spanwise locations with tree branches and velocity deficits that are generated accordingly. For example at y/H = -0.54 (lines with circular symbol), when the flow hits the branch at x/H = 0 as in Fig. 5.5c, the lowest five points are inside the branches with zero velocity. In the lee region of this big branch, i.e. in the recirculation zone, the mean velocity shows negative values as in Fig. 5.5d. Further downstream, the velocity recovers some, as in Fig. 5.5e.

The spatial variability of the mean velocity can be quantified through the profiles of dispersive flux component $\overline{u}''\overline{u}''$, shown in Fig. 5.6. This term represents the contributions to the final dispersive flux $\langle \overline{u}''\overline{u}'' \rangle$ which is a double-averaged quantity and only a function of height. The sparse space (lines with diamond symbols) displays relatively higher velocity than other regions blocked by trees leading to significant contributions to the dispersive flux throughout the canopy, especially at high elevations. At lower elevations, the wakes contribute even more to the dispersive flux, for example producing a distinct peak of $\overline{u}''\overline{u}''$ (line with circular symbols in Fig. 5.6d). Further downstream as shown in Fig. 5.6e, $\overline{u}''\overline{u}''$ decreases as wakes recover.

5.5 Spatially averaged quantities

In this section, various spatially averaged profiles are presented. Before performing full plane averaging, profiles based on averaging along individual lines are introduced. Figure 5.7 shows the averaged quantities along the streamwise direction where different lines indicate different spanwise locations. It is interesting that the behaviors can be separated into two regions, consistent with observations by Bohm et al. (2013), namely into wake and non-wake regions. At y/H = -0.54 and 0.36, velocities decrease first and show a large deficit near the top of the first-generation branches due to their wakes. On the other hand, in profiles at y/H = -1.01, -0.09, and 0.83 at locations without tree blockage where the flow can penetrate more easily, velocities display larger magnitude compared to the wake regions. At higher elevations close to the canopy top, small branches are densely distributed and absorb significant amounts of streamwise momentum. Above the canopy, the mean velocity recovers and increases significantly. Overall, these trends depend most strongly on the local blockage distribution of the trees.

Two general patterns can also be observed in the streamwise averaged dispersive flux component $\langle \overline{u}''\overline{u}'' \rangle_x$ profiles, shown in Fig. 5.7b. At y/H = -0.54 and 0.36, $\langle \overline{u}''\overline{u}'' \rangle_x$ peaks around the top of the first branch generation due to the local mean velocity deficits. Most $\langle \overline{u}''\overline{u}'' \rangle_x$ comes from the regions of the first and second generation. It has negligible contributions at higher elevations, i.e. above the second generation. On the other hand, at regions y/H = -1.01, -0.09, and 0.83 where the local mean flow velocity is larger than in the surroundings, there are large contributions to the dispersive flux especially at high elevations. The local velocity deficits in the wake regions contribute significantly to the dispersive fluxes in the lower canopy layer while the non-wake regions with locally high velocity play more important roles in the higher portions of the canopy. As a combined effect, the entire flow field inside the canopy displays large dispersive fluxes.

Next, we present results for double-averaged quantities where the spatial averaging is applied to the flow field in x-y horizontal planes. Figure 5.8a shows the double-averaged horizontal mean velocity components. The mean velocity in the spanwise direction is close to zero. Inside the canopy, the double-averaged streamwise velocity displays a local maximum around the top of the first-generation branches of the trees. Similarly, a local velocity maximum has been observed by Dupont et al. (2012) whose vertical distribution of vegetation is comparable with that in the present experiment in the sense that a dense foliated layer exists around top canopy and below it has a layer with only trunks. Close to the canopy top, i.e. at *z/H* = 0.9, a velocity deficit can be observed including an inflection point. Above this region, the velocity increases significantly. For the double-averaged Reynolds stresses shown in Fig. 5.8b, the $\langle \overline{u'u'} \rangle$ and $\langle \overline{v'v'} \rangle$ components show very similar trends. They are approximately constant inside the canopy and display a peak towards the top of the canopy. Above the canopy, they gradually decrease, until at around *z/H* = 1.5 they almost vanish. One can also note that the $\langle \overline{u'v'} \rangle$ component is close to zero inside the canopy due to the horizontal averaging procedure which averages out $\overline{u'v'}$ with positive and negative signs. In this flow $\overline{u'v'}$ is associated with the wakes generated by the trees inside the canopy. This term becomes apparent simultaneously on both sides of the wake as can be seen clearly in Fig. 5.4c where the magnitude is just slightly smaller than streamwise component $\overline{u'u'}$. However, due to its opposite signs on both sides, the horizontal averaging generates a vanishing $\langle \overline{u'v'} \rangle$.

Figure 5.9 shows two components of dispersive fluxes $\langle \overline{u}''\overline{u}'' \rangle$ and $\langle \overline{v}''\overline{v}'' \rangle$ normalized by the double-averaged Reynolds stresses. The relative spanwise component of dispersive fluxes is small, and gradually decreases inside the canopy and is about zero above the canopy. The streamwise component of dispersive flux $\langle \overline{u}''\overline{u}'' \rangle$, on the other hand, shows a maximum value in the second-generation branch region. Over most of the canopy height, for $z/H < 0.9$, the dispersive flux $\langle \overline{u}''\overline{u}'' \rangle$ exceeds the streamwise Reynolds stress. At $z/H = 0.6$ in the region of the second-generation branches, it reaches up to four times the corresponding Reynolds stress.

5.6 Boussinesq eddy viscosity and Prandtl mixing length

In the Boussinesq eddy viscosity model, the Reynolds shear stress is related to the gradient of the mean velocity as discussed in Eq. 3.1. In studies of canopy flows, among many important roles, eddy viscosity and its associated length scale are key factors in modeling mean velocity profiles, see e.g. the works by Cionco (1965) and Macdonald (2000). However, in most of the canopy turbulence literature the Boussinesq eddy viscosity is assumed directly without questioning the validity of Eq. 3.1, probably due to lack of detailed experimental data covering a sufficiently large dynamic range. The index-matching enables us to measure Reynolds shear stress as well as mean gradients in regions usually blocked by the tree branches that could not be measured in previous experiments. The eddy-viscosity relationship describing momentum transport in the horizontal planes can be written as in Eq. 3.2. Different from the wakes where $\partial V/\partial x$ is usually much smaller than $\partial U/\partial y$, flows inside the canopy may produce relatively large value of $\partial V/\partial x$. Therefore, $\partial V/\partial x$ may not be simply ignored and the relation between $\overline{u'v'}$ and $(\partial U/\partial y+\partial V/\partial x)$ is evaluated. We choose to examine this relation through scatter plots of these two quantities for a variety of spanwise directions, and study how the scatter plot varies at different locations. In Figs. 5.10a and b, two typical scatter plots of Reynolds shear stress $\overline{u'v'}$ and mean velocity gradient $(\partial U/\partial y+\partial V/\partial x)$ are shown at $z/H =$

0.51 and 0.98 respectively. In each figure, different symbols indicate results at different streamwise locations. For each elevation, data at different streamwise locations mostly follow the same trend and a linear behavior can be discerned, although accompanied by significant scatter.

As can be observed, the scatter plot slope changes with height. For instance, a shallower angle is observed near the canopy top at z/H = 0.98 compared to z/H = 0.51. It suggests significant variations of the eddy viscosity as function of elevation. In order to quantify this trend, the slope at different locations is estimated by linear least-square regression. The eddy viscosity measured from the data in this fashion is shown as a function of elevation in Fig. 5.11a. The error bars at each elevation indicates variations of measured eddy viscosity at different streamwise locations. The mean eddy viscosity shows a local peak at the center of the second generation, and reaches its minimum around the top of canopy. Above the canopy, it increases a bit and remains constant at higher elevations. The trend inside the canopy is different from what has been previously reported in canopy flows. For example, Raupach et al. (1986) and Brunet et al. (1994) report increasing trend of eddy viscosity from experiments in stripe canopy models and nylon-stalk canopy models respectively. Constant eddy viscosities have also been reported in some studies using canopy models (Thom 1971; Novak et al. 2000). The difference between our results and others might be due to the multi-scale characteristics of the presently studied canopy elements as well as the focus on horizontal rather than vertical momentum transport.

Associated with the eddy-viscosity model, the Prandtl mixing length, L_m, is expressed based on

$$\nu_t = L_m^2 \left| \frac{\partial U}{\partial y} + \frac{\partial V}{\partial x} \right|, \tag{5.5}$$

by including gradients of both velocity components. Since eddy viscosity is obtained at various streamwise (x) and vertical locations (z) by fitting (averaging) scatter plots of data in the spanwise (y) direction, it is appropriate to average the velocity gradient magnitude in the y direction as well. This approach was also followed in Bai et al. (2012) for measurements in the wake of a single fractal tree. The resulting mixing length is shown in Fig. 5.11b as a function of elevation. The error bars represent the variation of mixing length at different streamwise locations (standard deviation). The mean value of the mixing length indicates the momentum transport at each elevation. Two distinct trends are clearly observed and are separated at the top of trees. Above the canopy, the mean mixing length increases with elevation. As indicated by the straight line in Fig. 5.11b, in fact it follows the classic boundary layer scaling $\kappa(z-d)$ where κ is the von Karman constant (the slope of the plotted line has $\kappa = 0.4$) and d is the displacement height (here we observe $d/H = 0.94$). However, inside the canopy, the observed decreasing trend with height differs from previous studies. For extremely sparse canopy (Belcher et al. 2003), one could expect that the effects from the trees are not relevant, then the Prandtl mixing length follows the classic boundary layer scaling $L_m \sim \kappa z$. For dense canopy, previous studies of vertical transport have found or used either increasing mixing length (Uchijima 1962; Cown 1968) or a constant mixing length (Cionco 1965; Seginer et al. 1976; Belcher et al. 2003, Poggi et al. 2004b).

For modeling purpose, it would be interesting to link the scales in the flows to the morphology of the trees such as the diameters of the branches. Such an idea has been verified in a canopy model with cylinders (e.g. Poggi et al. 2004b). In the present case, the branch diameters, from first generation at bottom to the fifth generation at the top, decreases by a factor of about 8. However, the measured mixing length across the canopy decreases only by a factor of approximately 2, from 8 mm to 4 mm. As a result, this smaller rate of decrease cannot be explained by variations of prevailing branch diameters. Another quantity which is widely used to describe the morphology of the canopy is the leaf area density which is shown in Fig. 5.2 and the inverse of this quantity provides a length scale which might quantify the scales of the tree. As one can expect from Fig. 5.2, the inverse of the leaf area density decreases by a factor of 5 from low to high elevation, and hence fails to capture the measured decreasing trend. In the wake of a single fractal tree, the trend of mixing length is found to be captured by a continuous model as described in Eq. 3.19. In Fig. 5.11b, the modeled mixing length scale based on Eq. 3.19 with pre-factor 0.29 is compared to the measured data inside the canopy. Clearly, the model can capture the decreasing trend quite well. The agreement indicates that to quantify the characteristic length scales of the multi-scale structures and the flow fields generated by them, the multi-scale information should be incorporated. The good agreement, in general, also opens the possibility to link the morphological features of the canopy to the scales in the flow.

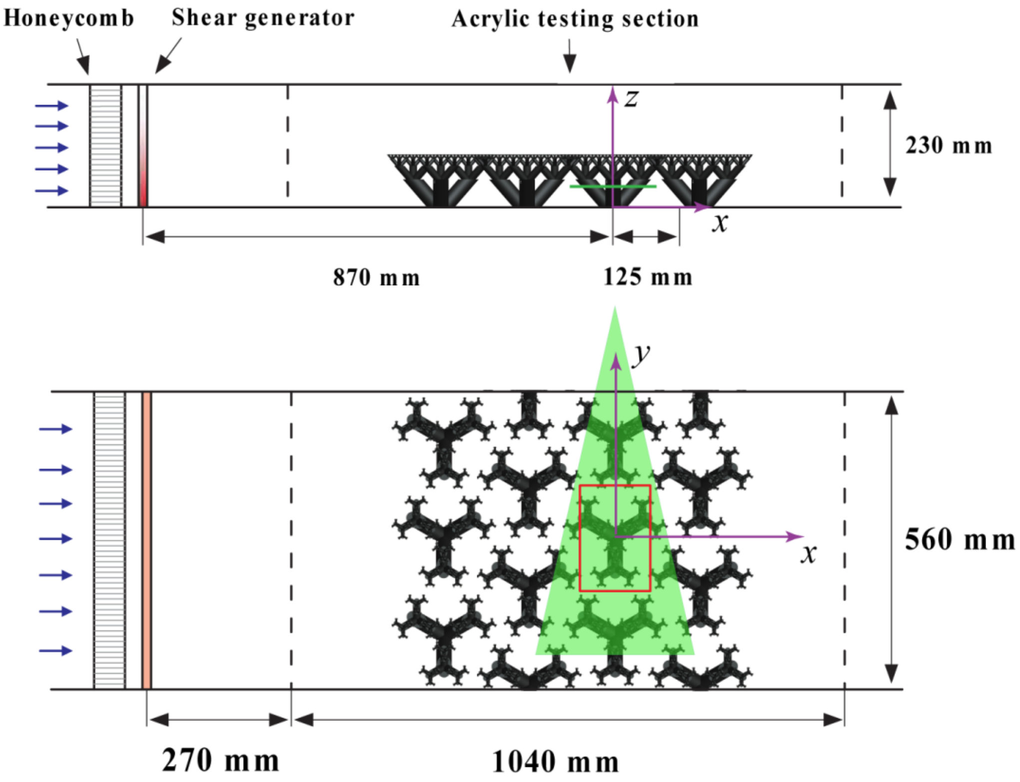

Figure 5.1 Experimental set-up for studies of flow inside the fractal canopy.

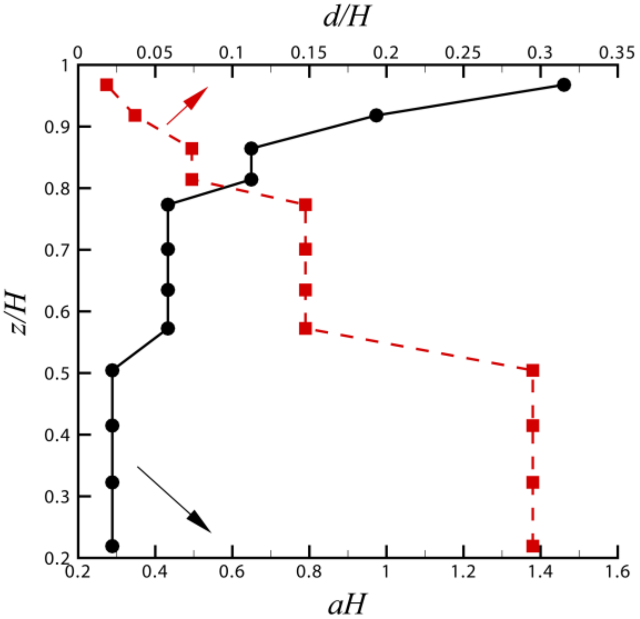

Figure 5.2 Leaf area density of the canopy *a* and branch diameters of the tree *d*.

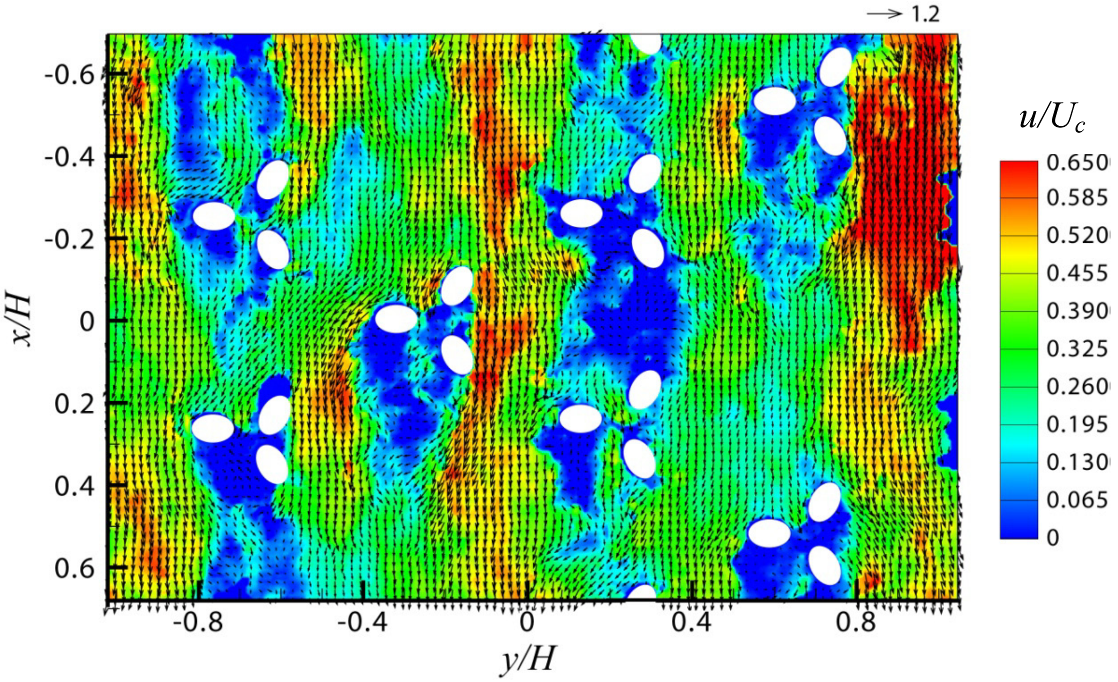

Figure 5.3 Instantaneous velocity field at *z/H* = 0.85, at the third generation of the tree. One third of vectors are shown for clarity. Color contours indicate streamwise velocity magnitude.

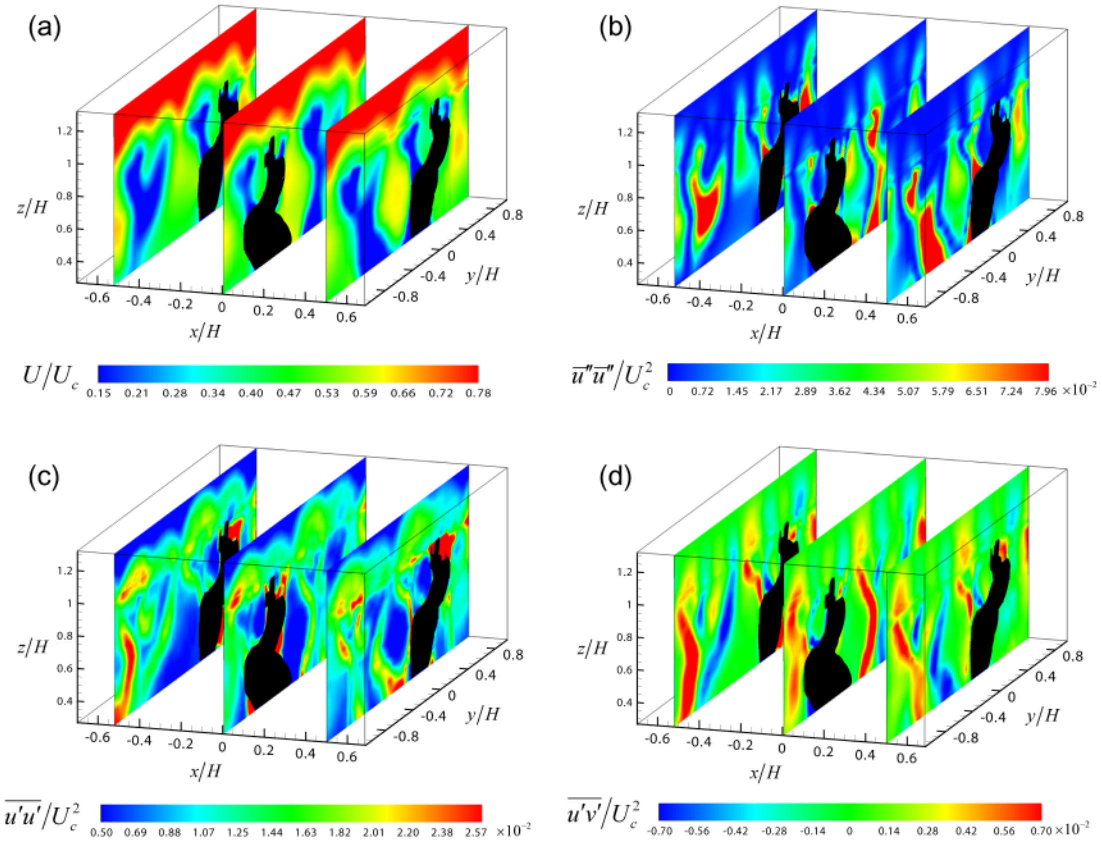

Figure 5.4 Statistics fields inside the canopy: (a) streamwise mean velocity U; (b) streamwise component of the dispersive flux $\overline{u''}\overline{u''}$; (c) Reynolds stress $\overline{u'u'}$; and (d) Reynolds shear stress $\overline{u'v'}$. The black regions indicate tree branches.

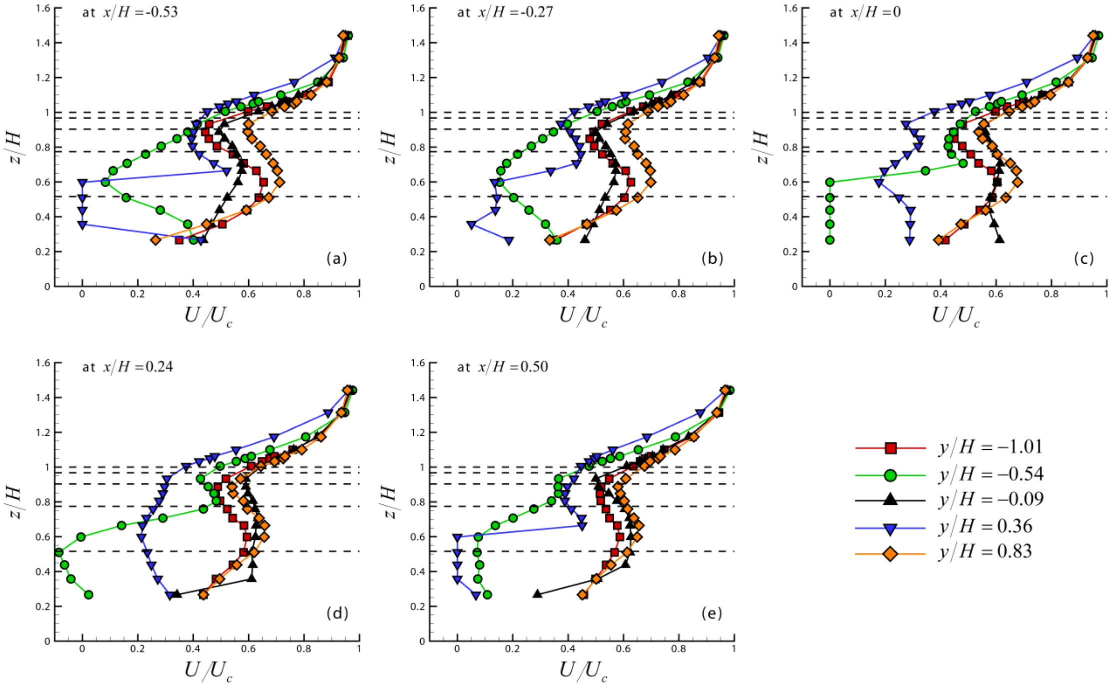

Figure 5.5 Ensemble averaged velocity at various locations. Different plots indicate different streamwise locations. In each plot, different lines indicate different spanwise locations.

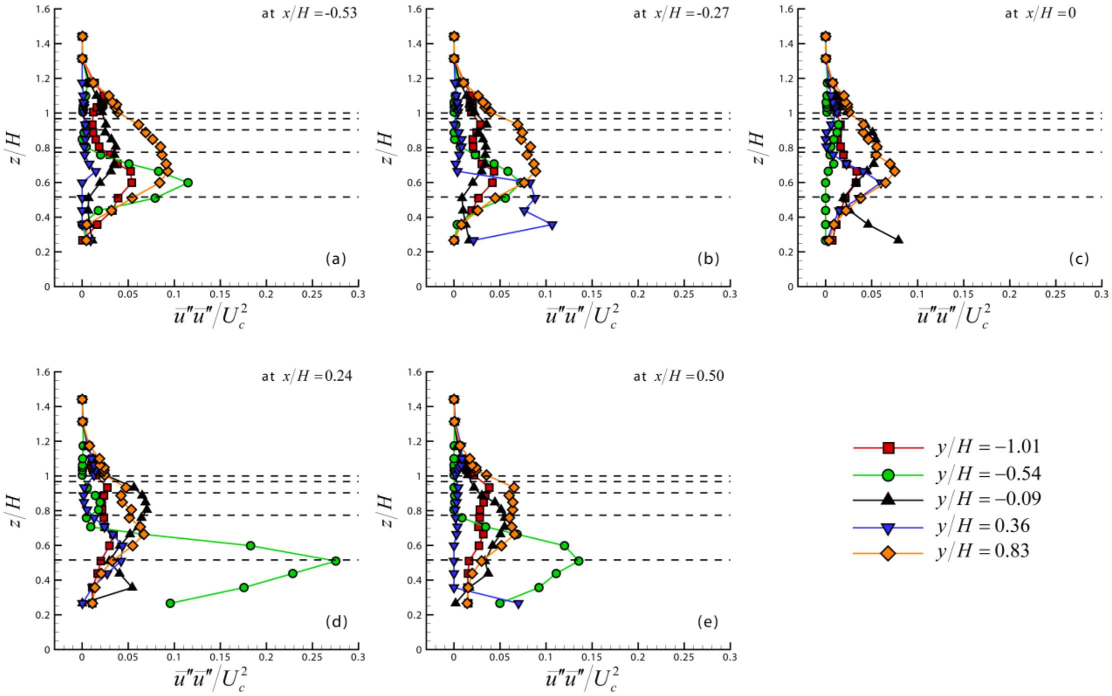

Figure 5.6 Contributor $\overline{u''}\overline{u''}$ of streamwise normal component of the dispersive flux, at various locations.

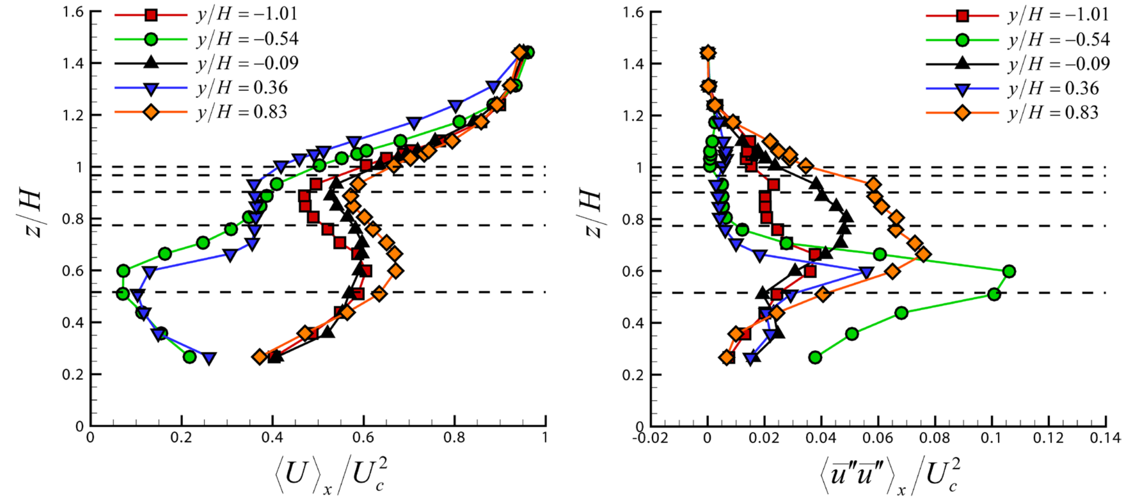

Figure 5.7 Streamwise velocity and component of dispersive flux averaged along the streamwise direction.

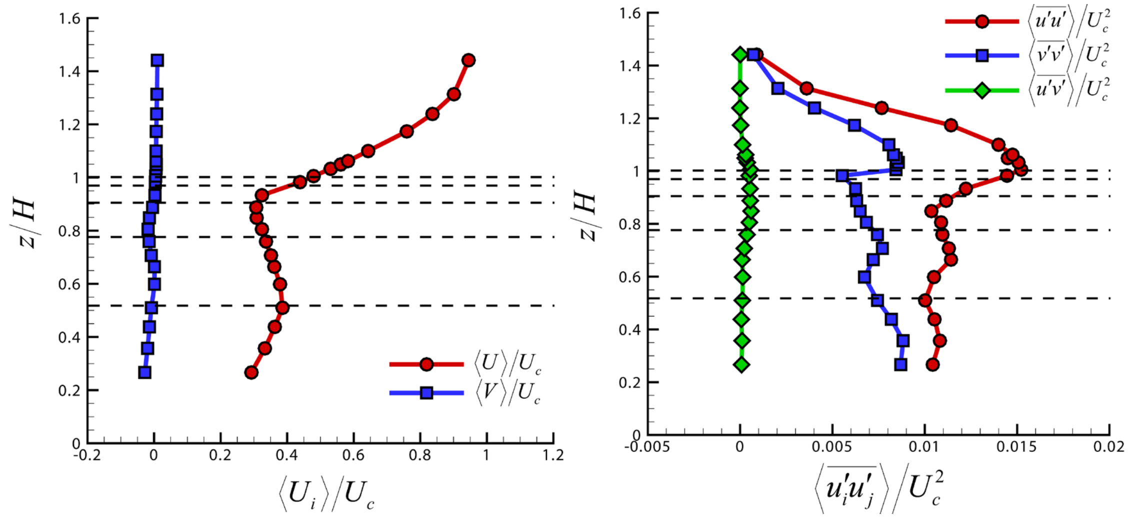

Figure 5.8 Double averaged quantities: (a) mean streamwise and spanwise velocities; and (b) Reynolds stresses.

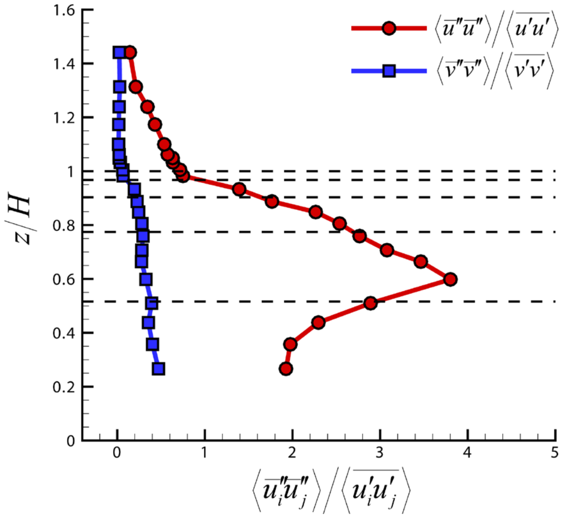

Figure 5.9 Vertical distribution of the ratio of dispersive fluxes to Reynolds stresses.

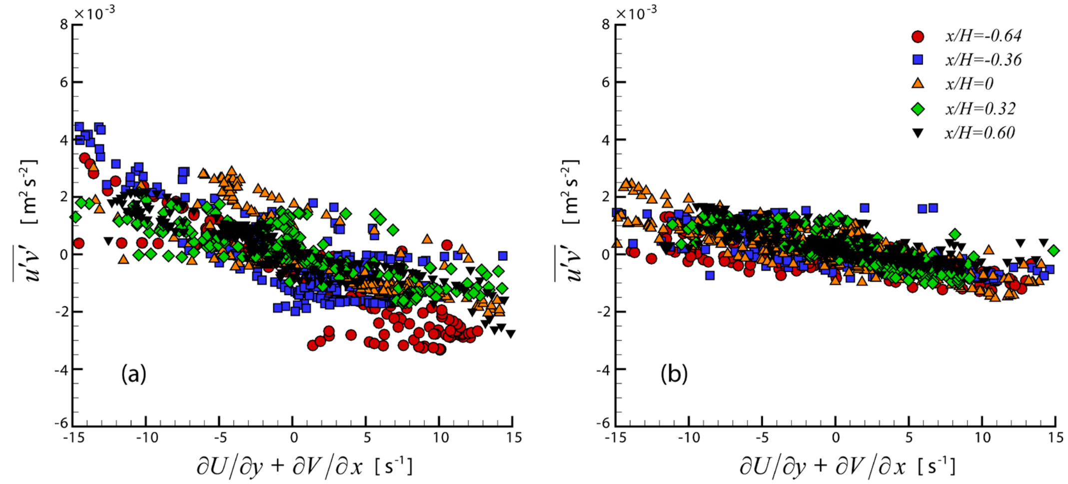

Figure 5.10 Scatter plots of Reynolds shear stress and mean velocity gradient: (a) at *z/H* = 0.51; and (b) *z/H* = 0.98.

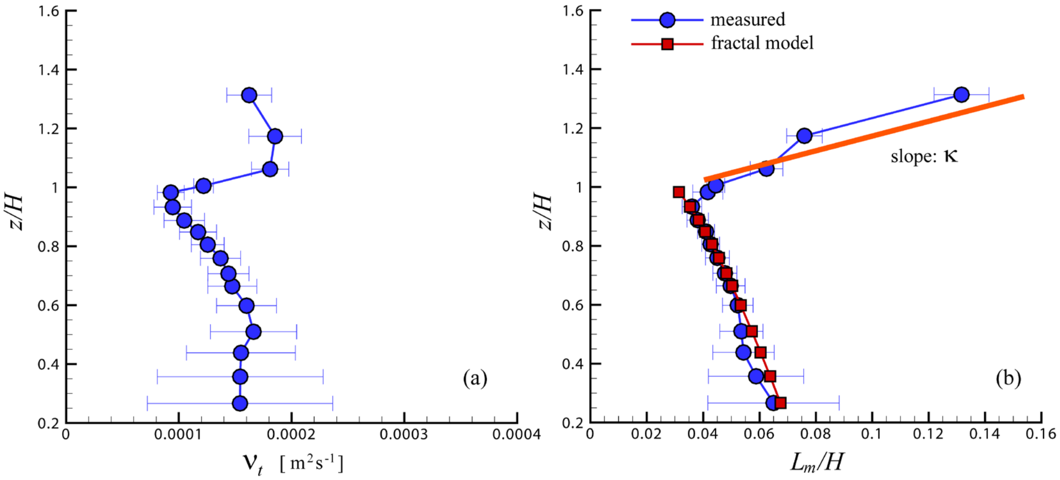

Figure 5.11 (a) Measured eddy viscosity and (b) measured and modeled mixing length. The error bar represents the standard deviation of observed data. A straight line with slope 0.4 is shown as a reference in (b).

Chapter 6. Coherent Flow Structures above the Fractal Canopy

In this chapter, we study the coherent structures above the fractal tree-like canopy. We especially focus on the inclination angle of the coherent structures, as well as on coherent structures at different scales. After a brief description of the set-up in section 6.1, basic profiles of mean velocities and Reynolds stresses above the canopy are presented in section 6.2. The coherent structures are analyzed based on the framework of quadrant analysis in section 6.3. In section 6.4, the inclination angle of the coherent structures are studied in detail, and the coherent structures at small scales are presented in section 6.5.

6.1 Experimental set-up

The flow motions in the vertical planes are captured by PIV where a sketch of the set-up is shown in Fig. 6.1. The measurements are carried out at 18 spanwise locations, from y/H=-1.07 to 0.87, as indicated by the lines in the top view of the target tree in Fig. 6.1c. For vector calculations, the final interrogation window size is 32×32 pixels, with 50% overlap. It provides a vector resolution of about 0.64 mm which is smaller than the smallest branch diameter. For each plane, 2000 statistically independent image pairs are recorded with a sampling frequency of 1 Hz, to ensure good convergence of turbulence statistics.

6.2 Mean velocities and Reynolds stresses

The mean velocities and Reynolds stresses at *y/H*=0.18 and -0.16 are shown in Fig. 6.2 where the solid symbols indicate the mean values of quantities along the streamwise direction, i.e. they are results from averaging along the *x*-direction. The dashed lines indicate the variation of these quantities along streamwise direction. The small variation of flow quantities along the streamwise direction indicates a well developed flow field. Results shown at these two locations represent the typical behaviors at all recorded spanwise locations. One location, i.e. at *y/H*=0.18, has dense branch elements underneath, while the branch elements are distributed more sparsely at the other location, i.e. at *y/H*=-0.16. The mean vertical velocity component *W*, at locations close to the canopy, is slightly larger than zero at *y/H*=0.18 and smaller than zero at *y/H*=-0.16. It remains near zero in regions away from the canopy. The streamwise velocity *U* increases with height and then remains constant beyond a certain elevation. This velocity is denoted as U_∞ (=0.63 m/s). The location of this transition varies at different sampling planes. For example it is located at *z/H*=1.45 and *y/H*=0.18, higher than that at *z/H*=1.35 and *y/H*=-0.16 as in Fig. 6.2a. Such transitions can also be observed in the profiles of Reynolds stresses in Figs. 6.2b and 2c. Below a certain elevation, turbulent motions are quite vigorous as indicated by large magnitude of the Reynolds stresses. Beyond that, on the other hand, Reynolds stresses remain very small. These transition points in both mean velocity and Reynolds stresses coincide, and are considered as indications of the boundary layer thickness in the present study.

Moreover, different behaviors at different spanwise locations can also be observed from the Reynolds stresses in regions close to the canopy top. At *y/H*=0.18, Reynolds stresses first increase with height, reach their maximum at *z/H*=1.15, and then decrease as height increases further. However at *y/H*=-0.16, Reynolds stresses decrease monotonically. The profiles of mean velocity and Reynolds stresses at *y/H*=-0.16 have similar trends as the top part of the profiles at *y/H*=0.18. One should note that the branches of trees at *y/H*=-0.16 are much sparser than at *y/H*=0.18. The flows above the canopy may penetrate the vegetation easier or the displacement height is lower. As a result, the entirety of turbulent structures at *y/H*=-0.16 shift to a lower elevation inside the canopy than at the other locations, and only the decreasing part of Reynolds stresses is observed above the canopy.

6.3 Coherent structures based on quadrant analysis

To further evaluate the contributions to momentum transport from different flow events, we apply the quadrant analysis has been widely used in wall-bounded turbulence (Wallace et al. 1972; Lu and Willmart 1973) and in canopy turbulence (e.g., Finnigan 1979; Shaw et al. 1983; Raupach et al. 1986; Katul et al. 1997; Zhu et al. 2007). It decomposes the flow events into four quadrants based on the signs of fluctuation velocities u' and w'. A quadrant 2 event where $u'<0$ and $w'>0$ is referred to as ejection. It represents low speed fluid moving away from the wall. On the other hand, quadrant 4 event where $u'> 0$ and $w'< 0$is referred to as sweeping motion. It indicates fluid moving towards the wall with high horizontal velocity. The other two events are generally called inward (quadrant 3, with $u'< 0$ and $w'< 0$) and outward (quadrant 1, with $u'> 0$ and $w'> 0$) events. In canopy flows and rough-wall turbulence, the ejection and sweep are the main contributors to vertical momentum transport. Close to rough surfaces, the sweep has the largest contributions to the total shear stress. The importance of sweeps increases with both roughness size and proximity to the surface (Rapauch et al. 1981). These results are in contrast with to those obtained in smooth-wall boundary layers where ejection events are the major contributor to the shear stress, even near the wall.

In quadrant analysis, we define the contribution to total stress from different flow events, i.e. the stress contribution, as $S_{f,i} = \frac{1}{T}\int_0^T u'w'\big|_i \, dt$ where i indicates the i-th event and T is the total experiment time. The time average is replaced by ensemble average in this case. The duration fraction, $D_i=N_i/N_{total}$, can also be defined where N_i indicates number of samples for i-th event while N_{total} indicates the number of all samples. The duration fraction represents the frequency of different flow events. Based on these definitions, the total Reynolds shear stress $\overline{u'w'}$ at y/H=0.18 is decomposed into four parts as in Fig. 6.3a. The symbols and solid lines represent the mean trend of results from different streamwise locations while the thin dashed lines indicate the variation along the streamwise direction. The behaviors are consistent with typical behaviors in canopy turbulence. The ejection and sweeping motions contribute mostly to the total shear stress. Close to the canopy, sweeps have larger contributions than ejections. As elevation increases, such as z/H>1.15, ejections become dominant. Associated with the stress fraction, the duration fraction shows opposite trends as in Fig. 6.3b. Near the canopy top, sweeps happen less frequently than ejections while the former contribute more to the total shear stress. When sweeps happen more frequently than ejections at higher elevations, sweeps actually have less contribution to the shear stress. These opposite trends between stress fraction and duration fraction can also be observed from data at other spanwise locations, such as at y/H=-0.16 in Figs. 6.3c and d. Throughout the flow regions above the canopy in general, a more intermittent motion has a larger contribution to the total shear stress. A motion that happens more frequently actually has less contribution.

The roles of sweeps and ejections vary at different spanwise locations. For example at y/H=-0.16, ejections play a dominant role throughout the boundary layer, which agrees with known behaviors in smooth-wall boundary layers. This trend seems to be in accordance to the trends in Reynolds stresses in Fig. 6.2c where the stresses decrease monotonically with height without a secondary peak above the canopy. On the other hand, at locations where the Reynolds stresses display a secondary peak, such as at y/H=0.18 in Fig. 6.2b, the dominance of sweeps and ejections switches as height increases. Furthermore, the location where the stresses peak coincides with the location of the crossover point of trends in sweeps and ejections, i.e. at z/H=1.15 in Figs. 6.3a and b. Similar to the profiles of mean velocities and Reynolds stresses, the quadrant behaviors at locations with sparse branches underneath are similar to the top part of profiles at other locations with dense branches underneath. Future studies with vertical velocity measurements inside the canopy as well as studies of the displacement height at these different places could complete the pictures of flows across the whole canopy.

In the above sections, the profiles of mean velocities and Reynolds stresses, as well as the quadrant events show significant dependencies as function of spanwise location. However, coherent structures also display some common features at all locations. In the following sections, we focus on these common features, and describe results based on the data at y/H=0.18 for conciseness. Specifically, we study the structure inclination angles and the small-scale coherent structures.

6.4 Coherent structures and their inclination angle

A typical instantaneous velocity field is shown in Fig. 6.4 where a constant streamwise velocity of 0.3 m/s has been subtracted in order to visualize the flow structures more clearly. Meanwhile, the fluctuation velocity field is shown in Fig. 6.5 where locally ensemble-averaged mean velocity has been subtracted. First of all, a vortex street consisting of clockwise rotating eddies can be observed from x/H=0.05 to 0.4 in both cases. Such vortex streets resemble the vortex packets in previous studies of classic wall turbulence. Adrian et al. (2000) proposed the hairpin vortex structure to explain the momentum transport in wall-bounded flows. Each rotating eddy may represent the head of possible hairpin structures. Several hairpin structures can then align in the streamwise direction and form a vortex street. In addition to these patterns which are often observed in classic wall-bounded flows, we can observe some distinct features in our instantaneous vector map as well. For example, around x/H=0, one can observe a jet-like structure with strong vertical motions. Such a structure can cover a large domain, for example from x/H=-0.15 to 0.15, and greatly disrupt the flow field as well as the vortex street. More interestingly, this jet-like structure is directly ejected from the regions inside the canopy. Such behavior cannot be expected in typical boundary layer flows where the walls are solid. In our case, on the other hand, the "wall" consists of highly porous structures. When the pressure above the canopy is lower than that below, one could expect such jet-like vertical motions. These can greatly enhance the mixing and the momentum and energy transport in the flow. This phenomenon may also have possible linkages to particle transport processes in real canopies. Nathan et al. (2002) proposed a mechanism of long distance seeds dispersal by wind. The long distance dispersal (LDD) is basically due to the events of seed uplifting. They concluded that the effects of gusts and rapid fluctuations in the wind that occur under near-neutral atmospheric conditions were the most important processes for seed uplifting, and hence LDD. Combining our observations in the instantaneous flow field where very strong vertical motions eject from the regions inside the canopy, we may suspect that particles and scalars such as temperature could be lifted up to a much higher elevations during these ejection events. Then due to larger wind speeds and stronger convective motions in the horizontal direction at higher elevations, one may expect a long distance transport of particles as well as strong mixing of scalars. Quantitative validation of such hypotheses is beyond the objectives of the present study but could be an interesting direction for future studies.

To further visualize and quantify the coherent structures, we apply linear stochastic estimation (LSE), which is used to estimate the average velocity field based on specific conditions in the flows. It was applied to previous studies of wall flows to identify the coherent structures based on positive swirling strength (e.g., Christensen and Adrian 2001; Hambleton et al. 2006; Volino et al. 2009; Hong et al. 2011). A complete derivation of LSE is presented in Adrian and Moin (1988). In our present study, the LSE based on positive swirling strength is evaluated based on

$$\overline{u_i'\left(x_{ref}+\Delta x, z_{ref}+\Delta z\right)\Big|\lambda\left(x_{ref}, z_{ref}\right)>0} = \frac{\overline{\lambda\left(x_{ref}, z_{ref}\right)u_i'\left(x_{ref}+\Delta x, z_{ref}+\Delta z\right)}}{\overline{\lambda\left(x_{ref}, z_{ref}\right)\lambda\left(x_{ref}, z_{ref}\right)}}\lambda\left(x_{ref}, z_{ref}\right), \quad (6.1)$$

where u_i' is the fluctuating velocity vector and λ is the swirling strength. The swirling strength is closely related to vorticity, but discriminates between vorticity due only to shear and vorticity resulting from rotation. It is defined as the imaginary part of the complex eigenvalue of the local velocity gradient tensor (Zhou et al. 1999). For 2D measurements, swirling strength is calculated from the in-plane velocity components (Hutchins et al. 2005; Volino et al. 2009). At a given z_{ref}, the averaging is performed among pairs with the same Δx and Δz, and then over all 2000 vector maps.

An example of the LSE results at y/H=0.18 is shown in Fig. 6.6a. The conditioning point is located at z/H= 1.21 and is indicated by the dot. For clarity, only one-fourth of vectors in x-direction and one-third of vectors in z-direction are shown. Following common practice in LSE analysis, each vector is normalized by its own magnitude, thus the vectors indicate only the averaged flow direction. Such normalization displays the structures more clearly, however the relative strength of the velocity at different locations cannot be distinguished. As a reference, the non-normalized LSE result is shown in Fig. 6.6b where large velocity shows around the sampling point while the velocity is weaker away from it. In both cases, similar flow patterns can be observed. First of all, a tilted large-scale flow pattern can be observed. This distinct pattern extends to the top of the boundary layer in the z-direction and to more than twice of the boundary-layer height in the x-direction. The strong upward motion is directly ejected from regions inside the canopy. Both downstream and upstream of this ejection motion, sweeping motions are observed. At the interface of the ejection and sweep, shear layers indicated as a 'crease' can be identified and denoted as A, B, and C in the plot. In wall flows, a continuous shear layer extending both upstream and downstream of the reference point has typically been observed (Christensen and Adrien 2001; Volino et al. 2009). In the present case, however, one cannot observe a continuous layer. Instead, shear layer A is separated from B by a strong ejection motion upstream of the reference point. Moreover, all shear layers (A, B, and C) and the overall structure incline at an angle of about 36°.

Such a shear layer inclination angle is much steeper than angles observed in solid wall flows before, typically about 14° (Christensen and Adrian 2001; Volino et al. 2009).

From a statistical point of view, the coherent structures could also be examined by two point correlations of flow quantities. The two point correlation of quantities *a* and *b* can be written as

$$R_{a,b}\left(\Delta x,\Delta z\right)=\frac{\overline{a\left(x_{ref},z_{ref}\right)b\left(x_{ref}+\Delta x,z_{ref}+\Delta z\right)}}{\sqrt{\overline{a^2\left(x_{ref},z_{ref}\right)}}\sqrt{\overline{b^2\left(x_{ref}+\Delta x,z_{ref}+\Delta z\right)}}} \tag{6.2}$$

where Δx and Δz indicate the spatial distances between the point of interest and the reference point in the streamwise and vertical directions, respectively. At every z_{ref}, the correlations are averaged both in the streamwise direction and over all 2000 vector fields. Some examples of two dimensional correlation maps are shown in Fig. 6.7 where Fig. 6.7a and b show the correlation between streamwise fluctuation velocity u'. When the reference point is located at the top of the canopy as in Fig. 6.7a, the correlation map at the downstream part is inclined while the upstream part tends to be more horizontal. This is likely a consequence of a rapid decrease of correlation inside the canopy due to the creation of small-scale motions and breakdown of large-scale flow by canopy elements (Shaw et al. 1995). As the height of the reference point increases, a more elliptical shape of the correlation contour appears and structures incline at both downstream and upstream directions. Meanwhile, as the height of the reference point increases, the size of the structure increases. For example, for a reference point at z/H=1.15 in Fig.6.7b, the correlated structures extend along the streamwise direction with size comparable with the height of the canopy. In the vertical direction, structures extend almost to the top of the boundary layer.

The correlation of vertical fluctuating velocity w', i.e. $R_{w,w}$, is shown in Figs. 6.7c and d. The structures extend in the vertical direction without inclination in the streamwise direction as in $R_{u,u}$ which is tied to the common convection velocity of hairpin packets. The size of the structure in $R_{w,w}$ is much smaller than that in $R_{u,u}$, especially in the streamwise direction.

To further quantify the coherent structures in detail, we focus on the inclination angle. As described in the introduction, the angle is also an important parameter in various wall models in numerical simulations. In typical wall-bounded turbulence, the inclination angles are about 12° to 20° which are shown from both instantaneous visualizations and correlation methods. In the present case, since some distinct flow features are observed in the instantaneous flow field, it is of interest to quantify the inclination angle of the coherent structures above the canopy. Also, in order to directly compare our estimation to the angle in typical wall flows, we adapt a method based on lead-lag correlation from two-point correlation function (e.g., Carper and Porte-Agel 2004; Marusic and Heuer 2007). We look at the correlation between streamwise fluctuation velocity, when the reference point is fixed at the top of the canopy, i.e. $z_{ref}/H=$ 1.02. In Fig. 6.8a, $R_{u,u}$ is now plotted as a function of the relative streamwise distance between a moving point and a reference point, i.e. as function of Δx. Different lines indicate correlation values when the moving point is located at different elevations. For example, the solid black line indicates that two points locates at the same elevation which is z/H=1.02 in this case. One should expect the highest correlation when these two points coincide. It provides zero streamwise delay, i.e. $\Delta x^*=0$. As the height of the moving point increases, the magnitude of the correlation gradually decreases. Meanwhile, due to the inclination of the coherent structures, the location of the maximum correlation shifts in the streamwise direction. From the spatial delay Δx^* of the peak correlation and the vertical distance between two points Δz, one can estimate the inclination angle of the prevalent flow structures. The relation between these two quantities is shown as the insert in Fig. 6.8a. By fitting a straight line to the data in a plot of Δz versus Δx^*, the inclination angle, γ, can be estimated from the slope of the line, i.e.

$$\gamma = \arctan\left(\Delta z / \Delta x^*\right). \tag{6.3}$$

Furthermore, in order to make sure that the results in Fig. 6.8a are not due to the special choice of the reference point location, we check the dependence of the results on the referent point location. The same analyses are performed for reference points at seven different elevations, from $z/H=1.02$ to 1.3. As can be seen in Fig. 6.8b, all data show similar trends, which confirms the robustness of the results.

The analyses performed above are based on data at a spanwise location $y/H=0.18$. The steep inclination angles are observed at other spanwise locations as well. To summarize the results, we apply the same procedure to the velocity correlations at different spanwise locations, and then evaluate the variation of the trends. In Fig. 6.8c, the solid line indicates the mean of data from all spanwise locations, while the dashed lines indicate the variation of the angles as evaluated at different y. In general, the inclination angle of the coherent structures in the entire flow field is about 36°±5°. The high inclination angle is consistent with the coherent structures observed from the LSE results presented in Fig. 6.6. The structures are inclined with a much steeper angle than that in typical solid-wall boundary layer flows.

In previous studies of canopy turbulence, the inclination angles were mostly based on the two-dimensional correlation maps rather than lead lag correlation. The inclination angle of the major axis of the ellipse was found to be about 15° to 20° relative to the wall (Raupach et al. 1991; Finnigan 2000; Dupont and Burnet 2008, 2009). One could then suspect that the angle in canopy turbulence is comparable with the angle in typical wall-bounded flows. However, as indicated by Shaw et al. (1995), the tilted major axis may not represent the inclined coherent structures well. In their studies of two-points velocity statistics in flows above a model canopy, they estimated the inclination angle (18°) in the two-dimensional correlation map, as well as an angle (39°) based on the time lags to maximize the correlation. They further indicated that the later method, which was similar to the lead-lag correlation we used here, placed emphasis on dominant flow patterns, while the two-dimensional correlation field could be diluted by less coherent turbulent motions which would exhibit smaller slopes in the correlation contours. As a result, the 39° angle was argued to be more representative of the slope of the coherent structures even if the angle of the major axis in the two-dimensional correlation map is smaller than the inclination angle derived from lead-lag correlation. Such behavior is also confirmed by other studies of boundary layer flows (e.g., Chauhan et al. 2013).

In studies of typical wall-bounded flows, the lead-lag correlation is widely used and provides values of the angle that are consistent with instantaneous visualizations. In order to compare the structure inclination angles in canopy turbulence and in wall flows, it is better to utilize same analysis framework. A few papers in the canopy literature mentioned the lead-lag correlation (Baldocchi and Meyers 1988; Finnigan 1979; Raupach et al. 1991). However, no information of angle was deduced from the lead-lag correlation in these studies. Based on some existing data in previous canopy turbulence literature, we could estimate the angle following the lead-lag correlation method. In paper by Raupach et al. (1991), lead-lag correlations map were provided where the reference located at z/H=2 while the moving point located at three elevations, i.e. z/H=2, 1.5, and 1. Based on the delayed correlation, the inclination angle could be about 45°, much steeper than the angle from two dimensional correlation map which was about 18°. Figures of two dimensional correlation map and the lead-lag correlation are shown in Fig. 6.9 which are adopted from Raupach et al. (1991) (Figs. 10 and 11 in their paper). Similarly, Finnigan (1979) showed the time delay as a function of height. By using their data, we estimate the angle that could even reach to 60°. These newly estimated results and the angle deduced in our present study confirm a significantly larger inclination angle of coherent structures in canopy turbulence than in typical wall flows bounded by solid walls. The steeper angle may be associated with the strong vertical jet-like motions as observed in the instantaneous vector maps. Such structures could lift up the typical vortex street to a higher elevation, and a higher inclination angle could be expected.

6.5 Coherent structure at small scales

In order to further evaluate a coherent structures at different scales, especially at small scales, we study the flow signatures in the spectrum and then apply the spatial filtering techniques to analyze the flow structures at small scales in this section.

The energy spectrum E_{uu} at y/H=0.18 is shown in Fig. 6.10a. Different lines indicate data at different elevations. As elevation increases, the energy contained at all scales gradually decrease. At large scales, however, it decreases more rapidly than that at small scales. Beyond the inertial range where the Kolmogorov scaling holds, the spectrum shows a small bump at small scales, for example at k=3000 (1/m). The size of the corresponding flow structure, about 2 mm, is comparable to the smallest branches. In turbulent boundary layers above a rough wall, Hong et al. (2011) noticed spikes in the spectrum which could be associated with the roughness height and wavelength of the roughness pattern. In canopy turbulence, a spectral short-cut mechanism has been proposed (Finnigan 2000) and tested (Cava and Katul 2008). The elements in the canopy interact with the turbulence, producing structures at scales comparable with the size of the canopy elements. As a result, the turbulent kinetic energy at large scales or mean flow could be directly converted into energy at smaller scales, bypassing the typical energy cascading process. In these cases, the signature of the elements can be represented in the energy spectrum. In Fig. 6.10b, the normalized energy spectrum is shown where the dissipation is estimated from the Kolmogorov scaling in the inertial range, i.e. $E_{11}=18/55C_k\varepsilon^{2/3}k_1^{-5/3}$ where C_k is the Kolmogorov constant. The data at different elevations collapse well in the normalized energy spectrum. Beyond the inertial range, one can also observe a small bump at small scales.

In Fig. 6.10c, the shear spectrum, $-E_{uw}$ is shown. The solid black line indicates the $k^{-7/3}$ law (Lumley, 1967). The shear spectrum indicates the contribution to momentum transport from the various scales of motions. In isotropic turbulence, the shear spectrum is zero. Shear flows with shear rate S can cause turbulence to be anisotropic. Following the approach proposed by Lumley (1967), and Saddoughi and Veeravalli (1994), characteristic length scale and velocity scale could be formulated based on the dissipation rate and mean shear rate, as $L_s=\varepsilon^{1/2}S^{-3/2}$ and $u_s=(\varepsilon/S)^{1/2}$. In the present case, we use $S=\partial U/\partial z$. By using these characteristic scales, the normalized shear spectrum is shown in Fig. 6.10d. The data collapse quite well in the inertial range.

In both energy spectrum and shear spectrum, the signal lifts up noticeably at high wavenumbers (small scales). The coherence of these small scales can be studied more clearly through the correlation spectrum, which is defined as:

$$Co(k) = -\frac{E_{uw}(k)}{\sqrt{E_{uu}(k)E_{ww}(k)}} \tag{6.4}$$

where E_{uu} and E_{ww} are the longitudinal and transverse spectrum, and E_{uw} is the shear spectrum. The correlation spectrum is the Fourier transform of the cross correlation between two signals, and indicates their coherence at different scales. In classic turbulence, as indicated by Kolmogorov's second hypotheses, for sufficiently high Reynolds number, the small scale turbulence forgets the large scale boundary conditions. As the result, the flow becomes homogeneous and isotropic at small scales and the correlation should vanish. Saddoughi and Veeravalli (1994) showed the correlation spectrum in their boundary layer studies with large correlation at small wavenumbers while the correlation at large wavenumbers was negligible, consistent with Kolmogorov's second hypothesis.

The measured correlation spectrum at y/H=0.18 is shown as in Fig. 6.11. Different lines indicate results from different elevations. At high elevation, i.e. z/H=1.5 as indicated by the green, diamond symbols, the correlation value is high at large scales. As scale decreases, the correlation decreases gradually and approaches zero at about *k*=1000 (1/m). Beyond this wavenumber, the correlation remains zero. It indicates that at small scales, there are no flow structures transporting mean momentum and the flow becomes statistically homogeneous and isotropic. On the other hand, at lower elevations close to the canopy top, the trend becomes different from what was observed in previous studies. For example at *z/H*=1.1 as indicated by the red circles, the correlation value first decreases as wavenumber increases and then increases again at large wavenumber. It indicates that in addition to the large-scale flow structures, the flow also contains small-scale structures that transport mean momentum. In general, these small-scale structures become apparent at regions close to the canopy top, for example at *z/H*<1.3. As elevation increases, the correlation spectrum gradually shifts to traditional behaviors. Such gradual transition indicates the lift-up at high wavenumber represents the actual flow physics at small-scales, although the spatial resolution in present study cannot resolve the smallest flow motions. If high magnification measurements could be obtained, one may observe that the correlation spectrum at region close to canopy will lift up at high wavenumber and then will gradually decrease at very small scales. As a result, a secondary correlation peak may be observed at high wavenumber. The identification of these possible correlation peaks and the flow motions at very small scales will leave for future studies.

In our present study, due to strong interactions between regions inside and above the canopy, the motions such as the jet-like ejections described in Fig. 6.4 could interact with the tree branches before entering the boundary layer above the canopy. At the fifth generation, one single tree has 243 branches of diameter 1.8 mm. These small-scale branches could generate flow structures with size comparable to the size of the branches. In addition, the structures presumably generated by the larger branches at lower generations would eventually break down to small-scale motions comparable with the size of the smallest branches, since these branches located at the highest elevations serve as spatial filters to produce small-scale wakes. Such small-scale structures can then be carried by strong ejecting motions and be imbedded in the flow above. As a result, besides typical large-scale coherent structures, we could observe coherence at small scales.

The small-scale flow motions can be clearly observed from the conditional averaged vector field as well. As examples, we choose the reference points at $z/H=1.09$ and 1.5, respectively. The conditioning criterion is the highest small-scale shear stress, i.e. the selected samples are with highest 10% value of $|u''w''|$ among all samples. The results are shown in Fig. 6.12. As one can see, close to the canopy as in Fig. 6.12a, a clear rotating eddy can be observed. On the other hand, at high elevations, as in Fig. 6.12b, one cannot see a distinct pattern. The surrounding flow is statistically quite homogeneous and isotropic.

The results described above indicate that besides large-scale coherent structures which are often observed in typical wall-bounded flows, our flow above a canopy also contains coherent, mean momentum transporting structures at small scales. These small-scale motions could be associated with the wake structures generated during the interactions between the tree branches and the strong vertical motions ejecting from regions inside the canopy. Further time-resolved flow measurements could be applied in future studies to reveal the mechanisms in details. Here, we make some comments on the effects of small-scale coherent motions on the LES. In LES, the flow motions with size above the filter scale are fully resolved. The unresolved motions with size smaller than the filter scale are modeled based on the resolved flow field according to various assumptions. The models often assume the unresolved flow motions are homogeneous and isotropic. Consequently, the small-scale coherent structures observed here could pose new challenges for existing subgrid-scale models in LES.

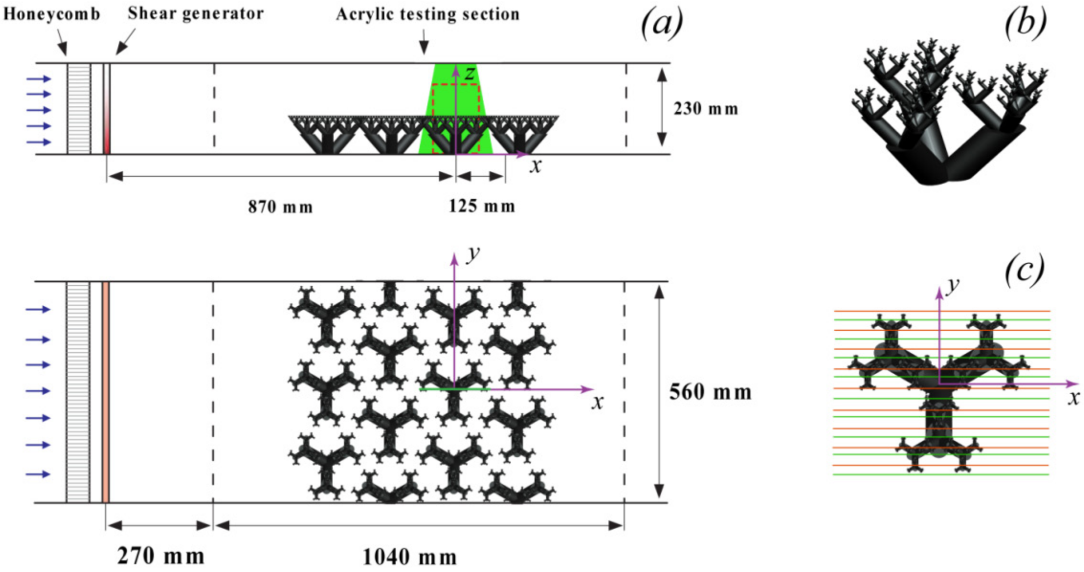

Figure 6.1 Experimental set-up of flows above a fractal canopy: (a) test section and canopy model; (b) perspective view of a fractal tree; and (c) top view of the target tree where the lines indicate the locations of sampling planes.

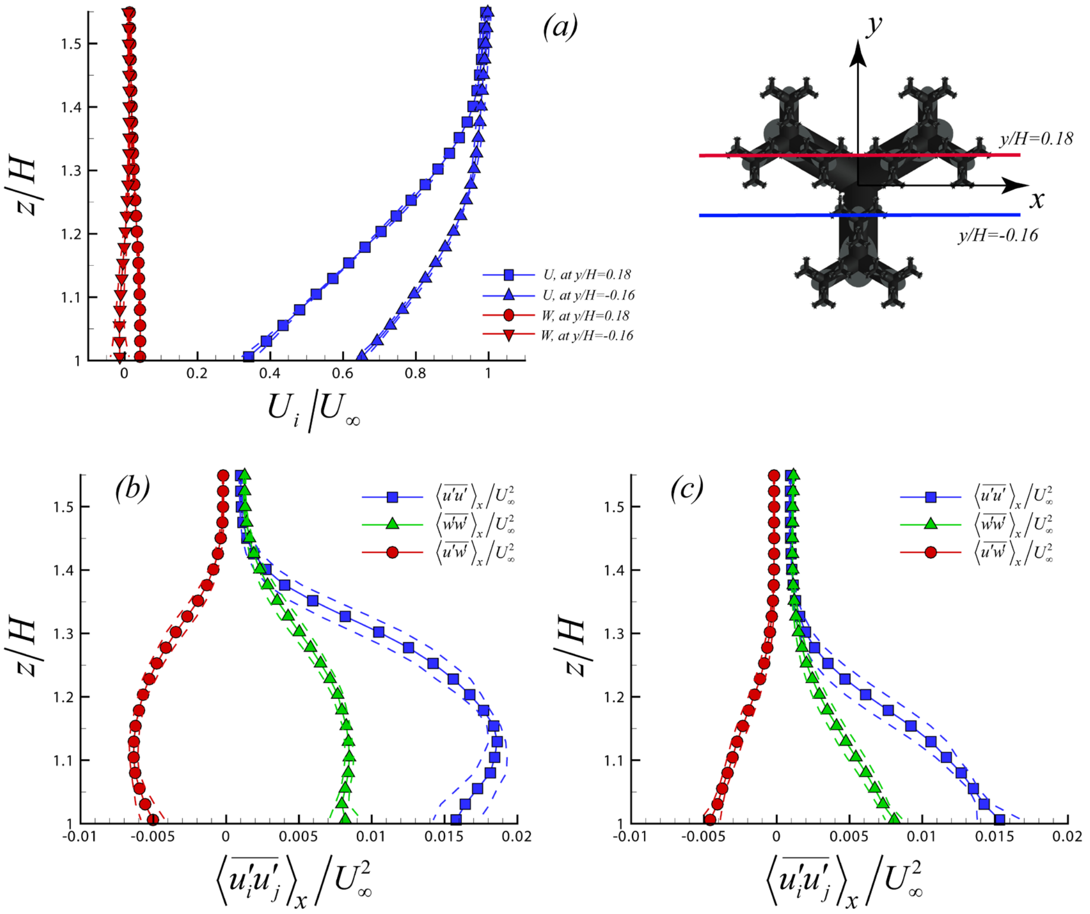

Figure 6.2 (a) Typical profiles of mean velocities above the canopy. Reynolds stresses (b) at *y/H*=0.18 and (c) at *y/H*=-0.16.

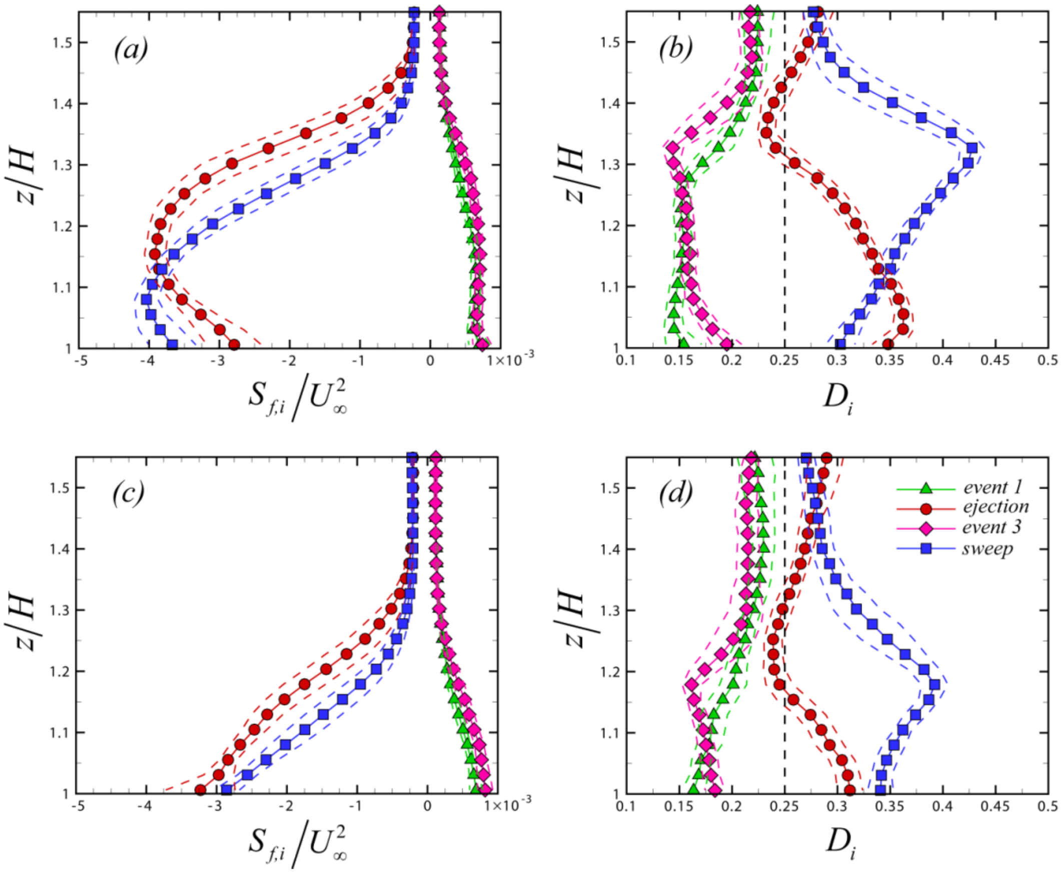

Figure 6.3 Quadrant analysis. The shear stress contributions (a) and duration fraction (b) of four quadrant events at *y/H*=0.18. The stress contributions (c) and duration fraction (d) at *y/H*=-0.16.

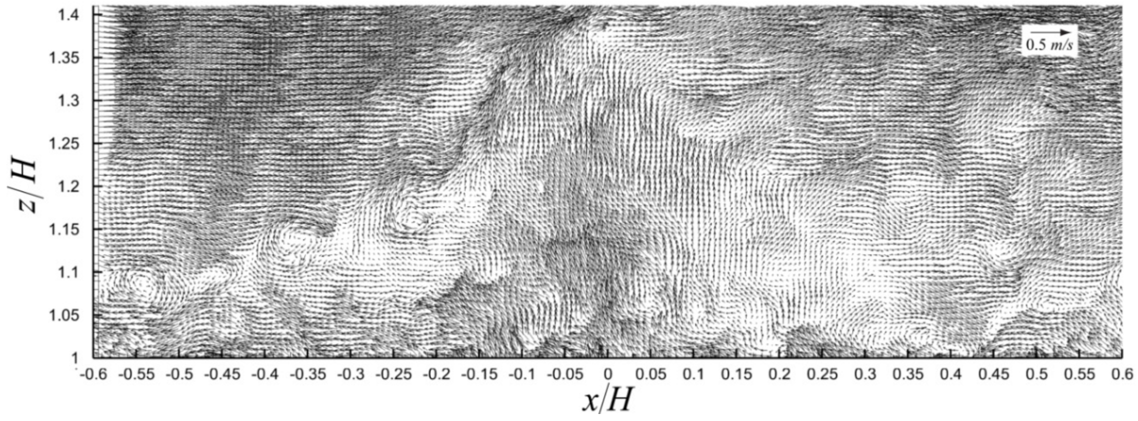

Figure 6.4 Instantaneous velocity field above the canopy where a constant streamwise velocity 0.3 m/s has been subtracted.

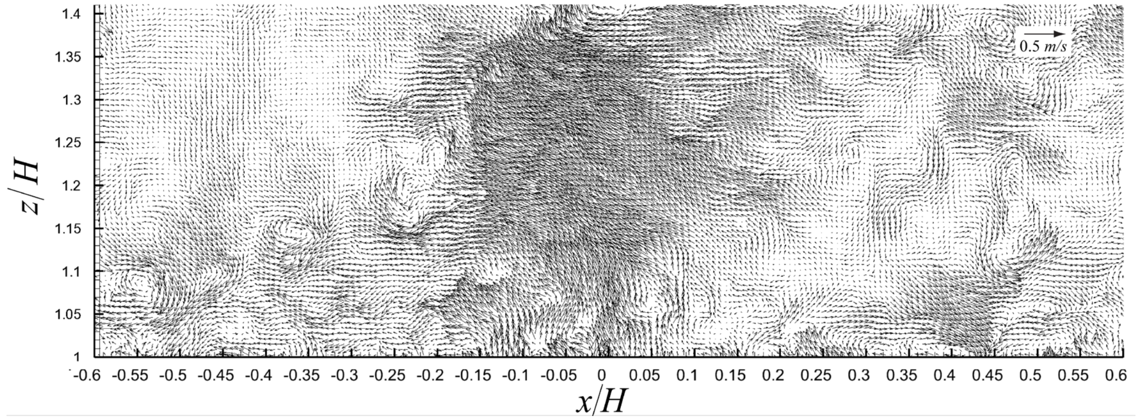

Figure 6.5 Fluctuation velocity field above the canopy where the locally ensemble-averaged velocity has be subtracted.

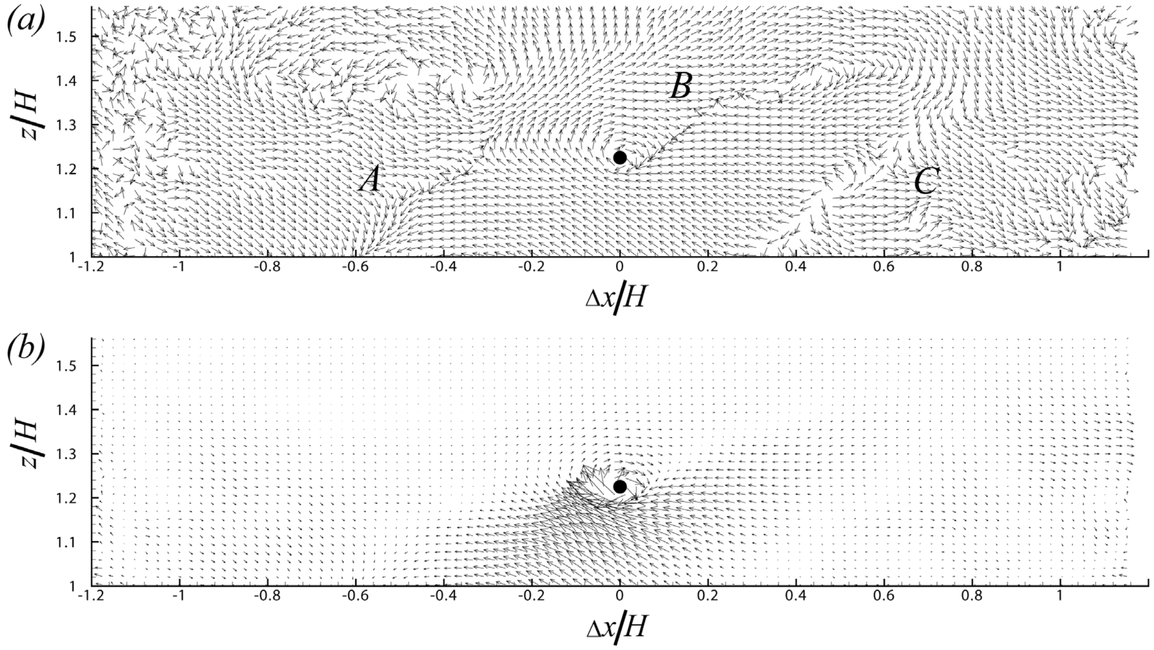

Figure 6.6 Linear stochastic estimation based on positive swirling strength. One fourth of vectors are shown for clarity. (a) The vectors are normalized by their own magnitude. As a result, vectors have unit length. (b) Non-normalized vectors are shown which are deduced from Eq. 6.1.

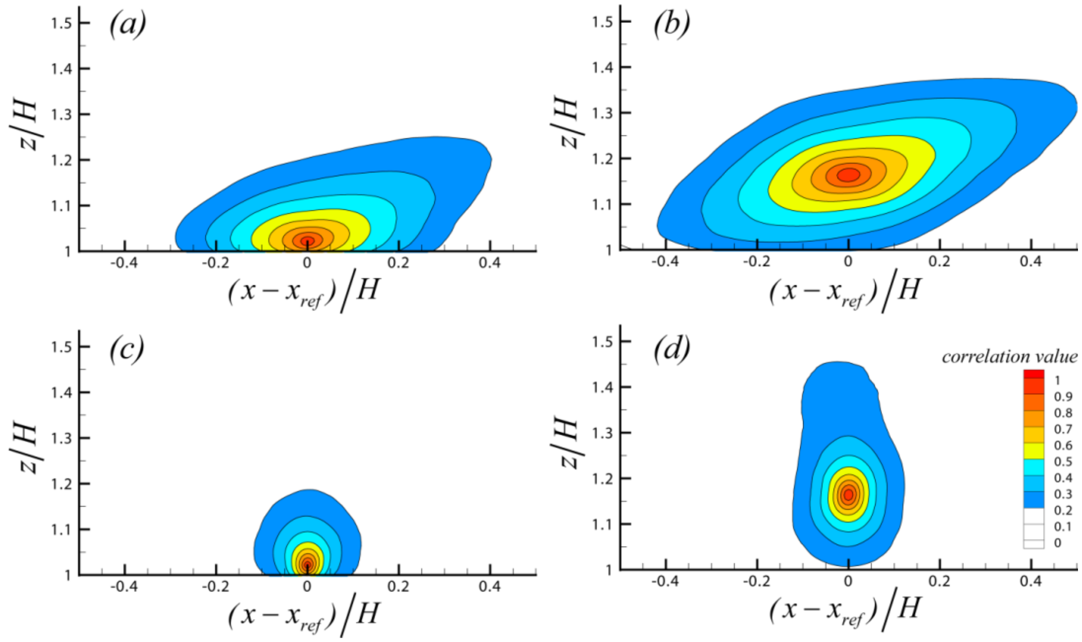

Figure 6.7 Two-dimensional correlation map. The correlation based on the streamwise velocity, $R_{u,u}$, is shown in (a) and (b). The correlation based on vertical velocity, $R_{w,w}$, is shown in (c) and (d). The reference point locates at z/H=1.02 in (a) and (c), and at z/H=1.15 in (b) and (d).

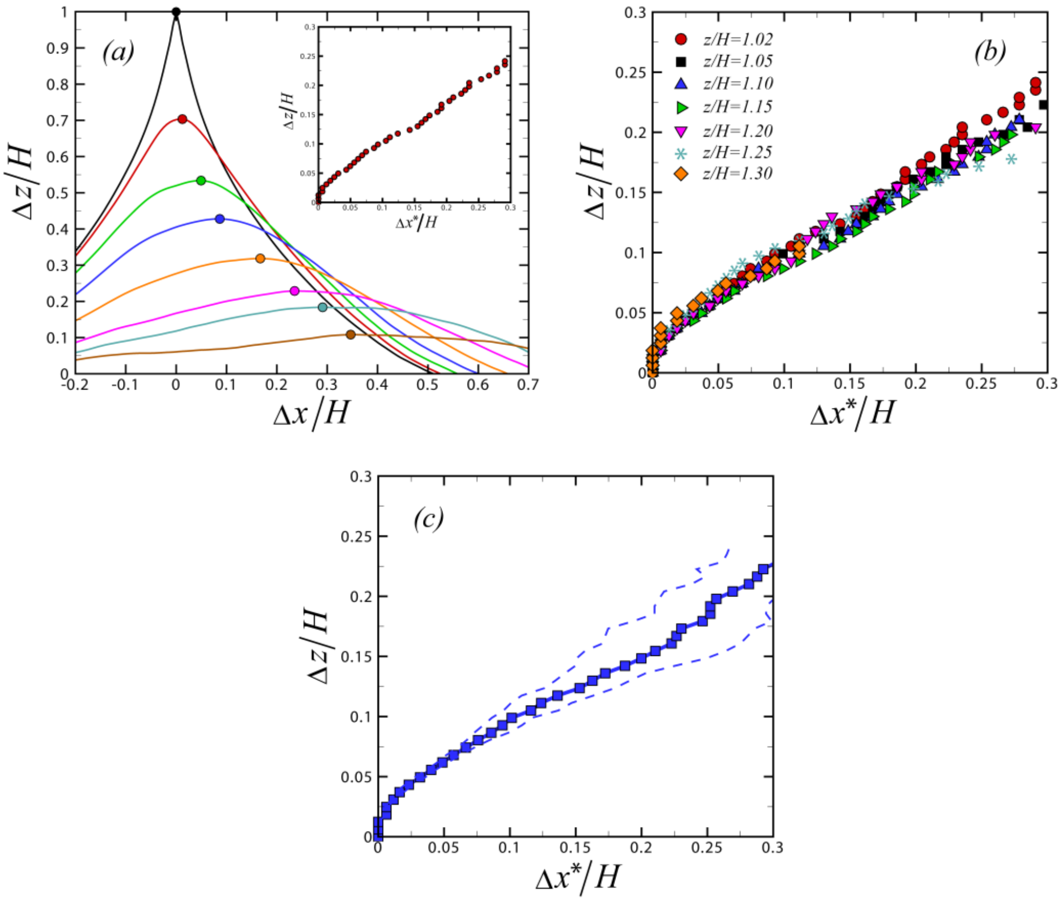

Figure 6.8 Lead-lag correlation from the two-point correlation and spatial delays. (a) The lead-lag correlation when the reference point locates at *z/H*=1.02. The insert is the spatial delays ofΔx^* and Δz accordingly. (b) Spatial delays obtained by changing reference point elevation. (c) Results of spatial delays at different spanwise locations, where solid line is the mean trend and dashed lines indicate variations.

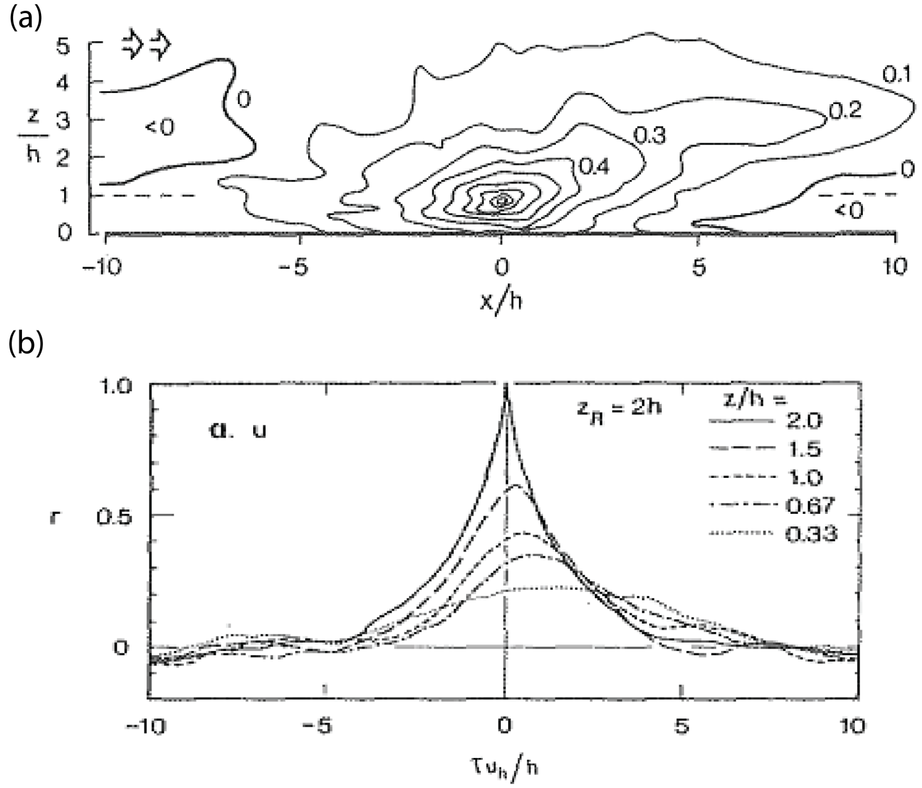

Figure 6.9 Two dimensional correlation map (a) and lead-lag correlation (b) adopted from Raupach et al. (1991).

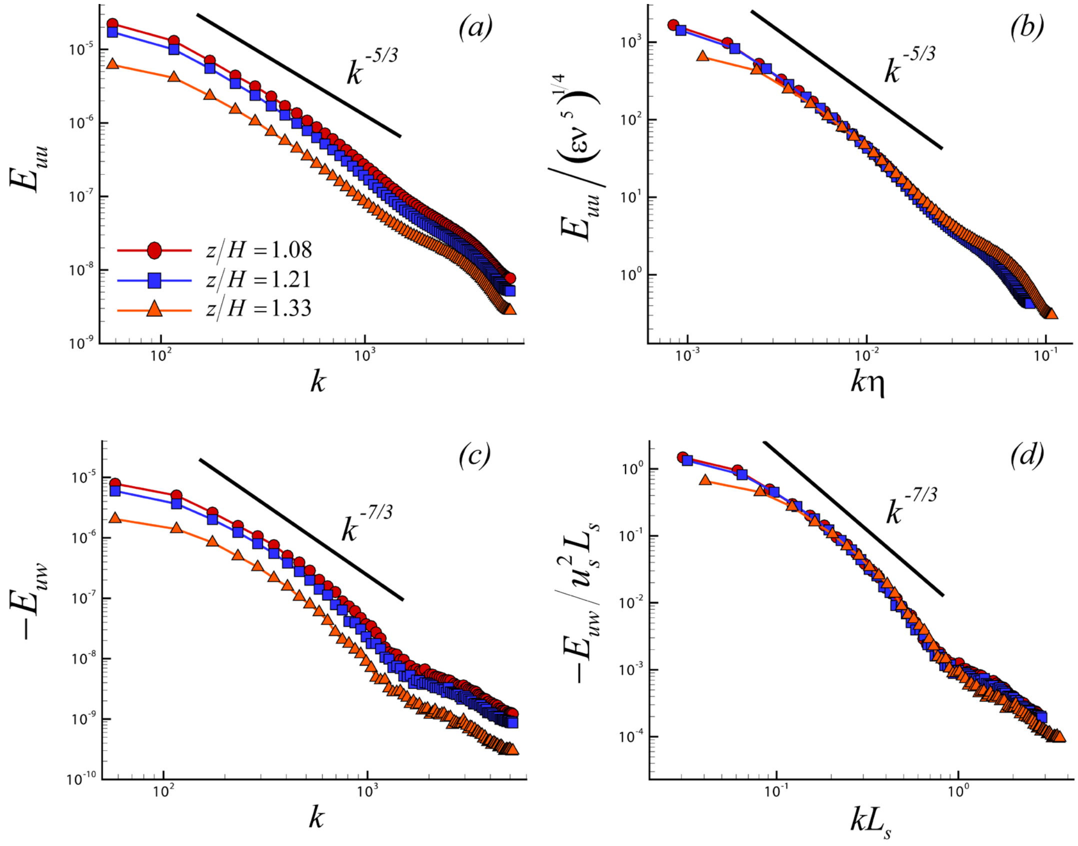

Figure 6.10 The energy spectrum and shear spectrum calculated at three elevations. (a) The energy spectrum. (b) Normalized energy spectrum based on dissipation and Kolmogorov scales. (c) Shear spectrum. (d) Normalized shear spectrum based on a velocity scale and a length scale which involve mean shear rate, as suggested by Saddoughi and Veeravalli (1994).

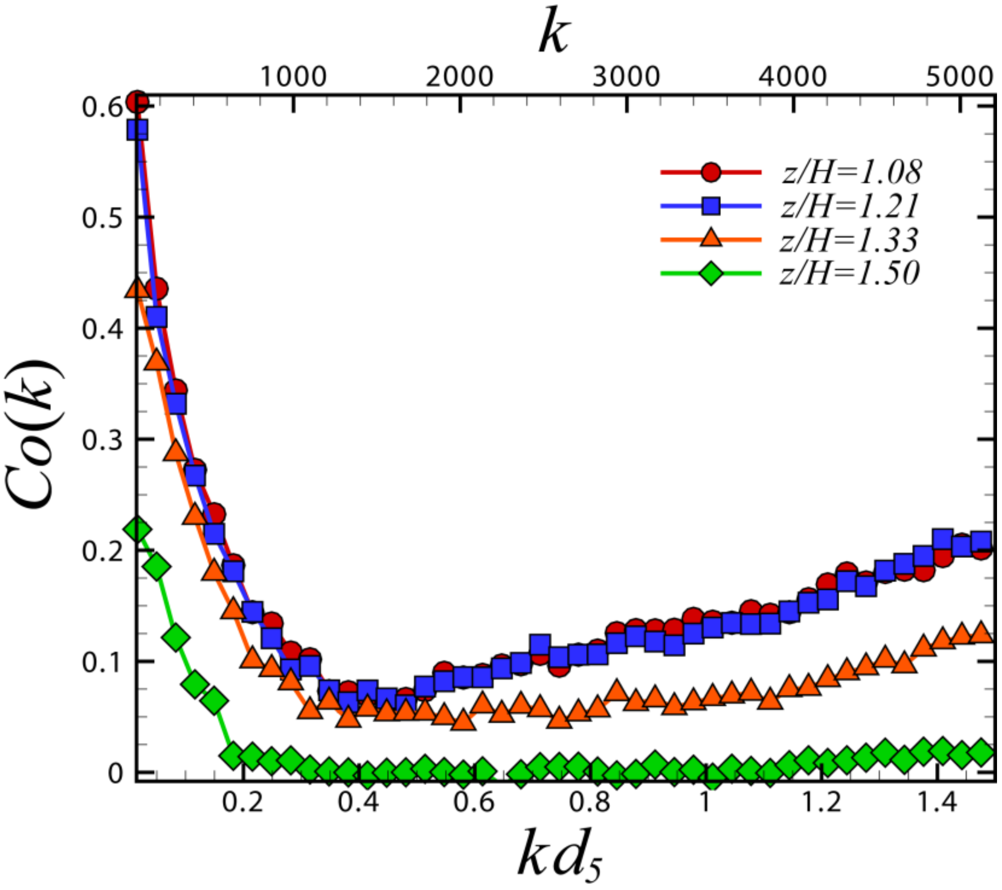

Figure 6.11 The correlation spectrum as a function of wavenumber, where the size of the smallest branch is indicated as d_5.

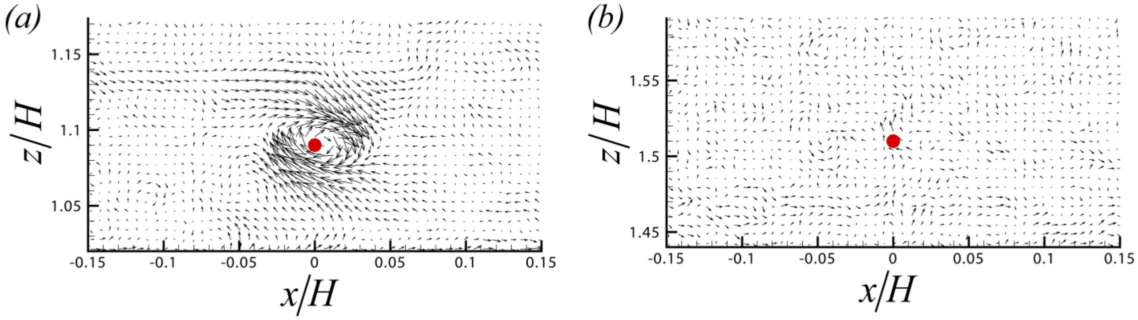

Figure 6.12 (a) Coherent small-scale motions from the conditional average close to canopy. Clear rotating motion can be observed. (b) Small-scale motions away from the canopy where surrounding flows are homogeneous and isotropic.

Chapter 7. Summary and Conclusion

In order to understand canopy turbulence generated by multi-scale structures, we have performed a series of systematic studies in a canopy model with fractal tree-like elements. We have focused on how the multi-scale elements affect the momentum and energy transport in this turbulent flow, as well as on the characteristic length scales that quantify and control these processes. In the next subsections 7.1-7.4, we summarize the results from the different parts of this thesis and recall the conclusions obtained in each part Then, in section 7.5, we provide some perspectives about future studies and possible extensions.

7.1 Near-wake flow structures behind a single fractal tree

Detailed PIV measurements have been carried out in the near-wake behind a fractal tree in order to study the turbulence structure behind a multi-scale object. Geometric features of the tree shape can be observed in the velocity and turbulence profiles near the tree. Phenomena, such as wake merging and decay, are documented using detailed mean velocity and Reynolds-stress maps and profiles. The data are subsequently analyzed to determine the turbulent eddy viscosity and mixing length in the transverse (wake) plane. At all locations, the results display a good linear relationship between the spanwise Reynolds shear stress and the corresponding mean velocity gradient in the spanwise direction. Thus, the present wake evolution in the transverse direction provides support for applying the Boussinesq eddy-viscosity concept, at least in the horizontal *x*-*y* planes. Even though the flow is generated by an object with a complicated multi-scale shape, this simple concept appears to describe transverse momentum fluxes quite well. At fixed height, the measured mixing length increases with streamwise distance, consistent with trends of a standard wake expansion. By using the expected plane-wake scaling ($\sim x^{1/2}$), the profiles of mixing length at different downstream distances can be collapsed quite well into a single curve.

We find that the measured eddy viscosity and mixing length decrease with increasing elevation, which is different from the traditional eddy viscosity and mixing length behaviors reported by other researchers for dense canopies and turbulent boundary layers. Although previous studies have examined vertical transport, while our results are relevant to transverse transport, the decreasing behavior is still noteworthy. We show that it is difficult to explain this trend by using length scales that can be determined from the classic leaf area density, leaf area index or other standard quantities typically based on any single length scale. Instead, the analysis suggests that multi-scale character of the fractal tree geometry must be taken into account explicitly. In order to do so, two approaches are proposed based on the notion of superposition of scales, including the scales of clusters of branches. One model is based on the spectral approach, in which the length scales are estimated from radial spectra of the tree cross-sections. It is shown that additional considerations involving cut-off scales based on wake merging can also be included. The second model does not require numerical calculation of Fourier transforms and instead uses the fractal dimension to incorporate the multi-scale information and its associated probability densities. In addition, an improved version of the second one is introduced which provides a continuous trend. The proposed models agree well with the measured trends of the mixing length, and capture its decrease with increasing height. The agreement between the measured and modeled mixing lengths confirm that the multi-scale and clustering properties of fractal objects should be incorporated when estimating characteristic mixing lengths. The results have been obtained for a single tree and are thus relevant to very sparse vegetation canopies consisting of fractal-like objects.

7.2 Spectral energy fluxes in flows behind a single fractal tree

By analyzing the data from the near-wake of a fractal tree, we further study the kinetic energy transfer in the flows, and focus on the energy flux as well net injection rate at different scales based on the filtering framework of relevance to Large Eddy Simulations. The measured energy flux is a function of elevation and streamwise location. For fixed elevations, we notice that the profiles at various streamwise locations can be collapsed on a single curve, once the energy flux and wavenumber are normalized by the mixing length. To consider the trends of energy fluxes at different elevations, we study the difference between the flux at different scales and its constant value in the inertial range. All profiles in the entire near-wake follow the same curve, within experimental scatter. When the normalized wavenumber is smaller than one, i.e. at scales larger than the mixing length, the measured energy flux increases with scale. At scales smaller than the mixing length, the energy flux displays a plateau corresponding to a constant flux, consistent with the Richardson-Kolmogorov cascade and classical inertial range behavior.

Based on the data, the net injection rate spectrum is also evaluated. Once the wavenumber is normalized by the effective mixing length, the data collapse and decay together as a function of wavenumber. Most of the energy is injected into the flow at scales larger than the (height and generation-dependent) mixing length, which results in a gradual increase in the flux with wavenumber. When the scales become smaller than the mixing length, the energy injection becomes negligible and a constant flux is observed.

Furthermore, in accordance with dimensional reasoning and a heuristic model for anisotropy, the data confirm a $k^{-7/3}$ power law scaling for the net injection rate spectrum in the inertial range.

The fact that the mixing length, which was derived chiefly from considerations of mean shear stresses and momentum transport in previous studies, can also be used to scale intrinsic turbulence quantities, such as the energy injection spectrum, is quite interesting. The present results show that the effective length-scale determined from a weighted sum over all relevant scales can be used not only for momentum transport in the flow, but also for the scale-dependent flux of kinetic energy across eddy sizes.

7.3 Turbulence inside the fractal canopy

In order to study the turbulent structures and spatial variations of turbulent flow inside a canopy with complex geometry and multiple scales, detailed PIV measurements are carried out. The canopy consists of fractal, tree-shape objects. To overcome the inherent difficulties of measuring the flow fields between individual branches, an index-matching technique is utilized which matches the refractive indices of the tree models and the working fluid solution. The approach enables full optical paths for both light illumination and camera data acquisition. As a result, the velocity field inside this canopy with complex shapes can be measured in detail, and the interactions between trees and flow fields studied. We focus on the flow motions in the horizontal planes which reveal the importance of the dispersive fluxes and the horizontal momentum transport in the flow.

A 3D reconstruction of the distributions of flow statistics is used to show the mean velocities, Reynolds stresses, and dispersive fluxes. The tree geometry leaves its signature in the overall wake structures where the tree shape can be identified downstream of the tree region inside the canopy. The mean velocity distributions are quite heterogeneous and as a result, the dispersive flux component is significant even compared to the Reynolds stress tensor in the streamwise direction. The double averaged mean streamwise velocity displays an "S" shaped profile which has a local maximum inside the canopy. The double averaged Reynolds stresses, $\left\langle \overline{u'u'} \right\rangle$ and $\left\langle \overline{v'v'} \right\rangle$, peak at the top of the canopy. Inside the canopy, they maintain roughly constant values. The dispersive flux $\left\langle \overline{u}''\overline{u}'' \right\rangle$ has a significant contribution throughout the whole canopy and exceeds the Reynolds normal stress by a factor of four at a height of the second-generation branches. The results indicate that at least under certain condition, the dispersive fluxes can be very important and should be included when modeling the horizontally averaged structure of flows inside multi-scale canopies.

To reveal the effective length scales in the flow and to explore possible links between such scales and the complex morphology of the tree, mixing and turbulent momentum transport are studied in the framework of the eddy-viscosity model. Evidence from scatter plots of mean velocity gradient and Reynolds shear stress confirm spatial validity of the eddy-viscosity model and its application to representing horizontal momentum transport. Based on fits to these scatter plots. The eddy viscosity and mixing length are deduced as a function of height. The mean mixing length increases with elevation above the canopy, which agrees with the classic scaling in classic boundary layers. Inside the canopy, however, the mixing length gradually decreases with elevation, which is quite different from previously reported results and cannot be described by scaling based on a single length scale of the objects in the canopy. In order to capture the measured trend, a model is tested which considers the coexistence of the branches with multiple scales. The trend of the length scales based on the model agrees well with the measured data. The agreement shows that a link between the scales of flow motions and the geometry of trees, may be established, even when the geometry is complex and structures contain multiple length scales as long as one takes into account multi-scale information including the clustering properties of the fractal objects.

7.4 Coherent turbulent structures above the fractal canopy

To study the turbulent coherent structures above a canopy composed of multi-scale elements, detailed PIV measurements are carried out. Turbulence statistics, such as mean velocities and Reynolds stresses do not vary much along the streamwise direction. They, however, display variations in the spanwise direction. Two typical behaviors are observed. At locations with dense branch elements underneath, the mean streamwise velocity profile displays a strong shear region that extends to a higher elevation compared to the profile at locations with relatively sparse branch elements underneath. Accordingly, the regions with significant turbulent motions also extend to different heights at these locations. In the former case, Reynolds stresses increases first and decreases with elevation. They display a secondary peak above the canopy. On the other hand at locations with sparse elements underneath, the Reynolds stresses decreases monotonically with a maximum value at the top of canopy. The profiles in the later case are similar to the top part of profiles in the former case. It may indicate that at locations with sparse elements underneath, the entire flow structure shifts to a lower elevation inside the canopy.

Similarly, different quadrant behaviors are observed at different spanwise locations. At locations with dense elements underneath, sweeps plays a more important role in regions close to the canopy, while they happen less frequently than ejections. At high elevations, however, the ejections become dominant.

In spite of the variation in the spanwise direction, some common features of the coherent structures are found. From instantaneous velocity field visualizations, one can see jet-like motions which are ejected from regions inside the canopy. These flow motions greatly disrupt the flows above the canopy. Such behavior cannot be expected in typical boundary layer flows where the wall is solid. From linear stochastic estimation results, we observe distinct flow patterns different from those in solid-wall flows. The inclination of the structures is found to be about 36°, as estimated visually.

Statistically, the coherent structures are observed in two-dimensional correlation maps $R_{u,u}$ and $R_{w,w}$. As elevation increases, the size of the correlation contour in $R_{u,u}$ increases and is comparable with the height of tree in the streamwise direction and height of boundary layer vertically. To quantify the inclination angle of the coherent structures, we apply the lead-lag correlation from the two-point correlation of streamwise velocity. As the moving point shifts to higher elevations while the reference point is fixed, the correlation value of $R_{u,u}$ gradually decreases. Meanwhile, the location of the peak correlation shifts along the streamwise direction, which is due to the inclined coherent structure. Then, the inclination angles of the coherent structures could be estimated based on the spatial delay of the correlation peak and the vertical distance between two points. The deduced angle is robust for different elevations of the reference point. By including data at different spanwise locations, the inclination angle is found to be about 36°±5°. The deduced inclination angle of the coherent structures is much steeper than that in typical boundary layer flows bounded by solid walls. We further reanalyze some existing data in the previous literature of canopy turbulence and identify steep inclination angles as well. Based on both the instantaneous velocity field and the inclination angle of the structures, we confirm, from a geometric perspective, that the flow structures in canopy flows are quite different from those in typical boundary layer flows bounded by solid walls. Moreover, we think the lead-lag correlation should be utilized in evaluating inclination angles in future studies of canopy flows, in order to compare to results in other types of flows.

The signature of coherent structures at different scales can also be observed in the correlation spectrum. At high elevations, the correlation decreases with wavenumber and nearly vanishes at high wavenumbers. Close to canopy, on the other hand, the correlation first decreases but then, surprisingly, increases again at small scales. It indicates that besides large-scale coherent structures, the flow also contain structures at small scales that transport mean momentum and contribute to the shear stress. By applying a spatial filtering technique and conditional averaging on small-scale motions, we identify these coherent structures. It is speculated that these small-scale motions could be associated with the wake structures generated during the interactions between the tree branches and the strong vertical motions ejecting from regions inside the canopy. Further time-resolved flow measurements should be applied in future studies to reveal the mechanisms.

Moreover, the existence of small-scale coherent structures also implies that a careful determination of filter size should be evaluated in LES where flow motions with size smaller than filter size are generally difficult to represent accurately.

7.5 Possible future studies and extensions

The presently obtained laboratory measurements provide a useful database to test and refine current numerical simulation models for flows generated by multi-scale structures. In addition, a few possible future extensions are anticipated.

Further studies of drag generated by the trees in the canopy could shed light on the design of windbreaks. Also, it has relevance to a recently proposed numerical scheme to parameterize the drag effects of small-scale, unresolved branch elements (Graham and Meneveau 2012). It would also be interesting to study the drag scaling of a multi-scale tree with velocity, and compare it to classic scaling of objects with a single length scale.

In present study, planar PIV is used which provides two velocity components. To acquire three velocity components simultaneously, Stereo PIV and Tomographic PIV could be implemented for two- and three-dimensional measurements respectively. With three velocity components, full tensors of the velocity gradient tensor and Reynolds stresses could be obtained and the flow physics such as energy cascading could be studied using less assumption that were needed in the present study.

By incorporating time-resolved measurements, the evolution of the flow structures could be quantified and the source of small-scale coherent structures observed in present study could possibly be elucidated. Furthermore, time-resolved PIV measurements allow evaluating the pressure field which could provide more information about how the observed large-scale ejection motions are generated above the canopy.

In this work, to quantify the length scale distributions, models have been proposed based on the concept of weighted superposition of multiple scales. It would be valuable to test such concepts in canopies with more complex, possibly irregular foliage distributions. Moreover, it would be valuable to extend such concepts to other more general areas. For example, one could use them to quantify the highly heterogeneous structures encountered in porous media flows.

Finally, present studies focused on rigid canopy elements. As a next step, it would be valuable to consider multi-scale structures with different mechanical properties, such as elasticity, at different elevations. As a result, the flow-structure interactions could be studied and the flow effects on the structures at different scales and with different levels of elasticity could be evaluated.

Appendix A: Integral length scales in two-dimensional fields

Here we relate the radial spectrum and correlation functions in 2D and the corresponding integral length scale. For a two-dimensional field the scalar radial spectrum $E_I(k)$ can be related to the 2D spectra, $F_{2D}(\underline{k})$, by a circular averaging according to

$$E_I(k) = \int_{|\underline{k}|=k} F_{2D}(\underline{k}) d\underline{k} = 2\pi k F(k), \tag{A.1}$$

where the underline "_" indicates a vector quantity and the pre-factor $2\pi k$ is the circumference of a circle with radius k in the spectral domain. Introducing the radial-averaged correlation function $C(r) = \frac{1}{2\pi r} \int_{|\underline{r}|=r} \langle I(\underline{x}+\underline{r}) I(\underline{x}) \rangle \, d\underline{r}$, this forms a Fourier transform pair with the spectrum as

$$\begin{aligned} C(r) &= \iint e^{i\underline{k}\underline{r}} F_{2D}(\underline{k}) d\underline{k} \\ &= \int_0^\infty \left\{ \int_{-\pi}^{\pi} \cos[kr\sin\theta] d\theta \right\} F(k) k dk \, . \end{aligned} \tag{A.2}$$

Integration of the correlation function and substitution of Eq. A.1yields

$$\begin{aligned} \int_0^\infty C(r) dr &= \frac{1}{2\pi} \int_0^\infty \int_0^\infty \left\{ \int_{-\pi}^{\pi} \cos[kr\sin\theta] d\theta \right\} E_I(k) dk dr \\ &= \int_0^\infty \int_0^\infty J_0(kr) E_I(k) dk dr \end{aligned}$$

$$= \int_0^\infty \frac{1}{k} E_I(k)\, dk \,, \tag{A.3}$$

where J_0 is the Bessel function. By using Eq. A.3, the length-scale model obtained from the radial spectrum is equivalent to a model based on the correlation function according to

$$\frac{\int \frac{1}{k} E_I(k) dk}{\int E_I(k) dk} = \frac{\int C(r) dr}{C(0)} \,. \tag{A.4}$$

Appendix B: Estimating the wake merger distance

As the simplest approximation, we may additively superpose velocity defect profiles from the self-similarity theory for a classic plane wake. The combined wake-defect velocity profile $U_{w,\,i}$ corresponding to two branches in the i-th generation, can then be written as

$$\frac{U_{w,\,i}}{U_0} = 1 - \frac{1}{2}\left(\frac{8\theta_i}{\pi x}\right)^{1/2} \left\{ \exp\left(-\frac{8}{\theta_i x}\left(y + \frac{S_i}{2} \right)^2 \right) + \exp\left(-\frac{8}{\theta_i x}\left(y - \frac{S_i}{2} \right)^2 \right) \right\}, \tag{B.1}$$

where U_0 is the free-stream velocity. The spanwise location y is measured from the center of both branches (the two branches are located at $y = \pm S_i / 2$), and x is the streamwise position downstream of the branches. Also, θ_i is the momentum thickness of the objects at the i-th generation that can be related to the diameter, d_i, using $\theta_i = \frac{1}{2} C_d d_i$. For a drag coefficient $C_d \approx 1$, which is a good approximation for bluff bodies such as cylinders for a wide range of Reynolds numbers, we thus have $\theta_i \approx 0.5 d_i$. Using the profile in Eq. B.1, one may consider that the wakes have merged when the signatures of separate wakes cannot be distinguished from the combined velocity profile. Up to some downstream distance, the combined profile displays two peaks, while the center line velocity between both peaks has a local minimum. Further downstream the center line velocity becomes maximum. The transition occurs when the second-derivative at $y = 0$

is zero, i.e. $\partial^2 U_{w,\,i} \big/ \partial y^2 \big|_{y=0} = 0$. Using this condition to solve for the merging distance $x_{m,\,i}$, one obtains

$$x_{m,\,i} = \frac{4S_i^2}{\theta_i} \Rightarrow \frac{x_{m,\,i}}{d_i} \approx 8\left(\frac{S_i}{d_i}\right)^2. \tag{B.2}$$

Bibliography

Aberle J, Koll K, Dittrich A (2008) Form induced stresses over rough gravel-beds. Acta Geophys 56:584–600.

Abdulagatov IM, Zeinalova AB, Azizov ND (2006) Viscosity of aqueous electrolyte solutions at high temperatures and high pressure.Viscosity B-coefficient. Sodium iodide. J ChemEng Data 51:1645-1659.

Adrian RJ (2007) Hairpin vortex organization in wall turbulence. Phys Fluids 19:041301.

Adrian RJ, Meinhart CD, Tomkins CD (2000) Vortex organization in the outer region of the turbulent boundary layer. J Fluid Mech 422:1-54.

Adrian RJ and Moin P (1988) Stochastic estimation of organized turbulent structure-homogeneous shear-flow. J Fluid Mech 190:531-559.

Adrian RJ and Westweel J (2011) Particle Image Velocimetry. Cambridge University Press.

Averbakh A, Shauly A, Nir A, Semiat R (1997) Slow viscous flows of highly concentrated suspensions – part I: laser-dopplervelocimetry in rectangular ducts. Int J Multiph Flow 23(3):409-424.

Bai K, Meneveau C, Katz J (2012) Near-wake turbulent flow structure and mixing length downstream of a fractal tree. Boundary-Layer Meteorol 143:285-308.

Bai K, Meneveau C, Katz J (2013) Experimental study of spectral energy fluxes in turbulence generated by a fractal, tree-like object. Phys Fluids 25:110810.

Balakumar BJ and Adrian RJ (2007) Large- and very-large-scale motions in channel and boundary-layer flows. Phil Trans R Soc A 365:665-681.

Baldocchi DD and Meyers TP (1988) Turbulence structure in a deciduous forest. Boundary-Layer Meteorol 43:345-365.

Barnsley M (1988) Fractals everywhere. Academic Press Inc., U.S.A., 394 pp.

Belcher SE, Jerram N, Hunt JCR (2003) Adjustment of a turbulent boundary layer to a canopy of roughness elements. J Fluid Mech 488:369–398.

Bohm M, Finnigan J, Raupach M, Hughes D (2013) Turbulence structure within and above a canopy of bluff elements. Boundary-Layer Meteorol 146:393-419.

Brown GL and Thomas ASW (1977) Large structure in a turbulent boundary-layer. Phys Fluids 20:243-251.

Brunet Y, Finnigan JJ, Raupach MR (1994) A Wind-tunnel study of air-flow in waving wheat: single-point velocity statistics. Boundary-Layer Meteorol 70(1-2):95-132.

Brunet Y and Irvine MR (2000) The control of coherent eddies in vegetation canopies: Streamwise structure spacing, canopy shear scale and atmospheric stability. Boundary-LayerMeteorol 94:139-163.

Budwig R (1994) Refractive index matching methods for liquid flow investigations. Exp Fluids 17(5):350-355.

Burk AR (ed) (2005) New research on forest ecosystems. Nova Science Publishers, US 187 pp.

Carper MA and Porte-Agel F (2004) The role of coherent structures in subfilter-scale dissipation of turbulence measured in the atmospheric surface layer. J Turbul 5.

Carper MA and Porté-Agel F (2008) Subfilter-scale Fluxes over a surface roughness transition. Part I: measured fluxes and energy transfer rates. Boundary-Layer Meteorol 126:157.

Cava D and Katul GG (2008) Spectral short-circuiting and wake production within the canopy trunk space of an alpine hardwood forest. Boundary-Layer Meteorol 126:415-431.

Chamorro LP and Porte-Agel F (2010) Wind-tunnel study of surface boundary conditions for large-eddy simulation of turbulent flow past a rough-to-smooth surface transition. J. Turbul 11:1-17.

Chauhan K, Hutchins N, Monty J, Marusic I (2013) Structure inclination angles in the convective atmospheric surface layer. Boundary-Layer Meteorol 147:41-50.

Cheng H, Castro IP (2002) Near wall flow over urban-like roughness. Boundary-Layer Meteorol 104(2):229-259.

Chen J, Meneveau C, Katz J (2006) Scale interactions of turbulence subjected to a straining-relaxation-destraining cycle. J Fluid Mech 562:123.

Chen RC (1991) Experimental and numerical studies of solid-liquid multiphase flow in pipes. PhD dissertation, Case Western Reserve University.

Chen RC, Reese J, Fan LS (1994) Flow structure in a three-dimensional bubble column and three-phase fluidized bed. AIChEJournal40(7):1093-1104.

Christensen KT and Adrian RJ (2001) Statistical evidence of hairpin vortex packets in wall turbulence. J Fluid Mech 431:433-443.

Cionco RM (1965) A mathematical model for air flow in a vegetative canopy. J ApplMeteorol 4:517-522.

Coceal O, Thomas TG, Castro IP, Belcher SE (2006) Mean flow and turbulence statistics over groups of urban-like cubical obstacles. Boundary-Layer Meteorol 121:491–519.

Collineau S and Brunet Y (1993a) Detection of turbulent coherent motions in a forest canopy. Part 1: wavelet analysis. Boundary-LayerMeteorol 65:357-379.

Collineau S and Brunet Y (1993b) Detection of turbulent coherent motions in a forest canopy. Part 2: time-scales and conditional averages. Boundary-LayerMeteorol 66:49-73.

Cowan IR (1968) Mass, heat momentum exchange between stands of plants and their atmospheric environment. Q J R MeteorolSoc 94(402):318-332.

deLangre E (2008) Effects of wind on plants. Ann Rev Fluid Mech 40:141-168.

Domaradzki JA and Carati D (2007) A comparison of spectral sharp and smooth filters in the analysis of nonlinear interactions and energy transfer in turbulence. Phys Fluids 19:085111.

Driscoll RJ and Kennedy LA (1981) Spectral transfer and velocity derivative skewness equation for a turbulent velocity field. Phys Fluids 24:1428.

Dupont S and Brunet Y (2008) Edge flow and canopy structure: A large-eddy simulation study. Boundary-Layer Meteorol 126:51-71.

Dupont S and Brunet Y (2009) Coherent structures in canopy edge flow: a large-eddy simulation study. J Fluid Mech 630:93-128.

Dupont S, Irvine M, Bonnefond J, Lamaud E, Brunet Y (2012) Turbulent structures in a pine forest with a deep and sparse trunk space: stand and edge regions. Boundary-Layer Meteorol 143:309-336.

Ferreira RML, Ricardo AM, Franca MJ (2009) Discussion of "Laboratory investigation of mean drag in a random array of rigid, emergent cylinders" by Yukie Tanino and Heidi M. Nepf. J HydraulEng 135:690–693.

Finnigan J (1979) Turbulence in waving wheat II.Structure of momentum transfer. Boundary-Layer Meteorol 16:213-236.

Finnigan J (1985) Turbulence transport in flexible plant canopies. The Forest-Atmosphere Interaction. Dordrecht, The Netherlands: Reidel, 684 pp.

Finnigan J (2000) Turbulence in plant canopies. Ann Rev Fluid Mech 32:519-571.

Finnigan J and Mulhearn PJ (1978) Modelling waving crops in a wind tunnel. Boundary-Layer Meteorol 14:253-277.

Finnigan J and Shaw RH (2000) A wind-tunnel study of airflow in waving wheat: an EOF analysis of the structure of the large-eddy motion. Boundary-LayerMeteorol 96:211-255.

Finnigan J, Shaw R, Patton E (2009) Turbulence structure above a vegetation canopy. J Fluid Mech 637:387-424.

Frisch U (1995) *Turbulence: the Legacy of A.N. Kolmogorov.* Cambridge University Press.

Ganapathisubramani B, Longmire EK, Marusic I (2003) Characteristics of vortex packets in turbulent boundary layers. J Fluid Mech 478:35-46.

Ghisalberti M and Nepf H (2002) Mixing layers and coherent structures in vegetated aquatic flows. J Geophys Res 107.

Goldsack DE and Franchetto RC (1977) The viscosity of concentrated electrolyte solutions. I. Concentrated dependence at fixed temperature. Can J Chem-Rev Can Chim 55:1062-1072.

Goldsack DE and Franchetto RC (1978) The viscosity of concentrated electrolyte solutions. II. Temperature dependence. Can J Chem-Rev Can Chim 56:1442-1450.

Gomes-Fernandes R, Ganapathisubramani B, Vassilicos JC (2012) Particle image velocimetry study of fractal-generated turbulence. J Fluid Mech 711:306.

Graham J, Bai K, Meneveau C, Katz J (2011) LES Modeling and Experimental Measurement of Boundary Layer Flow over Multi-scale, Fractal Canopies. *Direct and Large Eddy Simulation VIII* 15:233-238.

Graham J and Meneveau C (2012) Modeling turbulent flow over fractal trees using renormalized numerical simulation: alternate formulations and numerical experiments. Phys Fluids 24:125105.

Guala M, Hommema SE, Adrian RJ (2006) Large-scale and very-large-scale motions in turbulent pipe flow. J Fluid Mech 554:521-542.

Hambleton WT, Hutchins N, Marusic I (2006) Simultaneous orthogonal-plane particle image velocimetry measurements in a turbulent boundary layer. J Fluid Mech 560:53-64.

Head MR and Bandyopadhyay P (1981) New aspects of turbulent boundary-layer structure. J Fluid Mech 107:297-338.

Heisenberg W (1948) On the theory of statistical and isotropic turbulence. Proc R Soc London Ser A 195: 402-406.

Hinze JO (1975) *Turbulence*. McGraw-Hill, New York, USA.

Hong J, Katz J, Schultz MP (2011) Near-wall turbulence statistics and flow structures over 3D roughness in a turbulent channel flow. J Fluid Mech 667:1-37.

Hurst DJ and Vassilicos JC (2007) Scalings and decay of fractal-generated turbulence. Phys Fluids 19:035103.

Hutchins N, Hambleton WT, Marusic I (2005) Inclined cross-stream stereo particle image velocimetry measurements in turbulent boundary layers. J Fluid Mech 541:21-54.

Ishihara T, Gotoh T, Kaneda Y (2009) Study of high-Reynolds number isotropic turbulence by direct numerical simulation. Annu Rev Fluid Mech 41:165.

Jiang J and Sandler S (2003) A new model for the viscosity of electrolyte solutions. Ind Eng Chem Res 42:6267-6272.

Kacperska A, Taniewska-Osinska S, Bald A, SzejgisA (1989) Influence of ionic association on the B coefficient of the Jones-Dole equation for NaI in water-tert-butyl alcohol mixtures at 26˚C. J ChemSoc Faraday Trans 85:4147-4155.

Kaimal JC and Finnigan J (1994) Atmospheric boundary layer flows: their structure and measurement. Oxford University Press, Oxford, 289 pp.

Kanda M and Hino M (1994) Organized structures in developing turbulent-flow within and above a plant canopy, using a large-eddy simulation. Boundary-Layer Meteorol 68:237-257.

Katul G, Kuhn G, Schieldge J, Hsieh CI (1997) The ejection-sweep character of scalar fluxes in the unstable surface layer. Boundary-Layer Meteorol 83:1-26.

Katul GG, Mahrt L, Poggi D, Sanz C (2004) One- and two-equation models for canopy turbulence. Boundary-Layer Meteorol 113(1):81-109.

Kelley DH and Ouellette NT (2011) Spatiotemporal persistence of spectral fluxes in two-dimensional weak turbulence. Phys Fluids 23:115101.

Kim KC and Adrian RJ (1999) Very large-scale motion in the outer layer. Phys Fluids 11:417-422.

King AT, Tinoco RO, Cowen EA (2012) A $k-\varepsilon$ turbulence model based on the scales of vertical shear and stem wakes valid for emergent and submerged vegetated flows. J Fluid Mech 701:1-39.

Kraichnan RH (1971) Inertial-range transfer in two- and three-dimensional turbulence. J Fluid Mech 47:525.

Krogstad PA and Davidson PA (2012) Near-field investigation of turbulence produced by multi-scale grids. Phys Fluids 24:035103.

Launiainen S, Vesala T, Molder M, Mammarella I, Smolander S, Rannik U, Kolar P, Har P, Lindroth A, Katul GG (2007) Vertical variability and effect of stability on turbulence characteristics down to the floor of a pine forest. Tellus B 59:919-936.

Lengyel S, Tamas J, Giber J, Holdeith (1964) Study of viscosity of aqueous alkali halide solutions. J Acta Chim Hung 40:125-143.

Li D and Bou-Zeid E (2011) Coherent structures and the dissimilarity of turbulent transport of momentum and scalars in the unstable atmospheric surface layer. Boundary-Layer Meteorol 140:243-262.

Lien FS, Yee E, Wilson JD (2005) Numerical modelling of the turbulent flow developing within and over a 3-D building array, part II: a mathematical foundation for a distributed drag force approach. Boundary-Layer Meteorol 114:245-285.

Liu S, Meneveau C, Katz J (1994) On the properties of similarity subgrid-scale models as deduced from measurements in a turbulent jet. J Fluid Mech 275:83.

Lu SS and Willmart WW (1973) Measurements of structure of Reynolds stress in a turbulent boundary-layer. J Fluid Mech 60:481-511.

Luhar M, Rominger J, Nepf H (2008) Interaction between flow, transport and vegetation spatial structure. Environ Fluid Mech 8:423-439.

Lumley JL (1967) Similarity and turbulent energy spectrum. Phys Fluids 10:855.

Macdonald RW (2000) Modelling the mean velocity profile in the urban canopy layer. Boundary-Layer Meteorol 97(1):25-45.

Mahfouf JF and Jacquemin B (1989) A study of rainfall interception using a land surface parameterization for mesoscale meteorological models. J Appl Meteorol 28(12):1282-1302.

Mandelbrot BB (1975) On the geometry of homogeneous turbulence with stress on the fractal dimension of the iso-surfaces of scalars. J Fluid Mech 72:401-410.

Mandelbrot BB (1982) The fractal geometry of nature. W.H. Freeman and Co., New York, 460 pp.

Marshall BJ, Wood CJ, Gardiner BA, Belcher RE (2002) Conditional sampling of forest canopy gusts. Boundary-Layer Meteorol 102(2):225-251.

Martilli A and Santiago JL (2007) CFD simulation of airflow over a regular array of cubes. Part II: Analysis of spatial average properties. Boundary-Layer Meteorol 122:635–654.

MarusicI and Heuer WDC (2007) Reynolds number invariance of the structure inclination angle in wall turbulence. Phys Rev Lett 99.

Marusic I, Kunkel GJ, Porte-Agel F (2001) Experimental study of wall boundary conditions for large-eddy simulation. J Fluid Mech 446:309-320.

Mazellier N and Vassilicos JC (2010) Turbulence without Richardson-Kolmogorov cascade. Phys Fluids 22(7):075101.

Meneveau C and Katz J (2000) Scale-invariance and turbulence models for large-eddy simulations. Annu Rev Fluid Mech 32:1.

Meneveau C and Sreenivasan KR (1991) The multifractal nature of turbulent energy dissipation. J Fluid Mech 224:429-484.

Moin P (2002) Advances in large eddy simulation methodology for complex flows. Int J Heat Mass Transfer 23:710.

Moltchanov S, Bohbot-Raviv Y, Shavit U (2011) Dispersive stresses at the canopy upstream edge. Boundary-Layer Meteorol 139:333-351.

Monin AS and Yaglom AM (1975) Statistical fluid mechanics, mechanics of turbulence, volume II. Dover Publications Inc., New York, U.S.A.,874 pp.

Narrow TL, Yoda M, Abdel-Khalik SI (2000) A simple model for the refractive index of sodium iodide aqueous solutions. Exp Fluids 28(3):282-283.

Nathan, R., Katul, G.G., Horn, H.S., Thomas, S.M., Oren, R., Avissar, R., Pacala, S.W.& Levin, S.A. 2002Mechanisms of long-distance dispersal of seeds by wind. Nature 418, 409-413.

Northrup MA, Kulp TJ, Angel SM (1991) Fluorescent particle image velocimetry – application to flow measurement in refractive index-matched porous-media. Appl Optics 30(21):3034-3040.

Novak MD, Warland JS, Orchansky AL, Ketler R, Green S (2000) Wind tunnel and field measurements of turbulent flow in forests. Part I: uniformly thinned stands. Boundary-Layer Meteorol 95(3):457-495.

Obukhov AM (1941) The spectral energy distribution in a turbulent flow. Dokl Akad Nauk SSSR 32: 453-466.

Okumra M, Yuki K, Hashizume H, Sagara A (2005) Evaluation of flow structure in packed-bed tube by visualization experiment. Fusion Sci Technol 47(4):1089-1093.

Pao YH (1965) Structure of turbulent velocity and scalar fields at large wavenumbers. Phys Fluids 8: 1063.

Parker J and Merati P (1996) An investigation of turbulent Taylor-Couette flow using laser dopplervelocimetry in a refractive index matched facility. J Fluids Eng Trans ASME 118(4):810-818.

Paw KT, Brunet Y, Collineau S, Shaw RH, Maitani T, Qiu J, Hipps L (1992) On coherent structures in turbulence above and within agricultural plant canopies. Agric Forest Meteorol 61:55-68.

Pietri L, Petroff A, Amielh M, Anselmet F (2009) Turbulence characteristic within sparse and dense canopies. Environ Fluid Mech 9:297-320.

Piomelli U, Cabot WH, Moin P, Lee S (1991) Subgrid-scale backscatter in turbulent and transitional flows. Phys Fluids A3:1766.

Piomelli U, Ferziger J, Moin P, Kim J (1989) New approximate boundary-conditions for large eddy simulations of wall-bounded flows. Phys Fluids A 1:1061-1068.

Piomelli U, Moin P, Ferziger JH (1988) Model consistency in large eddy simulation of turbulent channel flows. Phys Fluids 31:1884.

Poggi D, Katul GG, Albertson JD (2004a) A note on the contribution of dispersive fluxes to momentum transfer within canopies. Boundary-Layer Meteorol 111(3):615-621.

Poggi D, Porporato A, Ridolfi L, Albertson JD, Katul GG (2004b) The effect of vegetation density on canopy sub-layer turbulence. Boundary-Layer Meteorol 111(3):565-587.

Pope SB (2000) Turbulent flows. Cambridge University Press, UK, 771 pp.

Qiu J, Pawu UK, Shaw RH (1995) Pseudo-wavelet analysis of turbulence patterns in threevegetation layers. Boundary-Layer Meteorol 72:177-204.

Raupach MR (1994) Simplified expressions for vegetation roughness length and zero-plane displacement as functions of canopy height and area index. Boundary-Layer Meteorol 71:211-216.

Raupach MR, Antonia RA, Rajagopalan S (1991) Rough-wall turbulent boundary layer. Appl. Mech Rev 44:1-25.

Raupach MR, Coppin PA, Legg BJ (1986) Experiments on scalar dispersion within a model-plant canopy. Part I: the turbulence structure. Boundary-Layer Meteorol 35(1-2):21-52.

Raupach MR, Finnigan JJ, Brunet Y (1996) Coherent eddies and turbulence in vegetation canopies: the mixing-layer analogy. Boundary-Layer Meteorol 78(3):351-382.

Raupach MR and Shaw RH (1982) Averaging procedures for flow within vegetation canopies. Boundary-Layer Meteorol 22(1):79-90.

Raupach MR and Thom AS (1981) Turbulence in and above plant canopies. Ann Rev Fluid Mech 13:97-129.

Reynolds RT and Castro IP (2008) Measurements in an urban-type boundary layer. Exp Fluids 45:141-156.

Richardson LF (1922) Weather prediction by numerical process. Cambridge University Press.

Righetti A and Armanini A (2002) Flow resistance in open channel flows with sparsely distributed bushes. J Hydrol 269:55-64.

Roth GI, Mascenik DT, Katz J (1999) Measurements of the flow structure and turbulence within a ship bow wave. Phys Fluids 11(11):3512-3523.

Saddoughi SG and Veeravalli SV (1994) Local isotropy in turbulent boundary-layers at high Reynolds-number. J Fluid Mech 268:333-372.

Schwartz RC, Fryrear DW, Harris BL, Bilbro JD, Juo ASR (1995) Mean flow and shear stress distributions as influenced by vegetative windbreak structure. Agric. For. Meteorol. 75:1-22.

Seginer I, Mulhearn PJ, Bradley EF, Finnigan J (1976) Turbulent flow in a model plant canopy. Boundary-Layer Meteorol 10:423-453.

Seoud RE and Vassilicos JC (2007) Dissipation and decay of fractal-generated turbulence. Phys Fluids 19(10):105108.

Shaw RH, Brunet Y, Finnigan JJ, Raupach MR (1995) A wind tunnel study of air flow in waving wheat: two-point velocity statistics. Boundary-Layer Meteorol 76(4):349-376.

Shaw RH, Denhartog G, Neumann HH (1988) Influence of foliar density and thermal-stability on profiles of Reynolds stress and turbulence intensity in a deciduous forest. Boundary-Layer Meteorol 45(4):391-409.

Shaw RH, Tavangar J, Ward DP (1983) Structure of the Reynolds stress in a canopy layer. J Climate Appl Meteorol 22:1922-1931.

Shida S, Kosukegawa H, Ohta M (2011) Development of a methodology for adaptation of refractive index under controlling kinematic viscosity for PIV. Proceedings of the ASME, Colorado USA.

Sreenivasan KR and Meneveau C (1986) The fractal facets of turbulence. J Fluid Mech 173:357-386.

Stacey GR, Belcher RE, Wood CJ, Gardiner BA (1994) Wind flows and forces in a model spruce forest. Boundary-Layer Meteorol 69(3):311-334.

Stoll R and Porte-Agel F (2006) Effect of roughness on surface boundary conditions for large-eddy simulation. Boundary-Layer Meteorol 118:169-187.

Stoll R and Porte-Agel F (2008) Large-eddy simulation of the stable atmospheric boundary layer using dynamic models with different averaging schemes. Boundary-Layer Meteorol 126:1-28.

Stoots C, Becker S, Condie K, Durst F, McEligot D (2001) A large-scale matched index of refraction flow facility for LDA studies around complex geometries. Exp Fluids 30: 391-398.

Stresing R, Peinke J, Seoud RE, Vassilicos JC (2010) Defining a new class of turbulent flows. Phys Rev Lett 104(19):194501.

Su HB, Shaw RH (2000) Two-point correlation analysis of neutrally stratified flow within and above a forest from large-eddy simulation. Boundary-Layer Meteorol 94:423-460.

Tanino Y and Nepf HM (2008) Laboratory investigation of mean drag in a random array of rigid, emergent cylinders. J Hydraul Eng 134:34-41.

Talapatra S and Katz J (2012) Coherent structures in the inner part of a rough-wall channel flow resolved using holographic PIV. J Fluid Mech 711:161-170.

Tennekes H and Lumley JL (1972) A first course in turbulence. MIT Press, Boston, U.S.A., 300 pp.

Thom AS (1971) Momentum absorption by vegetation. Q J R Meteorol Soc 97:414-428.

Thormann A, Meneveau C (2014) Decay of homogeneous, nearly isotropic turbulence behind active fractal grids. Phys Fluids (under review)

Tomkins CD and Adrian RJ (2003) Spanwise structure and scale growth in turbulent boundary layers. J Fluid Mech 490:37-74.

Townsend AA (1947) Measurements in the turbulent wake of a cylinder. Proc R Soc A 190(1023):551-561.

Turner BJ, Leclerc MY, Gauthier M, Moore KE, Fitzjarrald DR (1994) Identification of turbulence structures above a forest canopy using a wavelet transform. J Geophys Res 99:1919-1926.

Uchijima Z (1962) Studies on the microclimate within the plant communities. Part II: the scale of turbulence and the momentum transfer within plant layers. J Agric Meteorol 18:58-65.

Uzol O, Chow YC, Katz J, Meneveau C (2002) Unobstructed particle image velocimetry measurements within an axial turbo-pump using liquid and blades with matched refractive indices. Exp Fluids 33(6):909-919.

Valente PC and Vassilicos JC (2011) The decay of turbulence generated by a class of multiscale grids. J Fluid Mech 687:300-340.

vanHout R, Zhu W, Luznik L, Katz J, Kleissl J, Parlange MB (2007) PIV measurements in the atmospheric boundary layer within and above a mature corn canopy. Part I: statistics and energy flux. J Atmos Sci 64:2805-2824.

Volino RJ, Schultz MP, Flack KA (2009) Turbulence structure in a boundary layer with two-dimensional roughness. J Fluid Mech 635:75-101.

Wallace JM, Eckelmann H, Brodkey RS (1972) Wall region in turbulent shear-flow. J Fluid Mech 54:39-48.

Wiederseiner S, Andreini N, Epely-Chauvin G, Ancey C (2011) Refractive-index and density matching in concentrated particle suspensions: a review. Exp Fluids 50(5):1183-1206.

Wildman DJ, Ekmann JM, Kadambi JR, Chen RC (1992) Study of the flow properties of slurries using the refractive index matching technique LDV. Powder Technol 73(3):211-218.

Wilson NR and Shaw RH (1977) Higher-order closure model for canopy flow. J Appl Meteorol 16(11):1197-1205.

Wu HX, Miorini RL, Katz J (2011) Measurements of the tip leakage vortex structures and turbulence in the meridional plane of an axial water-jet pump. Exp Fluids 50(4):989-1003.

Yousif MY, Holdsworth DW, Poepping TL (2011) A blood-mimicking fluid for particle image velocimetry with silicone vascular models. Exp Fluids 50:769-774.

Yue W, Meneveau C, Parlange MB, Zhu W, Kang HS, Katz J (2008) Turbulent kinetic energy budgets in a model canopy: comparisons between LES and wind-tunnel experiments. Environ Fluid Mech 8:73-95.

Yue W, Meneveau C, Parlange MB, Zhu W, van Hout R, Katz J (2007) A comparative quadrant analysis of turbulence in a plant canopy.Water Resour Res 43(5).

Yuki K, Okumura M, Hashizume H, Toda S, Morley NB, Sagara A (2008) Flow visualization and heat transfer characteristics for sphere-packed pipes. J Thermophys Heat Transf 22(4):632-648.

Zaytsev ID and Aseyev MA (1992) Properties of aqueous solutions of Electrolyte. CRC Press: Boca Raton, FL.

Zerai B, Saylor BZ, Kadambi JR, Oliver MJ, Mazaheri AR, Ahmadi G, Bromhal GS, Smith DH (2005) Flow characterization through a network cell using particle image velocimetry. Transp Porous Media 60:159-181.

Zhou J, Adrian RJ, Balachandar S, Kendall TM (1999) Mechanisms for generating coherent packets of hairpin vortices in channel flow. J Fluid Mech 387:353-396.

Zhu W, van Hout R, Katz J (2007) On the flow structure and turbulence during sweep and ejection events in a wind-tunnel model canopy. Boundary-Layer Meteorol 124:205-233.

Zhu W, van Hout R, Katz J (2007) PIV measurements in the atmospheric boundary layer within and above a mature corn canopy. Part II: quadrant-hole analysis. J Atmos Sci 64:2825-2838.

Zhu W, van Hout R, Luznik L, Kang HS, Katz J, Meneveau C (2006) A comparison of PIV measurements of canopy turbulence performed in the field and in a wind tunnel model. Exp Fluids 41(2):309-318.

Vita

Place of Birth: Yunnan, China

Education

Ph.D., Johns Hopkins University, Baltimore, MD, January 2014

M.S., Johns Hopkins University, Baltimore, MD, May 2009

B.S., Beijing University of Aeronautics and Astronautics (BUAA), China, July 2007

Publications

Kunlun Bai, Charles Meneveau, Joseph Katz (2013) Experimental Study of Spectral Energy Fluxes in Turbulence Generated by a Fractal, Tree-like Object. *Physics of Fluids* 25, 110810.

Kunlun Bai, Charles Meneveau, Joseph Katz (2012) Near-Wake Turbulent Flow Structure and Mixing Length Downstream of a Fractal Tree. *Boundary-Layer Meteorology* 143:285-308.

Kunlun Bai, Joseph Katz (2014) On the Refractive Index of Sodium Iodide Solutions for Index Matching in PIV. *Experiments in Fluids* (in revision).

Kunlun Bai, Joseph Katz, Charles Meneveau (2014) Experimental Study of Turbulence and the Variation of Flow Properties inside a Fractal Canopy by the Index-Matched PIV Technique. *Boundary-Layer Meteorology* (to submit).

Kunlun Bai, Charles Meneveau, Joseph Katz (2014) Coherent Structure and Momentum Transport at Various Scales above an Array of Multi-scale Structures. (in preparation).

Jason Graham, **Kunlun Bai**, Charles Meneveau, Joseph Katz (2011) LES Modeling and Experimental Measurement of Boundary Layer Flow over Multi-scale, Fractal Canopies. *Direct and Large Eddy Simulation VIII* (refereed conference proceedings) 15:233-238.

Presentations

Kunlun Bai, Joseph Katz, Charles Meneveau, Coherent Structures and Momentum Transport at Various Scales above an Array of Multi-scale Structures.66th Annual Meeting of American Physical Society Division of Fluid Dynamics, Pittsburgh, U.S. (November 24-26, 2013).

Kunlun Bai, Joseph Katz, Charles Meneveau, Index-Matched PIV Measurements of Turbulence inside a Fractal-Tree Canopy. 65th Annual Meeting of American Physical Society Division of Fluid Dynamics, San Diego, U.S. (November 18-20, 2012).

Charles Meneveau, **Kunlun Bai**, Joseph Katz, Subgrid Scale Energy Fluxes and Effective Length Scale in the Wake of a Fractal Tree. European Geosciences Union General Assembly, Vienna, Austria (April 22-27, 2012).

Kunlun Bai, Charles Meneveau, Joseph Katz, Mixing Length and Scale-to-Scale Kinetic Energy Transfer in the Wake of a Fractal Tree. 64th Annual Meeting of American Physical Society Division of Fluid Dynamics, Baltimore, U.S. (November 20-22, 2011).

Charles Meneveau, **Kunlun Bai**, Joseph Katz, Interactions between a Fractal Tree-like Object and Hydrodynamic Turbulence: Flow Structure and Characteristic Mixing Length. American Geophysical Union Fall Meeting, San Francisco, U.S. (December 5-9, 2011).

Kunlun Bai, Charles Meneveau, Joseph Katz, Near-Wake Turbulent Flow Structure and Mixing Length Downstream of a Fractal, Tree-like Object. CEAFM-Burgers Symposium:

Joint Symposium between Johns Hopkins University and University of Maryland, College Park, Baltimore, U.S. (May 13, 2011).

Kunlun Bai, Charles Meneveau, Joseph Katz, PIV Measurements of the Near-Wake behind a Fractal Tree. 63rd Annual Meeting of American Physical Society Division of Fluid Dynamics, Long Beach, U.S. (November 21-23, 2010).

Charles Meneveau, Jason Graham, **Kunlun Bai**, Joseph Katz, Simulating, Measuring, and Parameterizing Turbulent Boundary Layer Flow over Multi-Scale, Fractal Canopies. European Geosciences Union General Assembly, Vienna, Austria (May 2-7, 2010)